The Lyman alpha reference sample. IV. Morphology at low and high redshift

L. Guaita, J. Melinder, M. Hayes, G. Östlin, J. E. Gonzalez, G. Micheva, A. Adamo, J. M. Mas-Hesse, A. Sandberg, H. Otí-Floranes, et al.

A&A 576, A51 (2015)
DOI: 10.1051/0004-6361/201425053

Astronomy & Astrophysics

The Lyman alpha reference sample

IV. Morphology at low and high redshift⋆,⋆⋆

L. Guaita[1], J. Melinder[1], M. Hayes[1], G. Östlin[1], J. E. Gonzalez[1], G. Micheva[1,2], A. Adamo[1], J. M. Mas-Hesse[4], A. Sandberg[1], H. Otí-Floranes[5,14], D. Schaerer[3,6], A. Verhamme[6], E. Freeland[1], I. Orlitová[7], P. Laursen[8], J. M. Cannon[9], F. Duval[1], T. Rivera-Thorsen[1], E. C. Herenz[10], D. Kunth[11], H. Atek[12], J. Puschnig[1], P. Gruyters[13], and S. A. Pardy[14,15]

[1] Department of Astronomy, Oskar Klein Centre for cosmoparticle physics, Stockholm University, AlbaNova, 10691 Stockholm, Sweden
e-mail: lguai@astro.su.se
[2] Subaru Observatory, Hilo, Hawai, USA
[3] CNRS, IRAP, 14 avenue Edouard Belin, 31400 Toulouse, France
[4] Centro de Astrobiología (CSIC–INTA), Departamento de Astrofísica, POB 78, Villanueva de la Cañada, Spain
[5] Instituto de Astronomía, Universidad Nacional Autónoma de México, Apdo. Postal 106, 22800 Ensenada B. C., Mexico
[6] Geneva Observatory, University of Geneva, 51 Chemin des Maillettes, 1290 Versoix, Switzerland
[7] Astronomical Institute of the Academy of Sciences of the Czech Republic, Boční II 1401/1a, 141 00 Praha 4, Czech Republic
[8] Dark Cosmology Centre, Niels Bohr Institute, University of Copenhagen, Juliane Maries Vej 30, 2100 Copenhagen, Denmark
[9] Department of Physics and Astronomy, Macalester College, 1600 Grand Avenue, Saint Paul, MN 55105, USA
[10] Leibniz-Institut fur Astrophysik (AIP), An der Sternwarte 16, 14482 Potsdam, Germany
[11] Institut d'Astrophysique de Paris, UMR 7095 CNRS & UPMC, 98bis Bd Arago, 75014 Paris, France
[12] Laboratoire d'Astrophysique, École Polytechnique Fédérale de Lausanne (EPFL), Observatoire, 1290 Sauverny, Switzerland
[13] Department of Physics and Astronomy, Uppsala University, Box 515, 751 20 Uppsala, Sweden
[14] Centro de Radioastronomía y Astrofísica, UNAM, Campus Morelia, Mexico
[15] Astronomy Department, University of Wisconsin – Madison , 475 N. Charter Street, Madison, Wisconsin, 53706, USA

Received 25 September 2014 / Accepted 15 December 2014

ABSTRACT

Context. The transport of Lyα photons in galaxies is a complex process and the conditions under which Lyα photons manage to escape from certain galaxies is still under investigation. The Lyman alpha reference sample (LARS) is a sample of 14 local star-forming galaxies, designed to study Lyα in detail and relate it to rest-frame UV and optical emission.
Aims. With the aim of identifying rest-frame UV and optical properties, which are typical of Lyα emitters (LAEs, galaxies with EW(Lyα) > 20 Å) at both low and high redshift, we investigated the morphological properties of the LARS galaxies, in particular the ones that exhibit intense Lyα radiation.
Methods. We measured sizes and morphological parameters in the continuum, Lyα, and Hα images. We studied morphology by using the Gini coefficient vs. M20 and asymmetry vs. concentration diagrams. We then simulated LARS galaxies at $z \sim 2$ and 5.7, performing the same morphological measurements. We also investigated the detectability of LARS galaxies in current deep field observations. The subsample of LAEs within LARS (LARS-LAEs) was stacked to provide a comparison to stacking studies performed at high redshift.
Results. LARS galaxies have continuum size, stellar mass, and rest-frame absolute magnitude typical of Lyman break analogues in the local Universe and also similar to $2 < z < 3$ star-forming galaxies and massive LAEs. LARS optical morphology is consistent with the one of merging systems, and irregular or starburst galaxies. For the first time we quantify the morphology in Lyα images: even if a variety of intrinsic conditions of the interstellar medium can favour the escape of Lyα photons, LARS-LAEs appear small in the continuum, and their Lyα is compact. LARS galaxies tend to be more extended in Lyα than in the rest-frame UV. It means that Lyα photons escape by forming haloes around HII regions of LARS galaxies.
Conclusions. The stack of LARS-LAE Lyα images is peaked in the centre, indicating that the conditions, which make a galaxy an LAE, tend to produce a concentrated surface brightness profile. On the other hand, the stack of all LARS galaxies is shallower and more extended. This can be caused by the variety of dust and HI amount and distribution, which produces a more complex, patchy, and extended profile, like the one observed for Lyman break galaxies that can contribute to the stack. We cannot identify a single morphological property that controls whether a galaxy emits a net positive Lyα flux. However, the LARS-LAEs have continuum properties consistent with merging systems.

Key words. techniques: imaging spectroscopy – galaxies: star formation – galaxies: starburst

1. Introduction

Originating mainly in recombining gas being ionized by hot O and B stars, Lyman alpha (Lyα) radiation has proved an excellent

⋆ Based on observations made with the NASA/ESA *Hubble* Space Telescope. These observations are associated with programme 12310.
⋆⋆ Figures 5, 6 and 18, Tables 5–6, and Appendices are available in electronic form at http://www.aanda.org

probe of star-forming galaxies at both low (e.g., Cowie et al. 2011) and high (e.g., Ouchi et al. 2010) redshift.

Hayes et al. (2005, 2009) and Östlin et al. (2009) developed a method to separate the rest-frame UV and Lyα emission in *Hubble* Space Telescope (HST) data. In these papers it was demonstrated observationally that, in nearby galaxies ($z < 0.1$), Lyα emission extends away from the star-forming regions where the Lyα photons were originally generated, forming the so-called Lyα haloes.

Young starburst galaxies are expected to be very bright in Lyα (Partridge & Peebles 1967). For the past 15 years, star-forming galaxies have been successfully detected at $z > 2$ by identifying their strong Lyα emission line. The principal method used is the narrow-band technique (e.g., Cowie & Hu 1998; Rhoads et al. 2000; Ouchi et al. 2008; Gronwall et al. 2007; Nilsson et al. 2009): Lyα emitters (LAEs) present an excess in a narrow band (covering the redshifted Lyα wavelength) with respect to a broad-band filter (covering the rest-frame UV continuum). Because Lyα photons are easily absorbed by dust grains and are scattered by neutral hydrogen (HI), LAEs were thought to be a *special* population of galaxies with *special* dust and HI amounts and distribution. Although extensive studies have been carried out to characterize LAE physical properties and their special conditions (Nilsson et al. 2011; Acquaviva et al. 2012; McLinden et al. 2014; Vargas et al. 2014; Hagen et al. 2014, among the most recent ones), the results have been inconclusive. The mechanisms (e.g., interstellar medium geometry and kinematics) controlling the escape of Lyα photon are still debated.

The morphology of the rest-frame UV and optical continua provides information about galaxy formation and evolution (e.g., star-forming region distribution, merger events, Conselice 2003; Lotz et al. 2004). From the ground LAEs were observed to be compact in the rest-frame UV, but multiple components were identified in deep HST-resolution images (Bond et al. 2009, 2012). There have also been a few attempts to quantify the morphology of the Lyα emission itself. Bond et al. (2010) explored a sample of seven LAEs placed at $z \simeq 3.1$ (observed-frame λ(Lyα) $\sim$ 5000 Å) by using HST Wide Field Camera2 (WFPC2) F502N narrow-band imaging. They found that, for one source, Lyα emission extended till 1.5 kpc ($\leq$1 kpc for the other six), a just-slightly-larger scale than the UV continuum. Also, this source was composed of two main clumps both in the rest-frame UV and in Lyα. Finkelstein et al. (2011a) spatially resolved three spectroscopically confirmed LAEs placed at $z \simeq 4.5$ (observed-frame λ(Lyα) $\sim$ 6570 Å) by using the HST Advanced Camera for Surveys (ACS) F658N narrow band. Two out of the three systems showed Lyα emission significantly more extended than the UV continuum.

Recently, evidence of extended Lyα emission was found in the stack of a large sample of Lyman break galaxies, (Steidel et al. 2011), which are generally more massive and dustier than LAEs, and of galaxies located in overdense regions (Matsuda et al. 2012). By stacking hundreds of $z \simeq 2.2$, $z \simeq 3.1$, $z \simeq 3.7$, and $z \simeq 5.7$ LAEs from deep ground-based imaging, Momose et al. (2014) discovered extended Lyα emission, with scale lengths in the range of 5−10 kpc. However, by stacking their sample of LAEs Feldmeier et al. (2013) just found a marginal detection at $z \sim 3.1$ and a non-detection at $z \simeq 2.07$. It is clear that depth and image resolution were the main factors affecting their results.

Instead, giant Lyα nebulae, powered by active galactic nuclei, have been studied by a few authors to assess the role of HI scattering and Lyα radiative transfer effects (e.g., Humphrey et al. 2013a; Prescott et al. 2015)

Local starbursts (Overzier et al. 2008, 2009, 2010; Hayes et al. 2013, 2014; Petty et al. 2014; Östlin et al. 2014) are unique laboratories for studying the rest-frame UV in detail and optical light distribution, morphology, and to investigate the mechanisms, that allow Lyα photons to escape. In Östlin et al. (2014, hereafter Paper I) we presented the Lyman alpha reference sample (LARS), which is composed of 14 star-forming galaxies at $z < 0.2$. These galaxies were observed during HST cycle 18 (P.I. G. Östlin) in a set of rest-frame UV (ACS/SBC *F125LP*, *F140LP*, *F150LP*) and optical (*WFC3/UVIS F336W/F390W*, *F438W/F475W*, *F775W/F850LP*, *F502N*, *F656N*, and ACS/WFC *F502N/F505N/F551N*, *F656N/F716N/F782N*) filters. Lyα maps were generated by estimating the continuum at rest-frame λ(Lyα) = 1216 Å, through modelling the galaxy spectrum as a composite population of young stars, old stars, and nebular gas. LARS images were published in Hayes et al. (2013, hereafter Paper 0) and further analysed in Hayes et al. (2014, hereafter Paper II). We found that the Lyα emission profile appeared different from the rest-frame UV and it flattened on scales larger than the rest-frame UV. The majority of the 14 galaxies showed a negative Lyα equivalent width at small radii and then an increase farther out. We concluded that this was due to scattering on neutral hydrogen, which is able to shape the Lyα emission into the form of haloes. Also, by comparing LARS Lyα with global physical properties, it appeared that the Lyα photon escape was favoured in the system with weaker dust reddening and low stellar mass.

The neutral hydrogen content of LARS galaxies was presented in Pardy et al. (2014, hereafter Paper III). The spectral lines of HI were detected in 11 of the 14 observed LARS galaxies and it was also found that the Lyα escape was favoured in low HI-mass systems. LARS interstellar medium kinematics will be presented in Rivera-Thorsen et al. (2015), Duval et al. (in prep.), and Orlitová et al. (in prep.).

In this paper, number IV of the series, we address the question whether specific galaxy morphological properties could be related to the escape of Lyα photons and escape in haloes. Note that in Paper I the present paper was termed paper 7, due to a previous numbering. In Sect. 2, we briefly explain how we measured morphological parameters (details are given in Appendix A) and the process adopted to simulate how some local ($z < 0.2$) galaxies would appear at high redshift ($z > 2$). In Sect. 3, we describe the morphological properties of the sample of local galaxies and compare them with local-Universe and high-z galaxy populations. In Sect. 4, we study the morphological properties of the high-z-simulated galaxies. In Sect. 5, we present the stacking of the high-z-simulated sample and compare with high-z stacks in the literature. In Sect. 6 and 7, we discuss and summarize the main results of the paper.

Throughout we adopt AB magnitudes and assume a ΛCDM cosmology of (H_0, Ω_m, Ω_Λ) = (70 km s^{-1} Mpc^{-1}, 0.3, 0.7) as in Hayes et al. (2013, 2014).

2. Method

We present the morphology of the local ($0.03 < z < 0.2$) LARS galaxies and investigate how it would change if the same galaxies were observed at high redshift. As explained above, in Paper II we isolated the contributions of the rest-frame UV (~1220 Å), optical (~6570 Å), Lyα (1216 Å), and Hα (6563 Å). In this work, we measure the morphological parameters of these

contributions. The LARS galaxies are hereafter referred to as Ln, where n ranges from 01 to 14 (see Paper 0).

2.1. Morphological parameter estimation

With the aim of quantifying the morphology of LARS galaxies, we calculated their sizes and performed non-parametric measurements of morphological parameters (see Appendix A and Fig. A.1 for details).

We calculated sizes, in terms of Petrosian semi-major axis (rP20, e.g., Lotz et al. 2004; Lisker 2008), circular Petrosian radius (Petrosian 1976), and radii containing 20%, 50%, and 80% of the flux (r_{20}, r_{50}, r_{80}). A comparison between these radii gives an idea of the distribution of the light in the galaxy. We also estimated asymmetry (A), concentration (C), clumpiness (S), Gini coefficient (G), and second-order moment of the brightest 20% of the galaxy's flux (M20, see e.g., Conselice 2003; Lotz et al. 2004; Scarlata et al. 2007; Micheva et al. 2013).

The asymmetry quantifies the symmetry of a galaxy with respect to a 180-degree rotation; the concentration describes how much the light is concentrated in the centre of a galaxy; the clumpiness measures the amount of small-scale structures within a galaxy; the Gini coefficient provides the information on how uniform is the light distribution; M20 traces the spatial distribution of any bright knots, and also off-centre clumps, its definition is very similar to that of C, but M20 is more sensitive to merger structures, such as off-centre components.

We first ran the Source Extractor (SExtractor) software (Bertin & Arnouts 1996). It provided the galaxy centroid and the elliptical aperture, containing the entire galaxy and characterized by semi-major axis (sma) equal to rP20. The photometry was performed within this SExtractor detection aperture.

We adopted configuration parameters like in Bond et al. (2009; DETECT_THRESH = 1.65, DETECT_MINAREA = 30, DEBLEND_MINCONT = 1). They were optimized to provide morphological measurements in deep HST rest-frame UV observations at $z > 2$. To prevent SExtractor from breaking up the clumpy, resolved $z \sim 0$ LARS galaxies into smaller fragments, we assumed a larger value of DETECT_MINAREA. This parameter sets the number of contiguous pixels required for a detection to be accepted by SExtractor. We measured fluxes at SExtractor centroid within elliptical apertures, by using the ELLIPSE task in *iraf.stsdas.isophote* and within circular apertures, by using the PHOT task in *iraf.digiphot.apphot*. ELLIPSE and PHOT outputs served to infer sizes, A, and C at minimum asymmetry ($C^{\mathrm{min}A}$), as explained in Appendix A and previously adopted in Bershady et al. (2000), Conselice (2003), Micheva et al. (2013).

The non-parametric measurements and signal-to-noise estimations were performed counting the flux of pixels belonging to a segmentation map. We defined the segmentation map in two ways, one is an ellipse with semi-major axis equal to rP20 (Scarlata et al. 2007) and orientation given by SExtractor; one contains the pixels with surface brightness larger than the value at the Petrosian radius (Lotz et al. 2004) measured in the smoothed image (smoothed by a kernel of width rP20/5). We calculated M20, S and Gini coefficient by considering the pixels within these segmentation maps. The Gini coefficients measured in these two segmentation maps are denoted by G^{rP20} and $G^{SB-rp20S}$ respectively. As described in Scarlata et al. (2007), G^{rP20} was defined to be consistent for redshift comparisons, thus we prefer it over $G^{SB-rP20S}$ throughout the paper when we compare with high redshift.

To test our code, we applied it to template galaxies with known profiles and compared the output to the results by Bershady et al. (2000) and Lotz et al. (2006). We recovered the expected values as described in Appendix A.

2.2. Combination of morphological parameters

As shown in Conselice (2003) and Lotz et al. (2004), combinations of morphological parameters can give information about galaxy history (e.g., star-formation and merging episodes). First of all the rest-frame UV morphology is sensitive to the current star formation; the rest-frame optical traces the structure of the entire galaxy stellar population (Lee et al. 2013; Bond et al. 2014). The combinations of parameters (see previous section) we adopted are,

- Asymmetry vs. concentration, asymmetry vs. clumpiness, together with clumpiness vs. concentration, as presented by Conselice (2003)
- Gini coefficient vs. M20 bright-pixel moment, as presented in Lotz et al. (2004).

The concentration depends on the galaxy star-formation history in the sense that a rapid gravitational collapse can produce high concentration. The presence of disk and intergalactic gas which cools onto the disk tends to produce a lower concentration value. Disk galaxies are characterized by $3 < C < 4$, ellipticals by $C > 4$ (Bershady et al. 2000). The asymmetry is sensitive to any feature that produces asymmetric light distributions (e.g., star-formation knots, interactions, and mergers). It is commonly assumed also at high z that large asymmetry ($A > 0.38$) indicates a major merger (Aguirre et al. 2013; Conselice 2003). Spiral galaxies and systems composed of more than one component are characterized by $A > 0.1$. The clumpiness is sensitive to the presence of star-forming clumps as well, but background noise can make it difficult to detect low surface brightness regions and increase the appearance of the galaxy as a mix of clumps. The Gini coefficient can be strongly correlated with C. By definition, $G = 1$ means that the light is all concentrated in one pixel, $G = 0$ that the light is equally distributed across the galactic body. In the case of a shallow light profile, both G and C are low. When more than one clump contains a significant fraction of light, G can be much larger than zero, but C still low. M20 traces the spatial distribution of off-centre bright regions.

In general, starburst and irregular galaxies are expected to have large A, large S, and intermediate C, merging systems and perturbed disks show large M20 and intermediate G.

2.3. High-redshift simulation

We simulated the observations of LARS galaxies (all at $z < 0.2$) at higher redshift by transforming their original science- and weight-map images (Paper I) according to the following steps (see also Overzier et al. 2008; Adamo et al. 2013).

1. The images were resampled preserving the flux (*IDL* frebin function). The size of the output image was defined by fixing the physical size of the galaxies. We chose mainly a $z \sim 2$ sampling to be able to compare with the interesting results obtained by surveys of Lyman alpha emitters in the last recent 5 years (Nilsson et al. 2009; Guaita et al. 2010; Hayes et al. 2010; Nakajima et al. 2012; Sandberg, in prep.). Also, the size changes a little with redshift.
2. Continuum subtraction (Hayes et al. 2009) was applied to the resampled images to generate rest-frame UV continuum

Table 1. 10σ detection limits applied to high-z simulated LARS images.

F(Lyα) erg s^{-1} cm^{-2}	m(rest-frame UV) AB	F(Hα) erg s^{-1} cm^{-2}	m(rest-frame optical) AB
5E-19	30	2E-19	29
3E-18	29	6E-19	28
8E-18	28	1E-18	27
2E-17	27	3E-18	26
5E-17	26	1E-17	25

Notes. Noise corresponding to the detection limits given in the table was added to LARS continuum and line images. As LARS Lyα and Hα(rest-UV and optical continua) images are in units of flux(flux density), the image depths are given in units of erg s^{-1}cm^{-2} (AB magnitudes). The MUSYC (Guaita et al. 2010; Bond et al. 2012) NB3727 survey implied a 10σ detection limit of F(Lyα) = 5E-17 erg s^{-1} cm^{-2}. MUSYC U,B (HUDF V606) 10σ detection limits were about 26(29.5). Assuming a *NB3727* filter width and transmission profile, a source with $m_{\rm AB}$(rest-frame UV) = 30 and EW(Lyα) = 20 Å is characterized by F(Lyα) = 5E-19 erg s^{-1} cm^{-2}. $m_{\rm AB}$(rest-frame UV) = 30, 29, 28 are consistent with HUDF09, GOODS, and GEMS survey depths (Bond et al. 2009). Lee et al. (2012) survey was characterized by a 10σ detection limit of 22.9 in *NB210* and 23.7 in K. CANDELS wide(deep) *F160W* 10σ detection limit was 25.8(26.5). Assuming a *NB210* filter width, a source with $m_{\rm AB}$(rest-frame optical) = 27 and EW(Hα) = 20 Å is characterized by F(Hα) = 2E-19 erg s^{-1} cm^{-2}.

and Lyα line, rest-frame optical continuum and Hα line images. The line images are in units of flux (erg s^{-1} cm^{-2}), while the continuum images are in units of flux densities (erg s^{-1} cm^{-2} Å^{-1}).

3. The image pixel values were scaled based on luminosity distance and surface brightness dimming (i.e., Hubble & Tolman 1935; Bouwens et al. 2004).
4. Gaussian noise, corresponding to a certain simulated survey depth, was added to the resampled and rescaled images by running the MKNOISE task in *iraf.artdata*. To calculate uncertainty on galaxy sizes and morphological parameters we performed Monte Carlo simulations by repeating 100 realizations of a noisy image. The noise applied was defined as the 10σ detection within a ~50 pixel (equivalent to a square aperture of ~0.2″ on a side for HST ACS optical filters) area, similar to the limits given for the *Hubble* Ultra Deep Field (HUDF, Beckwith et al. 2006). We do not show simulations in which we only resampled the pixel scale to that of a ground-based telescope and instrument, because the main effect on continuum and line images was produced by survey depth and ground-based point spread function (PSF, see Sect. 5).

To choose reasonable ranges of detection limits (Table 1) to apply, we referred to the MUlti-wavelength Survey by Yale-Chile (MUSYC) NB3727 narrow band (Guaita et al. 2010; Bond et al. 2012), to the triple narrow band by Nakajima et al. (2012), CANDELS/HUDF (McLure et al. 2013) broad band, and to the dual narrow-band survey by Lee et al. (2012).

3. LARS galaxies at $z \sim 0$

To be able to compare the Lyα, Hα, and continuum properties of LARS galaxies with those of high-z Lyα emitters (LAEs), we focused on the twelve LARS galaxies with EW(Lyα) > 1 Å as measured in Paper II. Thus, we excluded from this analysis the two galaxies of the sample (L04 and L06) characterized by null Lyα maps. LARS galaxies with integrated EW(Lyα) > 20 Å composed the subsample of LARS-LAEs (consisting of six galaxies). Various physical characteristics of the LARS galaxies (including their coordinates) are discussed in Paper II.

In Fig. 1[1] we present the red giant branch (RGB) images of the twelve LARS galaxies. Most of the galaxies show localized knots of star formation superposed on extended rest-frame optical emission; the Lyα emission is extended on larger angular scales (the Lyα haloes).

We investigated the properties of LARS galaxies in the context of other galaxy populations, to assess the fairness of our comparison. In Figs. 2 and 3 we show the location of the LARS galaxies in the half-light radius vs. stellar mass (r_{50} vs. $\log(M_*/M_\odot)$) and the half-light radius vs. UV absolute magnitude (r_{50} vs. $M_{\rm UV}$) diagrams, to understand if the LARS galaxies harbour stellar masses and UV magnitudes comparable to values in the literature. These diagrams have been designed for local galaxies, for which sizes could be easily measured in the rest-frame optical bands (Shen et al. 2003). However, measurements in the rest-frame UV could also be performed at high redshift. Following the method described in Sect. 2, we estimated the half-light radius as r_{50} in the rest-frame optical and also in the rest-frame UV images.

The high-z studies we adopted for comparison all performed size and morphological measurements by using HST images. These include,

- Continuum-selected Lyman break galaxies (LBGs) at $z \sim 3$, with and without Lyα in emission (Pentericci et al. 2010); at $z \sim 1$, 2, and 3 (Mosleh et al. 2011), at $1.5 < z < 3.6$ (Law et al. 2012); at $z \sim 1.8$ (Lotz et al. 2004); z-drop outs at $z \sim 7$ (Grazian et al. 2012); high signal-to-noise z- and Y-drop outs detected in the *Hubble* Ultra Deep Field, UDF12 (Ono et al. 2013).
- Compact star-forming galaxies (cSFGs) at $2 < z < 3$ (Barro et al. 2013). These authors have pointed out that, based on their number densities, masses, sizes, and star formation rates, $z \sim 2$–3 compact, star-forming galaxies were likely progenitors of compact, quiescent, massive galaxies at $z < 2$.
- Star-forming galaxies selected based on their $B-z$ and $z-K$ colour (sBzK, Yuma et al. 2012; Lee et al. 2013); passive and star-forming galaxies selected based on their $B-z$ and $z-K$ colour (pBzK and sBzK, Lee et al. 2013).
- Star-forming galaxies at $z \sim 2$–3 by Law et al. (2012). These authors found a typical value of the Gini coefficient ($G^{SB-rP20S} = 0.4$) for the sources with the strongest Lyα emission, characterized by $M_* \sim 1.5 \times 10^{10}\ M_\odot$.
- Great Observatories Origins Deep Survey (GOODS) and UDF (Ultra Deep Survey) $z \sim 4$ and GOODS $z \sim 1.5$ sources from the study of Lotz et al. (2006).
- Sub-millimeter galaxies (SMGs, Aguirre et al. 2013).
- Narrow-band selected Lyman alpha emitters at $z \simeq 2.07$ and $z \simeq 3.1$ (Bond et al. 2009, 2012) belonging to the MUSYC survey. We considered the stack of the $z \sim 2.07$ entire sample and of subsamples separated by photometric properties, UV-faint(UV-bright) with $R > 25.5(<25.5)$, IRAC-faint(IRAC-bright) with $f_{3.6\,\mu{\rm m}} < 0.57(>0.57)$ μJ, low-(high-)EW with EW(Lyα) < 66(>66) Å, red-(blue-)LAE with $B-R > 0.5(<0.5)$ (Guaita et al. 2011).
- Narrow-band selected Lyman alpha emitters at $z \sim 5.7$, 6.5, and 7.0 (Jiang et al. 2013), the first very-high-redshift sample

[1] We took advantage of this codification of the Lupton et al. (2004) prescription to produce RGB images: http://dept.astro.lsa.umich.edu/~msshin/science/code/Python_fits_image/

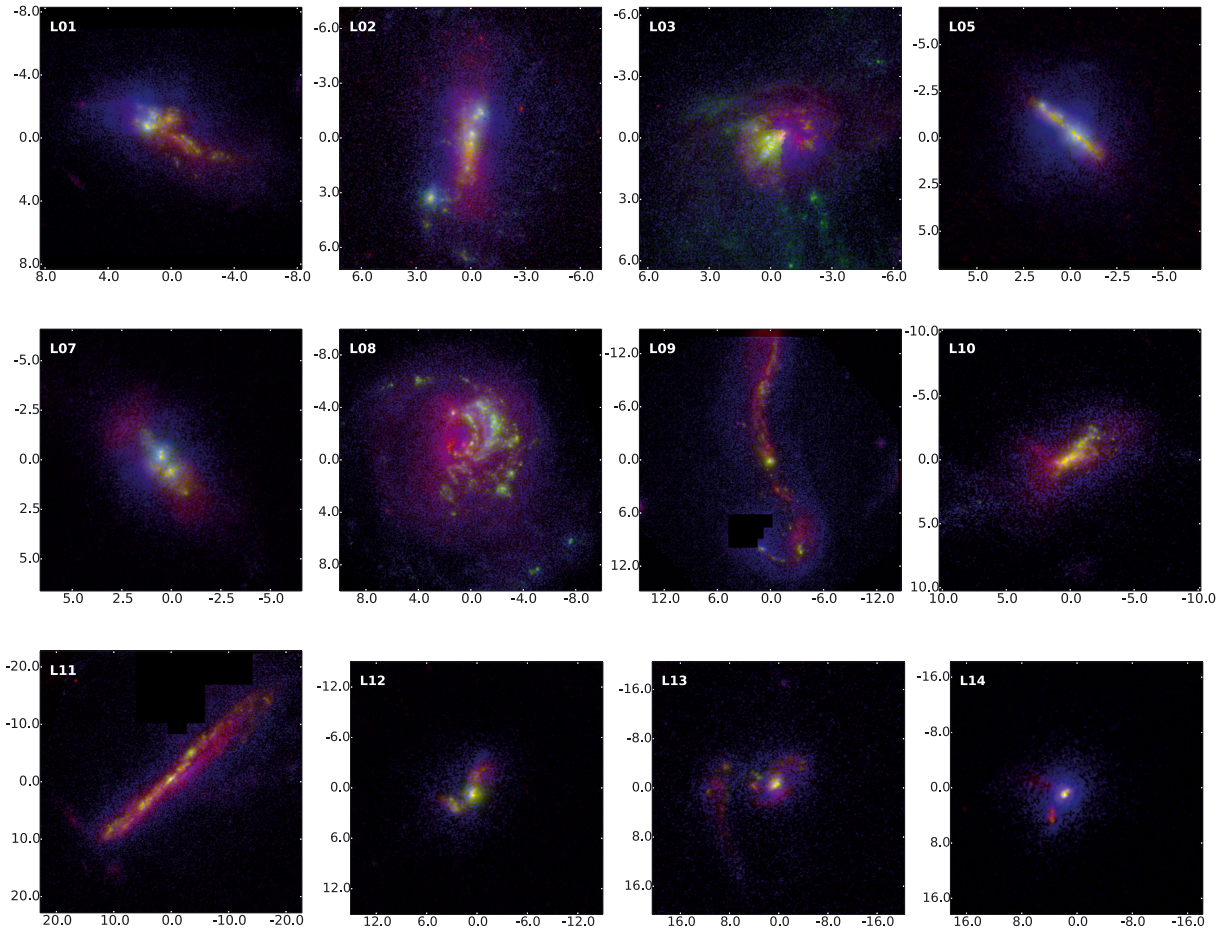

Fig. 1. False-colour images of the LARS galaxies analysed in this paper. Red encodes rest-frame optical continuum, green rest-frame UV continuum, and blue shows continuum-subtracted Lyα. Scales in kpc are given on the side. Intensity cut levels are set to show details.

where non-parametric morphological measurements were performed.

The local-Universe studies, we adopted for comparison, include,

- Sloan Digital Sky Survey (SDSS) early- and late-type galaxy relations obtained from the analysis of images in the z band (Shen et al. 2003).
- Lyman break analogues (LBAs) at $z \simeq 0.2$. These are local starbursts that share typical characteristics of high-z LBGs, such as stellar mass, metallicity, dust extinction, star-formation rate, and physical size. We considered a sample of 30 LBAs from Overzier et al. (2009, 2010). They were characterized by a median absolute UV magnitude of −20.3, almost one magnitude fainter than typical LBGs.

We found that the LARS galaxies occupy a quite wide range of r_{50}. Their rest-frame UV and optical sizes (Table 2) are broadly consistent with LBAs, LBGs, and SMGs. Their stellar mass tend to be larger than LAEs, consistent with LBAs and LBGs. However, there is an overlap in stellar mass between LARS-LAEs ($M_* < 10^{10}$ $M_\odot$) and the most massive LAEs in the sample of Bond et al. (2012). Also, LARS galaxies are less massive than cSFGs. The largest half-light radii characterize the LARS galaxies with the most distorted morphology (see also Fig. B.2). LARS $M_{\rm UV}$ magnitudes (and so star-formation rate, SFR$_{\rm UV}$) are comparable with those of $z \simeq 2.07$ LAEs and $z \geq 7$ LBGs. There is an overlap with $z > 5$ LAEs. However, the measurements of LARS sizes in the rest-frame UV are larger than those of $z \geq 7$ LBGs.

Therefore, LARS galaxies could be considered as LBAs, with size, stellar mass, and star-formation rate similar to $2 < z < 3$ star-forming galaxies.

3.1. Continuum morphology of LARS galaxies at $z \sim 0$

Following the method described in Sect. 2, we estimated the non-parametric measurements for the LARS galaxies (Table 3).

Combinations of morphological parameters (see Sect. 2.2) can give information about a galaxy's star-formation history. Lotz et al. (2004) proposed a criterion for separating perturbed disks or merging systems from normal galaxies, by studying local ultra luminous infrared galaxies (ULIRGs). The criterion identifies a region in the G vs. M20 diagram, which is $G^{SB-rP20S} > -0.115 \times {\rm M20} + 0.384$. For $z < 1.2$ galaxies observed in a rest-frame optical band (4000 Å) at HST resolution, Lotz et al. (2008) proposed a slightly different relation to identify merging systems, $G^{SB-rP20S} > -0.14 \times {\rm M20} + 0.33$. Also, Conselice (2003) distinguished the region where irregular or starburst galaxies were located in the A-C$^{{\rm min}A}$ and A-S planes.

As seen in Fig. 4 and Table 3, LARS galaxies, in particular the LARS-LAEs, tend to avoid the location of normal galaxies and to occupy the region of perturbed disks or merging systems and of irregular or starburst galaxies. The values of G, M20, C, and A, we calculated for LARS galaxies, are consistent with the ones measured by Overzier et al. (2010) for LBAs. Even if our sample is just composed of twelve sources, we do not see any significant dependency between G and EW(Lyα). L08 is

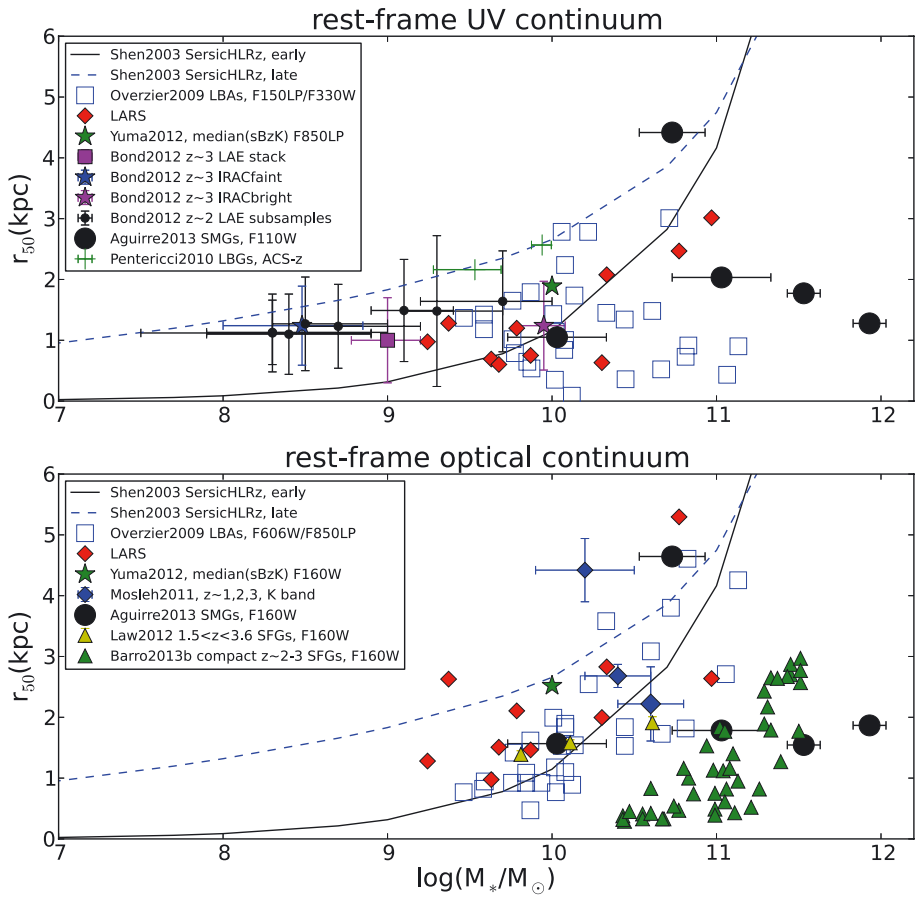

Fig. 2. Half-light radius measured using elliptical apertures in the rest-frame UV (*upper panel*) and optical (*lower panel*) as a function of stellar mass. LARS values at $z \sim 0$ from this work (red diamonds) are shown together with previous rest-frame UV measurements: Overzier et al. (2009) individual LBA values estimated in the HST ACS/SBC *F150LP* and ACS/HRC *F330W* filter (open blue squares), Yuma et al. (2012) median estimations in the *F850W* filter for sBzK (green star), Bond et al. (2012) LAE sample stack and subsamples (magenta square, blue and magenta stars, small black circle), Aguirre et al. (2013) individual SMG values measured in the HST *F110W* filter (big black dots), and Pentericci et al. (2010) average values of LBGs with and without Lyα in emission (green dots); and rest-frame optical measurements: Overzier et al. (2009) individual LBA values estimated in the HST (Wide Field and Planetary Camera2) *WFPC2/F606W* and ACS/WFC *F850LP* filter (open blue squares), Yuma et al. (2012) median estimations in the *F160W* filter for sBzK (green star), Mosleh et al. (2011) median values of UV-bright sources (GALEX-LBGs at $z \sim 0.6$–1.5, LBG at $z \sim 2.5$–3.5, and continuum-selected star-forming galaxies at $z \sim 1.5$–2.5, blue diamonds), Aguirre et al. (2013) individual SMG values measured in *F160W* filter, Law et al. (2012) mean value of all the sample of star-forming galaxies at $1.5 < z < 3.6$ estimated in the *F160W* filter (yellow triangles), and Barro et al. (2013) values for compact star-forming galaxies at $2 < z < 3$ also calculated in the *F160W* filter (green triangles). We also show the curve derived by Shen et al. (2003) for local SDSS early- and late-type galaxies. As these curves were obtained in z-bands for local galaxies, it is more meaningful to compare them to the radii in the rest-frame optical. However, for reference, we show them in the *upper panel* as well. The stellar masses are all corrected to Salpeter-IMF values and the size measurements are all scaled to be comparable to half-light radii. LARS stellar masses were calculated in Paper II. L09 and L11 are outside the graph, due to their half-light radius larger than 6 kpc.

the most massive of the LARS-LAEs, but equally concentrated within the segmentation map. L02 is the largest-EW(Lyα) emitter, characterized by one of the smallest stellar masses and the largest $G^{SB-rP20S}$ among the LARS-LAEs.

3.2. Lyα morphology of LARS galaxies at $z \sim 0$

One of the goals of our work was to quantify and compare the morphologies of LARS galaxies in Lyα and in the continuum. We present morphological parameters measured in the continua and in Lyα of LARS images in Figs. 5 and 6. G^{rP20}, M20, concentration, and ellipticity are smaller; while clumpiness and asymmetry are generally larger in Lyα than in the rest-frame UV continuum. The LARS-LAEs tend to be characterized by the highest concentration, lowest asymmetry, and lowest clumpiness in Lyα. G^{rP20} and M20 measured in the rest-frame optical are consistent with the values measured in Lyα.

4. LARS galaxies as seen at $z \sim 2$

We applied the procedure described in Sect. 2.3 to simulate LARS galaxies at $z \sim 2$. We named the high-z simulated galaxies as z2LARS and the subsample of Lyα emitters as z2LARS-LAEs. We estimated sizes and calculated morphological parameters (Tables 5 and 6) in the same way we did for the original images in Sect. 2.1.

The purpose of this test was to understand whether we could expect to detect LARS-type galaxies and LARS-type Lyα haloes in current high-z surveys. In particular, we wanted to understand how galaxy size and morphological parameters changed when varying the survey depth (Table 1). The results show that, in a

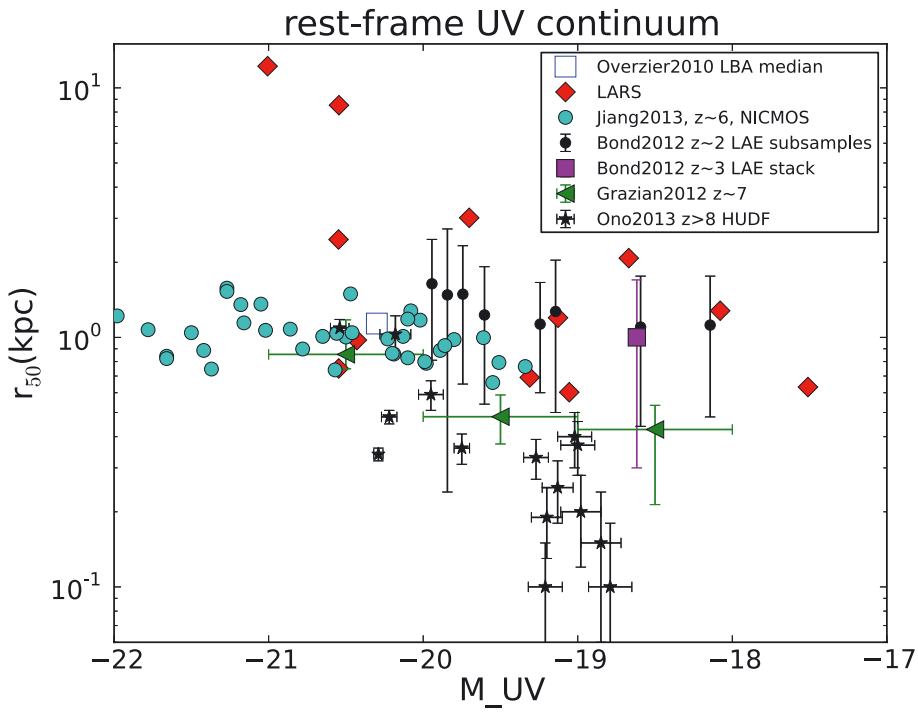

Fig. 3. Half-light radius measured using elliptical apertures in the rest-frame UV image as a function of the absolute rest-frame UV magnitude. LARS measurements from this work (red diamonds) are shown together with the literature estimations by Overzier et al. (2010) corresponding to the median value of their $z < 0.3$ LBAs, observed in the near-infrared bands, by Jiang et al. (2013) for a sample of $z \sim 5.7, 6.5, 7.0$ LAEs (cyan dots), by Bond et al. (2012) for the stack and subsamples of LAEs at $z \simeq 2-3$ (black circles, magenta squares), by Grazian et al. (2012) which measured SExtractor half-light radii for a sample of z-drop outs (green triangles), and by Ono et al. (2013) for a sample of high signal-to-noise z- and Y-drop outs detected in *Hubble* Ultra Deep Field, UDF12 (black stars).

sufficiently deep survey, faint galaxy structures in between bright knots remain connected together and SExtractor is able to detect just one source (the entire galaxy) in the image. In a shallower survey, the faint connecting structures tend to be lost in the noise and a galaxy appears to be composed of separated clumps. In that case SExtractor identifies more than one source and photometry is performed by locating the photometric aperture around the brightest clump. In Figs. B.1−B.3, we show how LARS galaxies would appear if detected in the deepest continuum and line surveys simulated here, while Figs. B.4−B.6 show the results for shallower surveys. In Appendix C, we present the corresponding surface brightness profiles.

In the following sub-sections, we describe the detection of LARS galaxies in the simulated surveys with 10σ detection limits presented in Table 1. In the first sub-section, we give details on the detection of L01 as an example. We proceed to describe the cases of the LARS-LAEs and of the galaxies with the faintest Lyα emission. Then, we explain the variations in size and ellipticity versus clumpiness owing pixel resampling and survey depth. In Sect. 4.6, we quantify the morphology of z2LARS and compare with high-z observations from the literature.

4.1. Detection of L01 in high-redshift surveys

In Fig. 7, we show the rest-frame UV, Lyα, optical, and Hα images of L01 simulated to be at $z \sim 2$ (z2L01) as they would be observed in the deepest surveys probed here; SExtractor detection apertures are over-plotted. The detection parameters we adopted are sensitive enough that (at the deepest simulated surveys) this galaxy is detected as a single source. As described in detail in Paper I and II, L01 consists of a bright UV star-forming centre with an extended tail, also seen in Hα and in the rest-frame optical. The Lyα emission is coincident with the bright UV knot and extends in a fan-like structure possibly indicating the presence of an expanding bubble. The main features of emission (dark red pixels in Fig. 7) and absorption (white pixels), observed in Lyα thanks to the HST resolution and the careful continuum subtraction presented in Paper II, are clearly visible in the $z \sim 2$ simulation as well. However, the extremely detailed Lyα structures close to the centre of the galaxy (see Paper I, Fig. 1) are not visible. The last panel of Fig. 7 shows L01 Lyα image, convolved with a ground-based seeing. From the ground L01 Lyα morphology would appear smoothed.

We show the surface brightness profiles of z2L01 in Fig. 8. The rest-frame UV and Lyα profiles (left column panels) are preserved when observed in a survey with sensitivity deeper than $m^{\rm lim}_{\rm rest-UV} = 28$ and $F({\rm Ly}\alpha)^{\rm lim} = 8{\rm E}{-}18$ erg s^{-1} cm^{-2}. However, on scales larger than 4 kpc, the profiles are indistinguishable from the background noise. In shallower surveys, the profiles start to be affected by the simulated-survey noise on smaller scales and z2L01 could not be detected by adopting a SExtractor detection threshold, DETECT_THRESH = 1.65. Therefore, size and morphological parameter measurements could not be performed either. We define $m^{\rm lim}_{\rm rest-UV}$ and $F({\rm Ly}\alpha)^{\rm lim}$ as the limits for detection and morphological parameter measurement. These limits are $m^{\rm lim}_{\rm rest-optical} = 26$ and $F({\rm H}\alpha)^{\rm lim} = 3{\rm E}{-}18$ erg s^{-1} cm^{-2} for L01 rest-frame optical and Hα.

The lower left panel of Fig. 8 shows that the rest-frame UV continuum profile is steeper than the Lyα profile. The lower right panel shows that the rest-frame optical continuum tends to be shallower than the rest-frame UV and the Hα, and more similar to the Lyα profiles.

Table 2. Size of the original LARS galaxies at $z \sim 0$.

(1) LARS	(2) rP20^{ell} kpc	(3) rP20^{circ} kpc	(4) rP20^{minA} kpc	(5) r_{20} kpc	(6) r_{50} kpc	(7) r_{80} kpc
Rest-UV						
L01	2.63	1.34	0.81	0.86	1.20	2.11
L02	2.42	2.28	1.49	0.69	1.28	2.17
L03	1.40	0.97	0.77	0.33	0.63	1.17
L05	1.71	1.46	0.84	0.35	0.69	1.45
L07	1.13	0.90	0.81	0.33	0.60	0.95
L08	5.98	3.35	2.08	1.67	3.01	4.96
L09	18.72	1.11	0.59	2.73	8.52	13.81
L10	4.73	3.71	3.09	0.77	2.08	3.93
L11	23.77	18.56	18.56	6.12	12.21	19.41
L12	1.84	1.20	1.05	0.41	0.75	1.76
L13	4.42	3.70	1.23	1.95	2.47	3.75
L14	1.83	1.71	0.98	0.67	0.98	1.52
Rest-optical						
L01	4.87	2.15	2.44	1.28	2.11	4.01
L02	7.12	2.23	2.51	1.08	2.63	5.62
L03	5.73	1.98	1.83	0.72	2.00	4.59
L05	2.32	1.79	1.84	0.41	0.98	1.79
L07	3.95	2.89	1.96	0.62	1.51	3.18
L08	5.28	3.17	3.29	1.48	2.63	4.22
L09	20.54	3.06	2.07	5.98	10.27	14.74
L10	7.14	3.93	3.93	1.08	2.83	5.57
L11	19.13	14.52	14.52	4.83	9.82	15.43
L12	3.68	3.15	1.20	0.64	1.46	2.97
L13	11.41	5.04	5.35	2.31	5.30	9.15
L14	3.72	3.78	1.22	0.73	1.28	2.80

Notes. Size measurements from elliptical and circular aperture photometry of the original LARS images. (1) LARS id; (2) Petrosian semi-major axis; (3) circular Petrosian radius; (4) Petrosian radius at minimum of asymmetry; (5) radius containing 20%; (6) 50%; and (7) 80% of the total flux. The measurements were performed in the bands corresponding to the rest-frame UV (either F140 or F150) and to the rest-frame optical (either F775, F814, or F850). The step in semi-major axis is 1 pixel (~0.02 kpc at $z \sim 0.03$) and in circular radius is 2 pixels (~0.05 kpc at $z \sim 0.03$).

4.2. Detection of the LARS-LAEs in high-redshift surveys

The LARS-LAE galaxies show more than one bright knot, connected by filaments, in the continua. They also show an intense Lyα emission close to their centres and Lyα structures in their outskirts. The Lyα emission is accompanied by regions of absorption. As a typical trend, in increasingly shallower surveys the filaments, seen in the continua, show lower surface brightness, while their Lyα emission become increasingly localized in the galaxy centre. Only L14, the galaxy brightest in Lyα, could be detected in the shallowest Lyα survey probed here. The magnitude and flux limits for z2LARS-LAE detection are shown in Table 4.

4.3. Detection of the Lyα-faint z2LARS galaxies

In general these LARS galaxies are bright enough in UV, optical, and Hα (see Paper II) to be detected as a single source in our SExtractor run. The exception is L13 (Fig. B.3): this galaxy is detected as two possibly blended sources (dashed-line aperture in Fig. B.3) in UV and Hα, and photometry was performed locating the aperture on the (brightest) right clump. In the shallow simulated surveys (Figs. B.4–B.6) low surface brightness filaments connecting the main continuum knots disappear into the background noise making the sources appear to be composed of several clumps. In increasingly shallow surveys, fewer clumps could be detected. For example, only the brightest clump is detected for L13 at $m_{\rm rest-UV} = 29$ and $m_{\rm rest-optical} = 26$. Only L09, the brightest galaxy in Hα, could be detected in the shallowest Hα survey probed here.

In general these galaxies could not be detected in Lyα surveys shallower than $F(\mathrm{Ly}\alpha) = 3\mathrm{E}{-18}$ erg s^{-1} cm^{-2}. The galaxies presenting the strongest Lyα absorption (white pixels in Fig. B.2) of the sample could be detected only in the deepest Lyα survey probed here.

4.4. Size

The Petrosian radius measured within elliptical apertures (rP20^{ell}) is the quantity adopted for the comparison of Lyα versus continuum size estimations (Appendix A and Paper 0). The rP20^{ell} estimated in the z2LARS continuum and Lyα images could vary by up to 20% in median (Fig. 9). The variation depends on the specific morphology.

As proposed in Paper 0, we define the quantity ξ to estimate the size of Lyα with respect to the size of Hα (Eq. (1)) and continuum (Eq. (2)) emission,

$$\xi(\mathrm{Ly}\alpha/\mathrm{H}\alpha) = \frac{rP20^{\rm ell}(\mathrm{Ly}\alpha)}{rP20^{\rm ell}(\mathrm{H}\alpha)} \quad (1)$$

$$\xi(\mathrm{Ly}\alpha/\mathrm{UV}) = \frac{rP20^{\rm ell}(\mathrm{Ly}\alpha)}{rP20^{\rm ell}(\mathrm{rest-UV})}. \quad (2)$$

A ξ larger than 1 indicates that Lyα photons extend to larger scales than UV and Hα due to neutral hydrogen scattering; the

Table 3. Morphological parameters of the original LARS galaxies at $z \sim 0$.

(1) LARS	(2) G^{rP20}	(3) $G^{SB-rP20S}$	(4) M20	(5) ell	(6) $C^{\rm circ}$	(7) $C^{\rm ell}$	(8) $C^{\rm minA}$	(9) $SN_{\rm pixel}$	(10) A	(11) S
Rest-UV										
L01	0.70	0.68	–0.87	0.61	1.34	1.94	1.73	251.40	0.42	0.16
L02	0.73	0.72	–0.79	0.53	3.14	2.50	3.49	52.26	0.50	0.26
L03	0.63	0.64	–1.17	0.30	2.20	2.71	2.76	83.18	0.21	0.11
L05	0.72	0.68	–1.26	0.34	3.11	3.07	3.27	408.69	0.33	0.15
L07	0.62	0.62	–1.02	0.40	1.99	2.28	1.24	696.00	0.26	0.09
L08	0.62	0.65	–0.89	0.33	1.95	2.36	1.43	21.98	0.37	0.29
L09	0.71	0.75	–2.33	0.80	1.76	3.52	3.35	23.86	0.21	0.24
L10	0.67	0.68	–1.52	0.52	3.53	3.53	2.76	32.83	0.33	0.24
L11	0.58	0.79	–1.22	0.87	3.40	2.51	3.40	44.05	0.30	0.31
L12	0.67	0.68	–1.50	0.34	2.56	3.15	2.82	583.81	0.28	0.04
L13	0.72	0.67	–0.77	0.21	1.23	1.42	2.61	89.17	0.33	0.23
L14	0.74	0.68	–0.71	0.27	1.51	1.78	2.72	622.68	0.21	0.02
Rest-optical										
L01	0.59	0.61	–1.09	0.64	1.72	2.48	2.53	21.91	0.29	0.09
L02	0.59	0.64	–1.36	0.69	2.96	3.58	2.89	4.25	0.14	0.31
L03	0.61	0.62	–2.16	0.45	3.32	4.02	3.42	50.72	0.09	0.05
L05	0.64	0.67	–1.57	0.73	3.27	3.22	4.77	64.96	0.33	0.15
L07	0.60	0.61	–1.68	0.60	3.28	3.56	2.97	14.60	0.24	0.10
L08	0.54	0.55	–1.05	0.23	2.10	2.28	1.78	36.82	0.31	0.16
L09	0.62	0.74	–1.13	0.83	2.03	1.96	4.35	11.38	0.45	0.34
L10	0.57	0.58	–1.87	0.54	3.08	3.56	3.31	9.95	0.13	0.15
L11	0.50	0.60	–1.25	0.85	3.46	2.52	3.46	18.70	0.20	0.23
L12	0.64	0.63	–1.90	0.46	3.70	3.34	3.35	54.74	0.33	0.13
L13	0.58	0.62	–1.52	0.55	2.43	2.99	3.67	3.98	0.18	0.30
L14	0.76	0.72	–1.32	0.10	2.92	2.92	3.01	35.24	0.32	0.13

Notes. Morphological parameters estimated for the original LARS galaxies, following the equations in Appendix A. (1) LARS id; (2) Gini coefficient estimated within the fixed-size segmentation map; (3) Gini coefficient estimated within the segmentation map built from the pixels with surface brightness larger than the value corresponding to that at the Petrosian radius; (4) M20; (5) SExtractor ellipticity 1-B/A; (6) concentration from circular apertures; (7) concentration from elliptical apertures; (8) concentration corresponding to the minimum of asymmetry; (9) signal-to-noise per pixel; (10) asymmetry; (11) clumpiness. As discussed in Appendix A, we could expect an uncertainty of ∼10% in G, of <5% in M20, and of ∼20% in C. We could expect an even larger uncertainty in S. The difference in G^{rP20} and $G^{SB-rP20S}$ is generally marginal.

Table 4. Limits of detection for LARS galaxies simulated to $z \sim 2$.

ID	$m_{\rm rest-UV}$	$m_{\rm rest-optical}$	F(Lyα)	F(Hα)
	AB	AB	erg s^{-1} cm^{-2}	erg s^{-1} cm^{-2}
L01lae	28	26	8E-18	3E-18
L02lae	29	27	8E-18	1E-18
L03	29	25	3E-18	3E-18
L05lae	27	26	8E-18	3E-18
L07lae	28	26	2E-17	3E-18
L08lae	28	25	8E-18	3E-18
L09	28	27	5E-19	1E-17
L10	28	25	5E-19	1E-18
L11	28	26	3E-18	3E-18
L12	26	26	3E-18	3E-18
L13	28	27	8E-18	3E-18
L14lae	27	27	5E-17	1E-17

Notes. Almost all LARS galaxies would be detected in Lyα at a 10σ detection limit depth of 3E-18 erg s^{-1} cm^{-2}. The exceptions are L09 and L10, which show strong absorption in their Lyα images (Fig. C.4). LARS-LAEs would be detected in shallower surveys. Also, the majority of LARS galaxies would be detected in Hα at a depth of 3E-18 erg s^{-1} cm^{-2}.

galaxy presents a Lyα halo. The left panel of Fig. 10 compares ξ measured in the high-z simulated image with that of the original LARS image. Even if the rP20$^{\rm ell}$ estimated in the high-z simulation is larger than in the original image, the ξ values remain consistent within the errors. The ratio between ξ(Lyα/UV) measured in the z2LARS and original LARS images is 1.1 ± 0.8 on average. The ratios ξ (Lyα/UV) or ξ(Lyα/Hα) vary between 1 and 5 among the LARS galaxies, implying that Lyα haloes are common in the LARS sample. However, the total extension of the haloes depends on the depth of the simulated survey and the limits of detection in Lyα, UV, and Hα (Sects. 4.1−4.3). The sizes of z2LARS for each simulated survey probed here are presented in Table 5. For comparison Finkelstein et al. (2011b) reported size measurements of three LAEs at $z \sim 4.5$ of 1−2 kpc in the rest-frame UV and of 1−3 kpc in Lyα. Similarly Bond et al. (2010) estimated 2 kpc both in UV and in Lyα.

In Fig. 10, we also show

$$\xi(\text{optical/UV}) = \frac{rP20^{\rm ell}(\text{rest} - \text{optical})}{rP20^{\rm ell}(\text{rest} - \text{UV})}. \quad (3)$$

From the right panel of the figure, we see that the ratio between ξ(optical/UV) measured in the z2LARS and in the original LARS images is 1.1 ± 0.3 on average.

4.5. Ellipticity and clumpiness

As noticed in Bond et al. (2009), it is not possible to easily understand if clumps in high-z broad-band images are merging components rather than star-forming regions connected by low surface brightness structures. Gronwall et al. (2011), Bond et al. (2012) observed that the rest-frame UV emission from a typical LAE was neither smooth nor spheroidal; its ellipticity

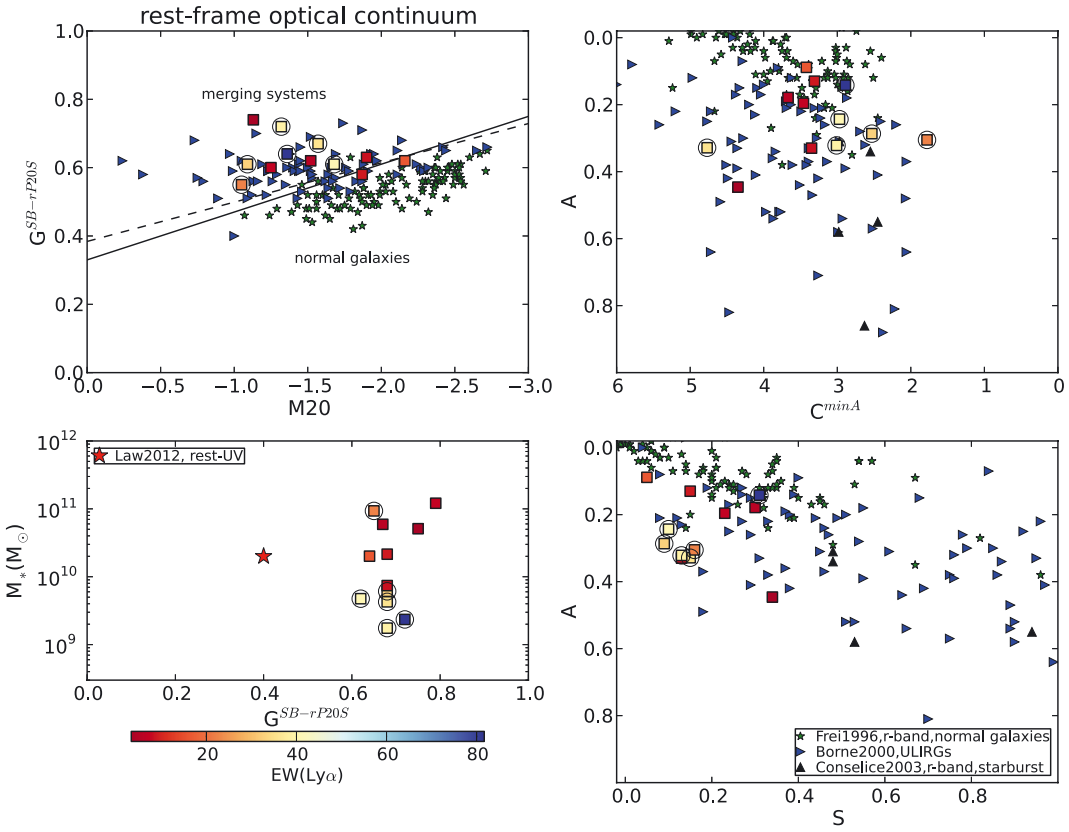

Fig. 4. Combinations of rest-frame optical morphological measurements, used in the literature as diagnostics of galaxy past and current history. $G^{SB-rP20S}$ vs. M20 (*upper left*), A vs. $C^{\mathrm{min}A}$ (*upper right*), and A vs. S (*lower right*). The *lower left* panel shows stellar mass vs. the rest-frame UV $G^{SB-rP20S}$. The typical value of $G^{SB-rP20S} = 0.4$ for the strongest Lyα emitters of the sample by Law et al. (2012) is reported as a red star. The twelve LARS galaxies analysed here are presented as squares, LARS-LAEs are rounded by open circles. The colour scale corresponds to EW(Lyα). For comparison, green stars correspond to the Frei et al. (1996) sample of normal galaxies and light blue triangles correspond to the ULIRG sample of Borne et al. (2000) as processed by Lotz et al. (2004). Black triangles correspond to a sample of starburst galaxies presented in Conselice (2003). Dashed and solid lines correspond to the separation between ULIRGs and normal galaxies, proposed by Lotz et al. (2004) and Lotz et al. (2008) respectively (see text).

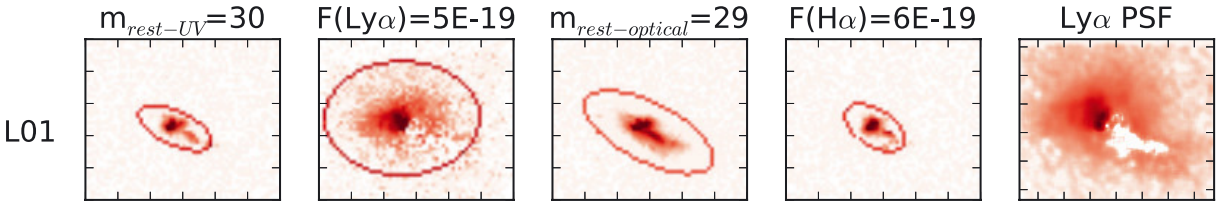

Fig. 7. Simulated $z \sim 2$ rest-frame UV, Lyα, rest-frame optical, and Hα emission for L01 as it would be observed in the deepest surveys probed here (*first four panels* starting from the *left*). The *last panel* shows the original-pixel-scale Lyα image convolved with a Gaussian kernel, resembling a ground-based seeing point spread function, PSF, of 1.32″. Every panel is 20 × 17 kpc wide. The reddish ellipses indicate SEx apertures, corresponding to the assumed detection parameters: DETECT_THRESH = 1.65, DETECT_MINAREA=30, and DEBLEND_MINCONT = 1 from Bond et al. (2009). The log colour scaling is chosen to show a visually consistent background noise.

was about 0.6, suggesting the presence of elongated structures due to merging activity or clumps of star formation. However, Shibuya et al. (2014) found that the LAEs in their sample with EW(Lyα) > 100 Å tended to be characterized by a small ellipticity both in the rest-frame UV and optical. This is supported by the theoretical results of Verhamme et al. (2012) and Laursen et al. (2009), which showed that Lyα photons could more easily escape from face-on disks (ellipticity ~0), generally characterized by low column density of HI along the line of sight.

LARS galaxies do not show any clear trend between continuum ellipticity and Lyα equivalent width (Table 3). After pixel resampling the rest-frame UV ellipticity varied by up to 60% for some of the LARS galaxies and no trend remains between continuum ellipticity and Lyα equivalent width for the z2LARS galaxies.

In shallow surveys, bright knots of star formation, seen without low surface brightness connectors, could appear aligned and lead to the galaxy appearing more elongated. Figures 11 and 12 show ellipticity versus clumpiness for a few z2LARS for which these measurements are significant. They also show how those parameters change when measured in the range of surveys probed here. Quantitatively z2LARS galaxies tend to have lower

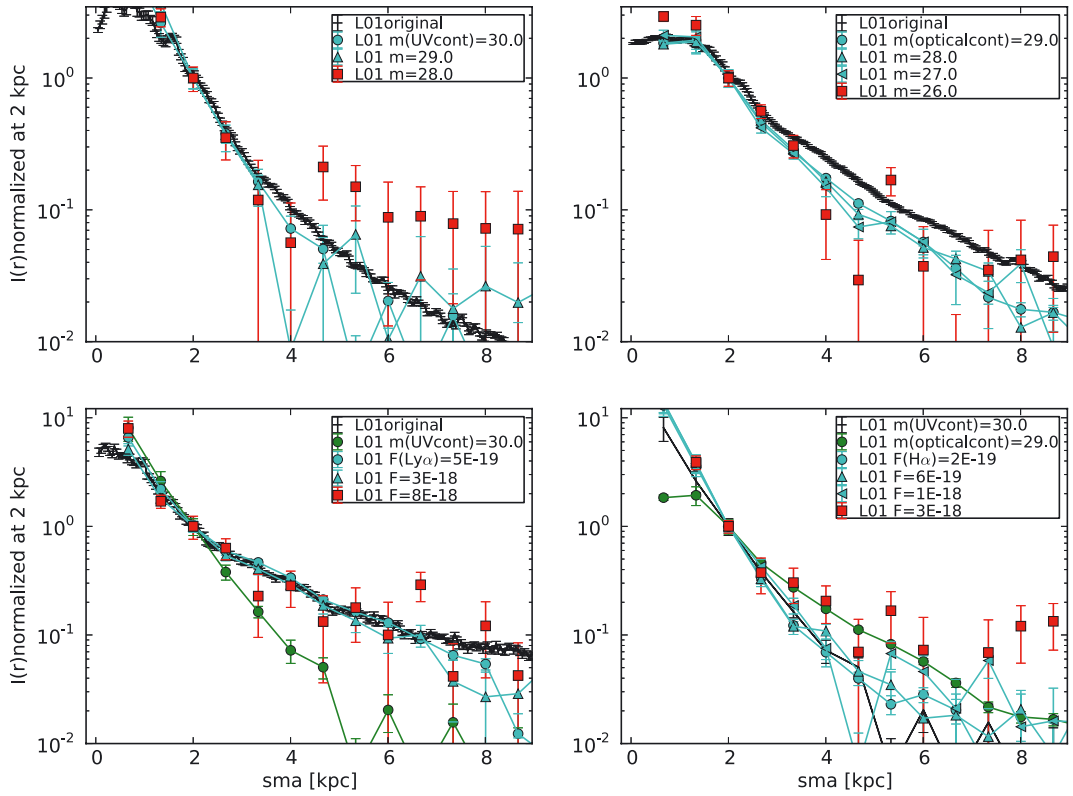

Fig. 8. Normalized surface brightness profiles of z2L01. The semi-major axis of an elliptical aperture is indicated as sma. Black points with error bars correspond to the surface brightness profile of the original LARS images in the rest-frame UV, optical, and Lyα line. The red squares represent the profiles at the limits of detection. The profiles indicated with circles(triangles) correspond to the deepest(intermediate) depth surveys. In the *upper left* panel we show the original rest-frame UV profile and the one at a depth of $m_{\rm rest-UV}$ = 30, 29(cyan) and 28(red). In the *upper right* panel the original rest-frame optical profile, the one at a depth of $m_{\rm rest-optical}$ = 29, 28, 27(cyan), and 26(red). In the *lower left* the original Lyα profile, the one at a depth of F(Lyα) = 5E-19, 3E-18(cyan), and 8E-18(red), together with the deepest-survey rest-frame UV profile (green circle and line). In the *lower right* the Hα profile at a depth of F(Hα) = 2E-19, 6E-19(cyan), and 1E-18(red), together with the deepest-survey rest-frame optical profile (green circle and line) and the deepest-survey rest-frame UV profile (black line with error bars).

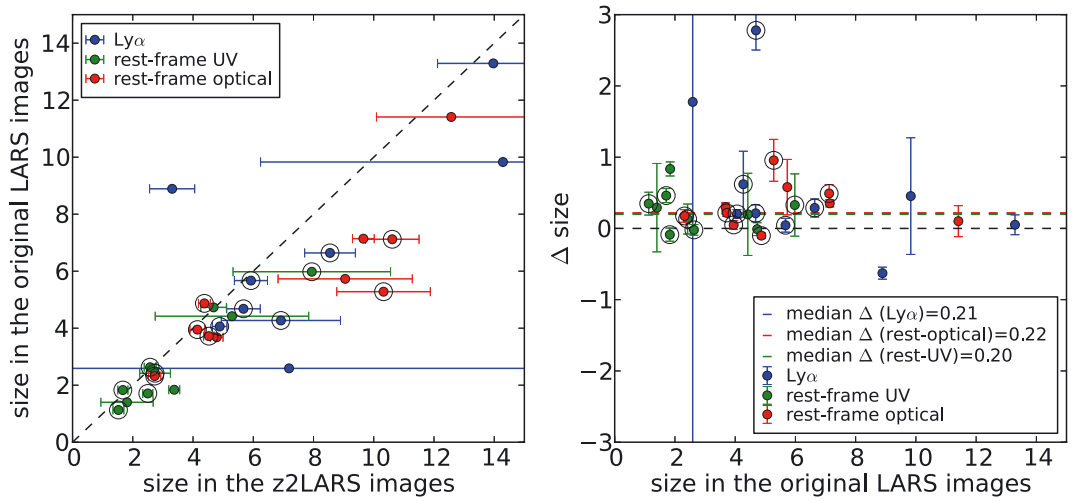

Fig. 9. *Left*: rP20$^{\rm ell}$ (kpc) measured in the original LARS images as a function of the value from the high-z simulated ones. The 1:1 relation is shown as a dashed line. *Right*: Δsize = $\frac{rP20^{\rm ell}(z2{\rm LARS}) - rP20^{\rm ell}({\rm LARS})}{rP20^{\rm ell}(LARS)}$ as a function of rP20$^{\rm ell}$ measured in the original LARS images. The black dashed line indicates Δ = 0; the dashed blue, green, and red lines the median Δ values for Lyα, rest-frame UV, and optical. Open circles indicate LARS-LAEs; blue, green, and red dots correspond to the measurements in Lyα, rest-frame UV, and optical images.

ellipticity in Lyα than in the rest-frame UV, optical continuum, and Hα. Also, z2LARS-LAEs tend to show lower S than the other LARS galaxies in Lyα.

On average the ellipticity values increase in a shallower and shallower survey when measured in the rest-frame optical. We evaluate the correlation between depth and ellipticity or clumpiness by calculating the difference between the morphological parameter measured in shallow surveys and in the deepest one. In the sample of LARS galaxies, 70% show a Spearman probability $p \sim 0.0$ and coefficient $r \sim -1$ for the correlation of ellipticity.

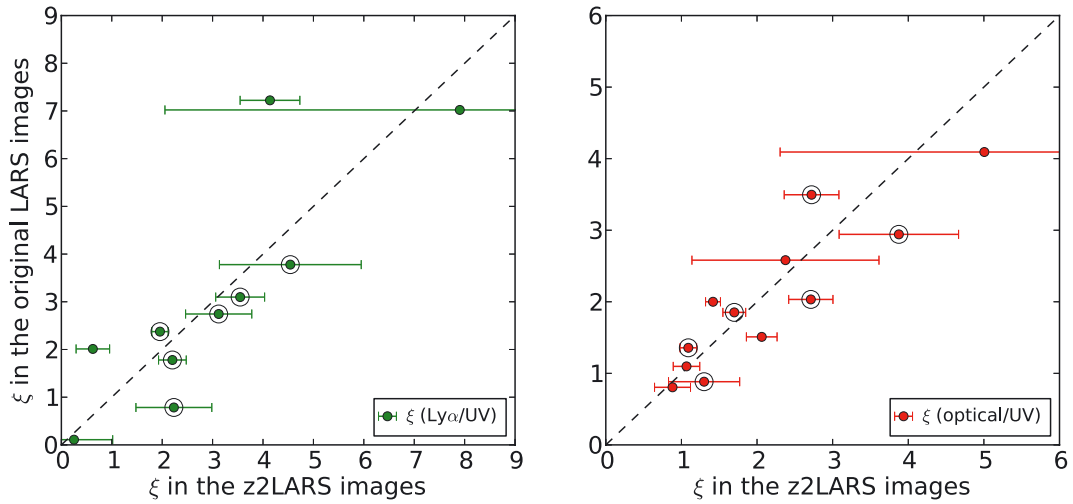

Fig. 10. ξ(Lyα/rest-UV) (*left*) and ξ(rest-optical/rest-UV) (*right*) measured in the original as a function of the regridded LARS images. Open circles indicate LARS-LAEs. The dashed line shows a 1:1 relation.

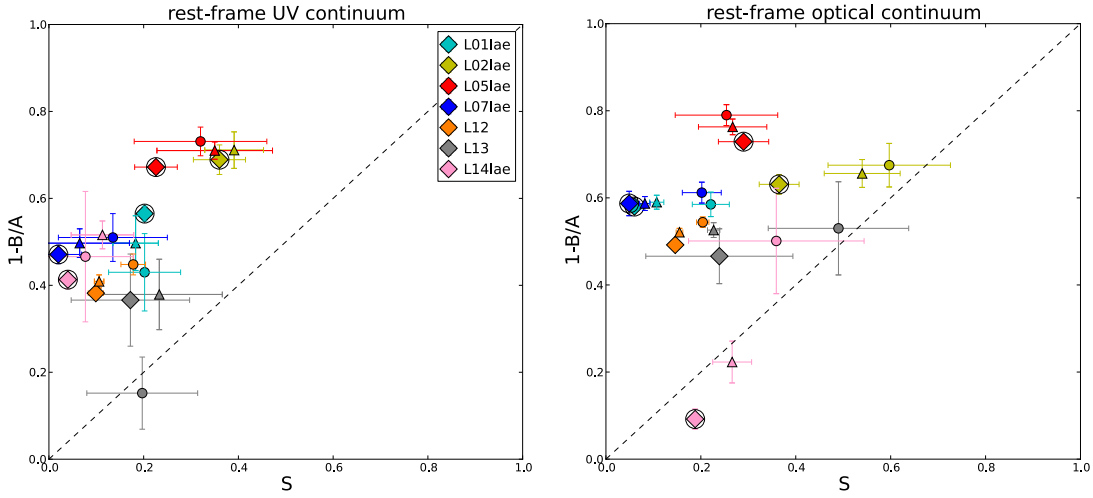

Fig. 11. Ellipticity as defined by SEx (1-B/A, where A and B are the semi-major and minor axes of the detection ellipse) as a function of clumpiness for the rest-frame UV and optical continuum. Diamonds represent z2LARS measurements in the deepest survey, triangle and circles in increasingly shallower surveys. Dashed line is a 1:1 relation drawn to aid the eye.

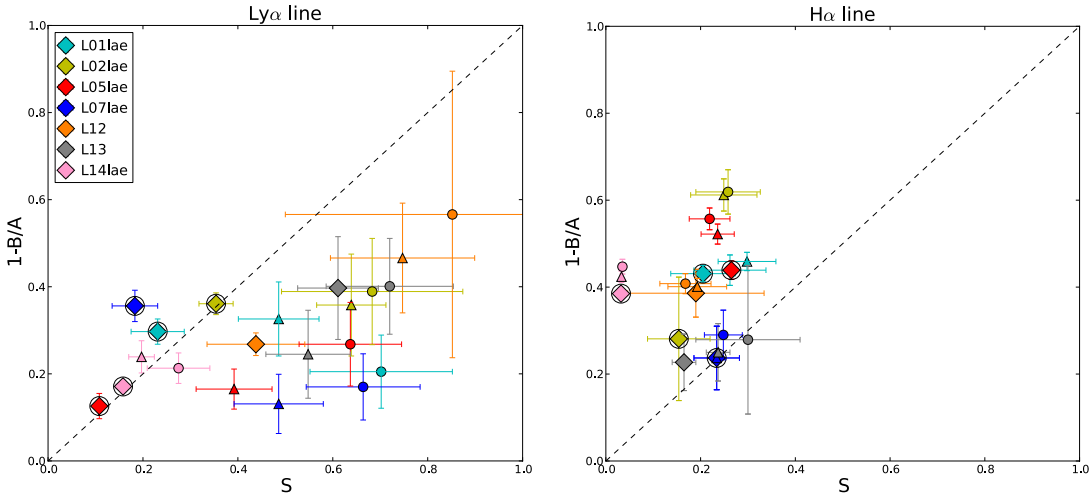

Fig. 12. Ellipticity versus clumpiness as in Fig. 11 for measurements performed in Lyα and Hα images.

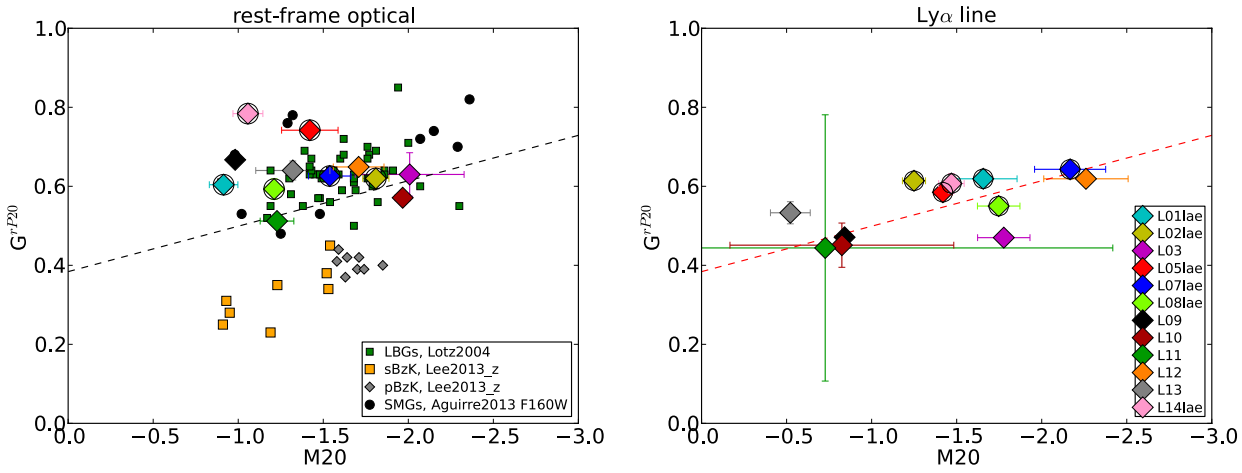

Fig. 13. *Left*: G^{rP20} vs. M20 measured in the rest-frame optical images of z2LARS (big diamonds). Open circles indicate z2LARS-LAEs. Data from the literature are presented as small symbols: LBGs detected in the *Hubble* Deep Field-North and measured by Lotz et al. (2004, green squares), passive and star-forming BzK (Lee et al. 2013, grey diamonds and yellow squares), and $z \sim 2.5$ SMGs (Aguirre et al. 2013, black circles), where the measurements are all performed on HST images. The dashed line indicates the separation between normal galaxies and merging systems by Lotz et al. (2008). *Right*: G^{rP20} vs. M20 measured in the Lyα images of z2LARS (big diamonds). The colour coding for LARS galaxies is as used throughout this paper. The dashed red line represents the rest-frame optical (*left panel*) separating region, drawn to guide the eye.

Also, 85% of the LARS galaxies show a correlation between depth and S estimated in the rest-optical. For the z2LARS-LAEs the ellipticity increases when measured in the rest-frame UV as well. Therefore, some of the high-z observations of large ellipticity and clumpy systems could be explained in terms of survey depth. Only a small change in S and ellipticity is seen in the Hα images. In Lyα we generally measure a significant increase of S in shallow surveys. Of the LARS galaxies, 85% are characterized by a correlation between depth and S when measured in Lyα. For a few galaxies the Lyα ellipticity also increases with the shallowness of the survey.

4.6. Morphological parameters of LARS at $z \sim 2$

As in the case of the original LARS images (Sect. 3.1), we performed non-parametric measurements of morphological parameters for z2LARS. To compare with high-z literature observations, we made used of the G vs. M20 diagram. We chose G^{rP20} which shows a better consistency for high-z comparisons (Scarlata et al. 2007). As shown in Appendix A, the pixel resampling has little effect on the measurements of G^{rP20} and M20 for LARS galaxies. The change of parameters owing resampling has been studied in the literature by some groups (Lotz et al. 2006; Overzier et al. 2010; Huertas-Company et al. 2014; Petty et al. 2014). The changes for irregular galaxies are in agreement with our findings for LARS galaxies. The non-parametric measurements for all the simulated surveys probed here are presented in Table 6. The left panel of Fig. 13 shows that z2LARS have morphology consistent with that of merging system, like $z \sim 2.5$ SMGs and some of the LBGs studied by Lotz et al. (2004). They tend to be separated from the location of $z \sim 2$ sBzK and pBzK galaxies (Lee et al. 2013). Some z2LARS-LAEs show a larger G^{rP20} per M20 value than the other z2LARS.

Lotz et al. (2006) built a criterion to identify merging systems based on their rest-frame UV. Since the rest-frame UV tends to be more disturbed than the optical, they defined two main regions in the G-M20 diagram. The condition M20 ≥ -1.1, typical of well-separated double or multiple bright nuclei, was used to identify major mergers, while the condition M20 < -1.6, $G > 0.6$ to identify bulge-dominated systems. The left panel of Fig. 14 shows that z2LARS galaxies have morphologies similar to that of high-z LAEs and LBGs in the rest-frame UV, and tend to be less compact than SMGs. In this diagram L01, L08, and L14 have morphologies consistent with that of major-merger systems. The non-LAE z2LARS galaxies, similar to the majority of the star-forming galaxies at high redshift, are characterized by intermediate M20 values. In the right panel of Figs. 13 and 14, we present G^{rP20} vs. M20 measured in the Lyα images. The subsample of z2LARS-LAEs tend to have lower G^{rP20} and lower M20 in Lyα than in the rest-frame optical and UV. Some of the z2LARS non-LAEs tend to have a more distorted (composed of more than one clump) morphology in Lyα than in the continua. It can be seen in Table 6 that the morphology of LARS galaxies does not change significantly in the rest-frame optical when non-parametric measurements were performed in simulated surveys with depths comparable with the limits of detection (Table 4). For a few z2LARS, G^{rP20} and M20 vary in a way that they approach the dashed line drawn in Fig. 13. In the rest-frame UV, G^{rP20} and M20 become characterized by larger uncertainties, while in Lyα z2LARS become increasingly compact and less composed of multiple structures.

5. Stacking of regridded LARS images

As extensively described in Paper 0 and II, a significant fraction of the Lyα photons in LARS galaxies is emitted from haloes. These haloes begin in the inner few kpc and extend outward to scales larger than those characterizing localized star-forming regions. Lyα maps were shown in Paper II as well as maps of Lyα/Hα ratio and dust-reddening maps. Since Hα photons are emitted directly from the HII regions (i.e., they do not scatter), a value of the Lyα/Hα ratio that exceeds that of case B recombination is most probably related to HI scattering. Dust reddening and HI scattering together can contribute to the situation in which the number of Lyα photons observed on a particular sight-line is reduced. The re-processing of ionizing photons (e.g., Humphrey et al. 2008) in a region of the galaxy different from that of the star formation could contribute to an additional production of Lyα photons and a possible extended Lyα emission. In this case, however, Hα radiation will also be

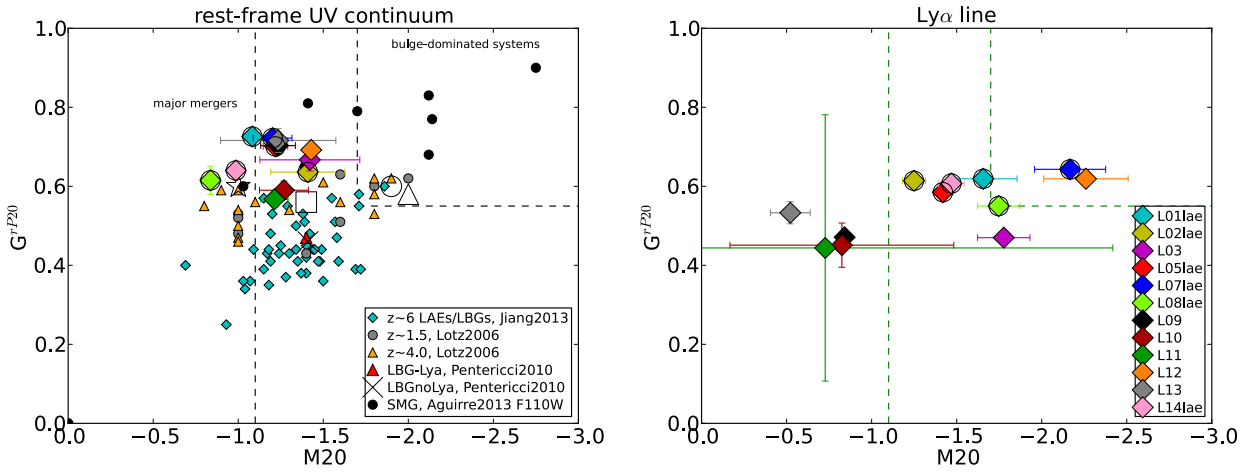

Fig. 14. *Left*: G^{rP20} vs. M20 measured in the rest-frame UV images of z2LARS (big diamonds). Open circles indicate z2LARS-LAEs. Small symbols are data from literature: LAEs and LBGs at $z > 6$ (Jiang et al. 2013, cyan diamonds), GOODS $z \sim 1.5$ and GOODS/UDF $z \sim 4$ galaxies (Lotz et al. 2006, grey circles and yellow triangles), mean values for $z \sim 3$ LBGs with and without Lyα emission (Pentericci et al. 2010, red triangle and black cross), and $z \sim 2.5$ SMGs (Aguirre et al. 2013, black circles), where the measurements are all performed in HST images. For comparison we also show the local galaxies regridded to be at $z \sim 1.5$ by Lotz et al. (2006): an elliptical (open circle), an Sb (open triangle), an Scb (open square), and a merging galaxy (open star). The dashed lines indicate the criteria introduced by Lotz et al. (2006) to identify major mergers and bulge-dominated systems. *Right*: G^{rP20} vs. M20 measured the Lyα images of z2LARS (big diamonds). The dashed green lines represent the rest-frame UV (*left panel*) separating regions, drawn to aid the eye. The colour coding for LARS galaxies is the same as in Fig. 13.

produced at large radii by the same recombinations that make Lyα. The availability of Hα images, together with those of Lyα, has favoured an interpretation in which HI scattering plays a key role in Lyα emission, but it has proven difficult to disentangle the contribution of other factors. However, HI scattering would also produce a certain degree of polarization in the Lyα emission (e.g., Humphrey et al. 2013b; Hayes et al. 2011). At high redshift, Lyα haloes have been detected only in a minority of cases, indicating that their detection is challenging.

5.1. Literature results

Rauch et al. (2008) stacked Lyα spectra of a sample of faint ($V >$ 25.5 for 80% of the sample) spectroscopically detected galaxies at $2.67 < z < 3.75$, reaching a Lyα surface brightness limit of ~2E-19 erg s^{-1} cm^{-2} arcsec^{-2} at 1σ. The resulting Lyα profile extended up to ~30 kpc from the centre. Matsuda et al. (2012) stacked narrow-band images of large subsamples of LBGs, separated based on their environment. They found that galaxies in overdense regions tend to show Lyα emission on scales up to 40−60 kpc, and are larger than those of isolated galaxies. This could imply that Lyα haloes follow the dark matter distribution. Steidel et al. (2011, hereafter S11) also stacked Lyα images of subsamples of LBGs at $z \sim 2.65$, segregated by Lyα equivalent width. The galaxies came from surveys of three different fields, which were also characterized by over-densities. The stack of the entire sample reached a Lyα surface brightness limit of ~1E-19 erg s^{-1} cm^{-2} arcsec^{-2} (1σ), while the LAE (EW(Lyα) > 20 Å) subsample reached ~2.4E-19 erg s^{-1} cm^{-2} arcsec^{-2}. They found that the stacked Lyα profiles had a characteristic size up to 9 times larger than the stellar continua. Their detected Lyα emission extended up to 80 kpc from the centre of the stacked source.

By stacking images of 187 narrow-band selected Lyα emitters at $z \simeq 2.07$, Feldmeier et al. (2013) found no evidence of extended Lyα emission, but did observe a 5−8 kpc halo in a stack of about 200 LAEs at $z \simeq 3.1$. These field-galaxy stacks reached a Lyα surface brightness 1σ limit of just 9.9E-19 erg s^{-1} cm^{-2} arcsec^{-2} at $z \simeq 2.07$ and 6.2E-19 erg s^{-1} cm^{-2} arcsec^{-2} at $z \simeq 3.1$. Recently, Momose et al. (2014, hereafter M14) succeeded in detecting extended haloes, by stacking over 3500, 300, and 350 narrow-band detected LAEs at $z \sim 2.2$, ~3.1, and $z \sim 5.7$ from Subaru surveys (not necessarily in overdense regions). They reached a Lyα surface brightness 1σ limit of 1.6E-20, 1.7E-19, and 5.5E-20 erg s^{-1} cm^{-2} arcsec^{-2}, respectively. Both these last two studies performed LAE selection in deep (5σ detection limit of 25 AB for Feldmeier; Guaita et al. 2010; Gronwall et al. 2007) and very deep (5σ detection limit of 25.1–25.7 AB for Momose; Nakajima et al. 2012) narrow-band images. Also, they treated the sources of uncertainty in a very careful way. However, the detected haloes ($r_e \sim 8$ kpc at $z = 2.2$) were not as extended as the ones claimed by S11 ($r_e \sim 25$ kpc at $z = 2.65$). A few attempts to detect Lyα haloes from individual high-z LAEs were performed by Bond et al. (2010) and Finkelstein et al. (2011a) in HST-filter images. Bond et al. (2010) presented a morphological study of LAE Lyα emission at $z \simeq 3.1$ (F502N filter, 1σ detection limit of 3E-17 erg s^{-1} cm^{-2} arcsec^{-2} for 1 arcsec source). Their images were very shallow and did not show significant extended haloes (ξ(Lyα/UV) ~ 1, Table 5). An estimation at $z \sim 4.5$ was presented in Finkelstein et al. (2011a) (*F658N* filter, 1σ detection limit of about 2E-18 erg s^{-1} cm^{-2} for 1 arcsec source). They studied Lyα emission from three spectroscopically confirmed LAEs and found evidence of Lyα haloes in two of them (ξ(Lyα/UV) ~1.5).

5.2. Stacking procedure and stacked surface brightness of LARS at high redshift

By following the steps listed in Sect. 2, we simulated the appearance of LARS galaxies at $z \sim 2$ and $z \simeq 5.7$. After adding noise to the simulated high-z images, we stacked the observations of individual galaxies the same way it is done at high redshift to increase the signal-to-noise. We used the

Table 7. Size of stacked Lyα and continuum images.

LARS stack	$r_{\rm circ}^{\rm SEx}$ kpc	rP20$^{\rm ell}$ kpc	rP20$^{\rm circ}$ kpc	rP20$^{\rm min}A$ kpc	r_{20} kpc	r_{50} kpc	r_{80} kpc
$z \sim 2$							
F(Lyα) = 5E-19							
LARS-LAE	5.26	6.67	6.00	3.34	1.33	2.67	5.34
LARSaverage	8.05	> 12	> 12	8.01	2.84	7.84	> 12
F(Lyα) = 3E-18							
LARS-LAE	3.55	6.84	5.00	3.67	1.50	2.67	5.67
LARSaverage	4.84	> 12	> 12	7.00	2.84	7.34	> 12
F(Lyα) = 2E-17							
LARS-LAE	2.16	4.00	5.34	3.67	1.17	2.50	4.00
LARSaverage	2.54	7.00	9.01	4.00	1.83	3.84	6.84
$z \simeq 5.7$							
F(Lyα) = 5E-19							
LARS-LAE	2.40	4.70	6.34	3.52	1.17	2.35	4.35
LARSaverage	2.72	11.98	11.75	5.87	2.11	5.17	10.34
F(Lyα) = 3E-18							
LARS-LAE	0.81	4.35	3.52	2.82	1.29	2.47	4.11
LARSaverage	0.82	5.05	3.29	4.70	1.76	3.17	5.17
$z \sim 2$							
$m_{\rm rest-UV}$ = 30							
LARS-LAE	2.28	2.17	1.33	1.33	0.50	1.00	1.83
LARSaverage	3.09	4.34	3.00	1.67	0.67	1.50	3.50
$z \simeq 5.7$							
$m_{\rm rest-UV}$ = 30							
LARS-LAE	1.28	1.88	1.41	0.94	0.35	0.82	1.53
LARSaverage	1.45	3.76	1.64	1.17	0.59	1.29	3.29

Notes. Size measurements from elliptical and circular aperture photometry. For three(two) simulated survey depths, we reported the Lyα emission sizes of the two stacks (LARS-LAE, LARSaverage) at $z \sim 2 (z \simeq 5.7)$. We also reported the continuum emission sizes of the two stacks in the lower part of the table at a 10σ detection limit of $m_{\rm rest-UV} = 30.0$. F(Lyα) is given in erg s^{-1} cm^{-2}.

IMCOMBINE task in *iraf.images.immatch* to (average) stack every galaxy at the position of SExtractor centroid. We generated an average (LARSaverage), median stack of all the twelve high-z LARS galaxies (like in M11), and also an average stack of the six LARS-LAEs. It was only meaningful to look at the stacked profiles up to 12 kpc, which was the physical scale probed by the ACS/SBC detector common to all LARS images. However, narrow-band observations at high redshift are able to probe much larger scales. As the median stack provided very similar results as the average one, we only reported results from the LARS-LAE and LARSaverage stacks in the tables and figures. We chose to combine individual galaxy frames from simulated survey depth of F(Lyα) = 5E-19, 3E-18, 2E-17, and 1E-15 erg s^{-1} cm^2. The central value of F(Lyα) = 2E-17 is comparable to recent ground-based narrow-band surveys. The shallowest value was chosen to match the depth of Bond et al. (2010). At this depth we did not detect any Lyα emission from the stacks. The final depths depended on the number of sources in the stack, F(Lyα)/ $\sqrt{12}$ for LARSaverage and F(Lyα)/ $\sqrt{6}$ for LARS-LAEs. We applied the same code we ran on the individual z2LARS galaxies to obtain surface brightness profiles (Fig. 15) and sizes (Table 7) of the stacks at $z \sim 2$ and $z \simeq 5.7$. The LARS-LAE Lyα profile was the most peaked in the centre, and was also the most affected by background noise at large radii. The Sérsic indices of the LARS-LAE stack profiles were found to be 3.4 and 2.1, while the ones of the LARSaverage stacks are 2.5 and 2.0 at $z \sim 2$ and $z \simeq 5.7$, respectively.

We find that a depth of F(Lyα) = 5E-19 erg s^{-1} cm^{-2} (∼1.4E-19 erg s^{-1} cm^{-2} after stacking twelve sources) enables us to recover Lyα haloes in the stacks of LARS galaxies at both $z \sim 2$ and $z \simeq 5.7$. A depth of F(Lyα) = 2E-17 erg s^{-1} cm^{-2} (∼5.8E-18 erg s^{-1} cm^{-2} after stacking twelve sources) is more realistic in terms of current surveys. Even the brightest galaxy (L14) would hardly be detectable individually. In a simulated $z \simeq 5.7$ survey with depth of F(Lyα) = 3E-18 erg s^{-1} cm^2 (∼0.9E-18 erg s^{-1} cm^{-2} after stacking twelve sources), the Lyα surface brightness profile reached the level of the background noise at a radius of 5 kpc.

In Fig. 16 we compare the rest-frame UV and Lyα line surface brightness. The figure shows that the UV profiles for the LARS-LAEs and LARSaverage stacks are very similar. They are also steeper than any other Lyα-stack at both redshifts, showing Sérsic indices $n \sim 9$ and $n \sim 11$ at $z \sim 2$ and $z \simeq 5.7$, respectively. The consequence of this is that the sizes of the Lyα-stacks are generally larger than the continuum ones (Paper 0, Table 7). The profile of the LARSaverage stack (composed of both EW(Lyα) > 20 Å and EW(Lyα) < 20 Å sources) was also shallower and more extended than that of the LARS-LAEs; i.e. the Lyα emission of the LARS-LAE stack was more compact. As we described in Sect. 3.2, there are no unique conditions for Lyα photons to escape or unique morphologies. The conditions that make a galaxy a Lyα emitter (mainly Lyα flux concentrated around rest-frame UV bright star-forming regions) produce a consistent surface brightness profile, while variations in the dust and HI contents and distributions, which made Lyα photons eventually escape along the line of sight, produce a more complex, patchy, and extended emission.

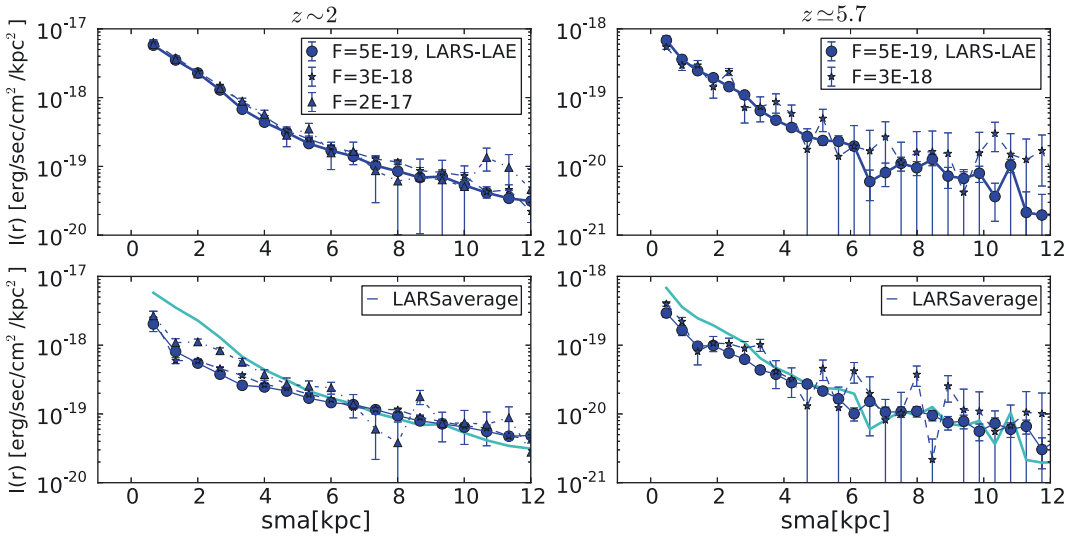

Fig. 15. Lyα surface brightness profiles of the two stacks: LARS-LAE (*upper*) and LARSaverage (*lower*; see text for details). *Left* and *right panels* show the profiles at $z \sim 2$ and 5.7, respectively, corresponding to three and two 10σ detection limits (blue circles, stars, and triangles). The cyan solid line represents the LARS-LAE profile of the deepest simulated survey and it is shown in the *lower panels* for comparison. The difference in the surface brightnesses in the *left* and *right panels* is the result of surface brightness dimming. The error bars correspond to the shallowest survey in each panel; for the other depths they are usually smaller than the symbols. The large error bars at sma >5 kpc are produced by background noise.

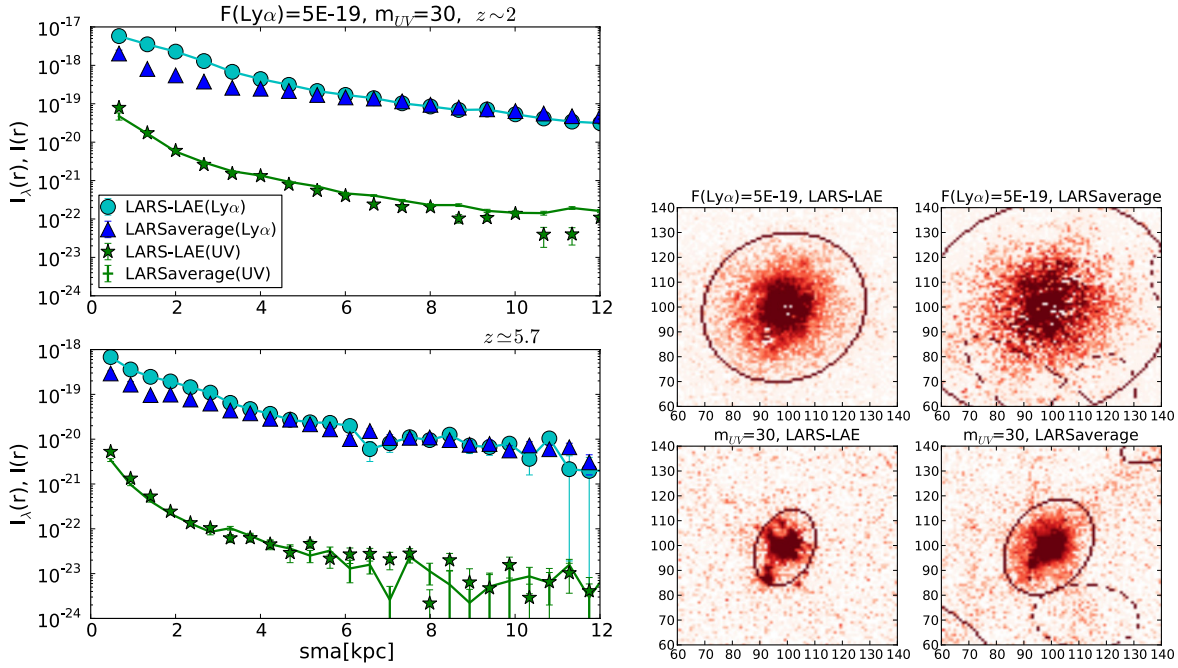

Fig. 16. *Left*: surface brightness profiles for Lyα (units of erg s^{-1} cm^{-2} kpc^{-2}) at $z \sim 2$ (*upper panel*). LARS-LAEs are shown with the cyan circles and line, and LARSaverage with (blue triangles). Rest UV profiles (units of erg s^{-1} cm^{-2} kpc^{-2} Å^{-1}) are shown for the LARS-LAE sample (green stars) and LARSaverage (green line with errorbars). The *lower* panel shows the equivalent profiles at $z = 5.7$. *Right*: from the *upper left* to the *lower right*: Lyα for the LARS-LAE and LARSaverage stacks; rest-frame UV continuum for LARS-LAEs and LARSaverage. The logarithmic colour scale is adjusted to match the background level. The elongated structures in the LARSaverage continuum frame come from L09 (vertical) and L11 (diagonal). The whitish structures in the LARSaverage Lyα come from the same galaxies, which are weak Lyα emitters but show strong absorption centrally. The cut-out size is about 15 kpc.

5.3. Ground-based PSF convolution and stacking of LARS at high redshift

To be able to properly compare with current observations at $z \sim 2$ and $z \simeq 5.7$, we convolved LARS images with ground-based PSF (Fig. 17). As the ground-based PSF is much larger than the HST one, we applied a Gaussian kernel with σ = PSF(pixel)/2.3548, using the GAUSS task in *iraf.images.imfilter*. Feldmeier et al. (2013) data at $z \simeq 2.07$ exhibited a 1.4″ PSF in narrow-band observation and 1″ in the broad band. S11 observations at $z \simeq 2.64$ were performed in similar weather conditions (PSF = 0.8″−1.2″). The measurements reported in M14 were performed on frames smoothed to a *FWHM* = 1.32″. To be able to compare with their observations

Table 8. Size of the LARS-LAE stack convolved with ground-based PSF.

LARS stack	$r_{\rm circ}^{\rm SEx}$ kpc	rP20$^{\rm ell}$ kpc	rP20$^{\rm circ}$ kpc	rP20$^{\rm min}A$ kpc	r_{20} kpc	r_{50} kpc	r_{80} kpc
$z \sim 2$							
F(Lyα) = 5E-19							
LARS-LAE	5.26	6.67	6.00	3.34	1.33	2.67	5.34
Feldmeier2013, $r_{\rm n}$						5.4	
LARS-LAE, PSF, F	9.40	9.51	9.34	6.00	3.00	5.00	7.84
Momose2014, $r_{\rm n}$						7.9	
LARS-LAE, PSF, M	9.21	9.34	9.01	5.67	2.84	4.84	7.67
Steidel2011, $r_{\rm n}^{\rm LAEonly}$						28.4	
$m_{\rm rest-UV}$ = 30							
LARS-LAE	2.28	2.17	1.33	1.33	0.50	1.00	1.83
LARS-LAE, PSF, F	5.69	5.50	5.34	> 12	2.00	3.34	4.67
LARS-LAE, PSF, M	6.40	6.67	6.67	4.34	2.50	4.00	5.67
Steidel2011, $r_{\rm n}^{\rm LAEonly}$						2.9	
$z \simeq 5.7$							
F(Lyα) = 5E-19							
LARS-LAE	2.40	4.70	6.34	3.52	1.17	2.35	4.35
Momose2014, $r_{\rm n}$						5.9	
LARS-LAE, PSF, M	6.60	9.28	7.99	4.70	2.35	4.11	7.28
$m_{\rm rest-UV}$ = 30							
LARS-LAE	1.28	1.88	1.41	0.94	0.35	0.82	1.53
LARS-LAE, PSF, M	5.59	5.99	7.52	4.46	2.00	3.29	4.93

Notes. Sizes for the LARS-LAE stack before and after convolving with Feldmeier et al. (2013) (PSF, F) and Momose et al. (2014) (PSF, M) ground-based PSF. The values correspond to the Lyα and rest-frame UV continuum images. For reference we report the e-folding parameters of the best-fit exponential profile, $I(r)$, of the observed surface brightness by Feldmeier et al. (2013), by Momose et al. (2014), and by Steidel et al. (2011), where $I(r) \propto \exp(-r/r_{\rm n})$ and $r \gtrsim 10$ kpc.

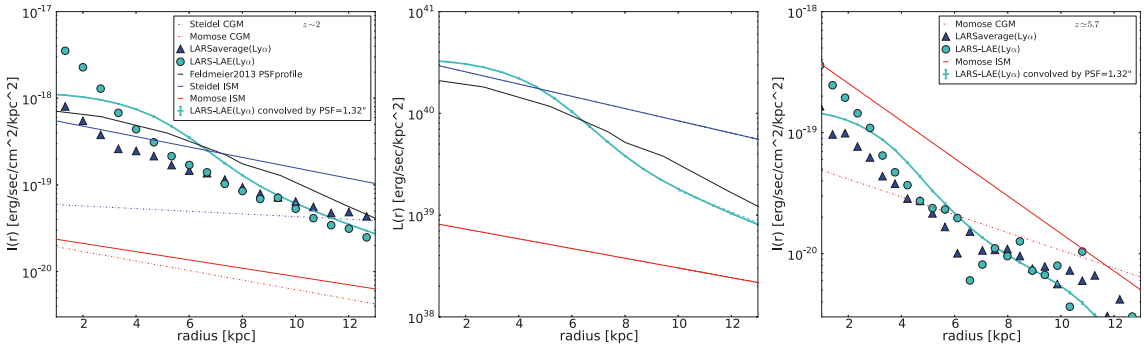

Fig. 17. *Left*: Lyα surface brightness, $I(r)$, of the $z \sim 2$ LARS-LAE and LARSaverage stacks, before convolution with ground-based PSF (cyan circles and blue triangles). The PSF-convolved LARS-LAE stack is shown with the cyan line. The ground-based PSF profile from Feldmeier et al. (2013) is shown as a black line. The blue and red dashed-dotted lines represent the circumgalactic medium, as fit by Steidel et al. (2011) and Momose et al. (2014) at $z \simeq 2.2$, we extrapolated inwards. The blue and red solid lines represent the $I(r)$ fit on scales of 10−20 kpc derived from Fig. 9 of Steidel et al. (2011) and Fig. 3 of Momose et al. (2014). *Middle*: luminosity per kpc^2 for our PSF-convolved LARS-LAE stack in Lyα (cyan line), for the ground-based PSF profile from Feldmeier et al. (2013, black line), for the 10−20-kpc-scale fit from Steidel et al. (2011, blue line) and Momose et al. (2014, red line). *Right*: Lyα surface brightness of the $z \simeq 5.7$ LARS-LAE and LARSaverage stacks before convolving with ground-based PSF (cyan circles and blue triangles) together with that of the PSF-convolved LARS-LAE stack (cyan line). The red dashed-dotted line represents the circumgalactic medium fit by Momose et al. (2014) at $z \simeq 5.7$, we extended inwards. The red line shows the fit on scales of 5−15 kpc derived from Fig. 3 of Momose et al. (2014).

at both $z \simeq 2.2$ and $z \simeq 5.7$, we convolved line and continuum images with that same Gaussian kernel, before stacking. This convolution produced a profile close to Gaussian in the stacked images of both continuum and Lyα; the central peak was suppressed and, as a consequence, the profile became shallower. However, the stacked Lyα profile remained more extended than that of the rest-frame UV (Table 8).

In the studies mentioned earlier the surface brightness of the circumgalactic medium (CGM) was estimated by fitting an exponential curve to radial profiles that excluded the first 2″ (∼17 kpc at $z \sim 2$ and ∼11 kpc at $z \sim 5.7$). Inside the first 2″, emission from the interstellar medium (ISM) dominates over that from the CGM. Moreover, the ground-based PSF will most likely dominate on these (and smaller) scales.

A fair comparison with high-z observations should have been performed to radii larger than those allowed by our HST observations, in which we mainly detected Lyα photons coming also from the interstellar media. Looking at Fig. 9 of S11 and Fig. 3 of M14, we derived the high-z Lyα profiles on scales of 10−20 ($z \sim 2$) and 5−15 ($z \simeq 5.7$) kpc, resembling the profiles typical of high-z interstellar media, with some contribution from the PSF. We show them in Fig. 17, labelled as

"Steidel ISM" and "Momose ISM". The surface brightness of M14 stacked sample at $z \simeq 2.2$ was more than one order of magnitude fainter than Steidel's and ours. LARS surface brightness profile was as bright as Steidel's one and steeper than S11 and M14 samples. The characteristic scale of a fitted exponential profile, $I(r) \propto \exp(-r/r_n)$ was $r_n = 4$, almost half the value we calculated for S11 and M14 ISM profiles. At $z \sim 5.7$ we obtained a similar slope profile as in M14, with $r_n \sim 2.7$.

6. Discussion

In Sect. 3, we have presented the morphological properties of LARS galaxies; in Sect. 4, we have described the results of the test of simulating LARS galaxies at $z \sim 2$, following the methods explained in Sect. 2; in Sect. 5, we have performed the stacking of individual LARS galaxy frames to simulate their typical extended Lyα emission at $z \sim 2$ and $z \simeq 5.7$. Here we discuss the main results.

6.1. Local Universe LARS

As described in Paper II, LARS galaxies are irregular, star-forming galaxies. Compared to the non-LAE LARS galaxies, the LARS-LAEs are younger and are characterized by lower star-formation rates, by Lyα escape fractions larger than 10% (except L08), by low dust content in terms of the ratio Hα/Hβ, and by lower masses. Figures 2 and 3 tell us that the LARS galaxies have sizes, stellar masses, and rest-frame absolute magnitudes similar to those of LBAs, and that they are also comparable to $2 < z < 3$ star-forming galaxies. The stellar masses of the LARS galaxies tend to be larger than those estimated for LAEs at $z \sim 2$–3. Even if most of the LARS-LAEs have Lyα luminosities twice fainter than those of high-z Lyα emitters, they have stellar masses and sizes comparable to those of the subsample of the most massive LAEs from Guaita et al. (2011) and Bond et al. (2012). Therefore, LARS galaxies are analogues of 10^9–10^{11} $M_\odot$ high-z star-forming galaxies; they also share some properties with the most massive Lyα emitters at high z.

The ratio between half-light radii estimated in the rest-frame optical and rest-frame UV have been adopted in the literature to identify the presence of multiple stellar populations. Within LARS, this ratio varies from 0.8 to 3, with a median value larger than 1 (~1.4). This shows that the young stellar populations are more localized than the old ones, consistent with the findings for $z \sim 2$ SMGs (Swinbank et al. 2010), sBzK (Yuma et al. 2012), and star-forming galaxies at $1.4 < z < 2.9$ (Bond et al. 2011).

The optical morphologies of LARS are typical of irregular or starburst galaxies and merging systems. They vary from the typical of early-stage mergers to closely-gathered clumps of intense star-formation. G and M20 are smaller when measured in Lyα than in the rest-frame UV. However, they are comparable when measured in the rest-frame optical and in Lyα (Fig. 6). This indicates quantitatively that the Lyα emission of LARS galaxies is generally characterized by one component in a structure that tends to be more extended in Lyα than in the bright UV continuum and seems to follow the entire galaxy stellar populations. Also, the LARS-LAEs are the ones characterized by the highest concentration, lowest asymmetry and lowest clumpiness in Lyα. A Lyα emitting galaxy with these properties would easily satisfy the EW(Lyα) requirement adopted at high redshift to identify Lyα emitters.

With the aim of identifying any continuum morphological property that characterizes Lyα emitters and star-forming galaxies, we study the correlations between morphological and physical parameters in Table 9. The LARS galaxies characterized by larger EW(Lyα) tend to be smaller in the rest-frame UV and optical than the other galaxies. They also present a more symmetric Lyα emission. The galaxies which are younger (Age≤10 Myr), less massive ($M_* < 10^{10}$ $M_\odot$), and characterized by larger specific star-formation rate (dust-corrected $sSFRuv > -9.3$ yr^{-1}) tend to present larger Gini coefficient for a fixed M20 value. These are mainly the LARS-LAEs where the merging components appear separated, like in early-stage mergers. In Fig. 18 we show the G vs. M20 diagram, in which the colour scale corresponds to the integrated physical parameters (Paper II).

In Lyα, LARS-LAEs tend to be composed of one bulge-like component and to harbour lower S and ellipticity. The other LARS galaxies are composed of patchy Lyα emission (see also Appendix B). Some LARS galaxies with large $E(B-V)$neb tend to be characterized by the lowest M20 in the rest-frame optical, typical of a bulge-like morphology. According to these results, it seems that early-stage mergers could be characterized by younger stellar populations and symmetrical, somewhat homogeneous Lyα emissions, which could satisfy high-z LAE selections. Late-stage mergers could instead be characterized by turbulent star-formation episodes and, as a consequence, patchy Lyα emissions, just like the ones observed within one galaxy with numerous star-forming regions. This may indicate that the clumpy Lyα emitting galaxies observed at high redshift (Bond et al. 2012; Gronwall et al. 2011; Shibuya et al. 2014) could also be experiencing early-stage merging events (Cooke et al. 2010). Of the twelve LARS galaxies, whose continuum morphologies are consistent with them being merging systems, six are LAEs. This does not mean that every observed LAE must necessarily be a merging system (Shibuya et al. 2014; Law et al. 2012). However, we can not verify the claim by Shibuya et al. (2014) that mergers are rare in LAEs with EW(Lyα) > 100 Å, because LARS galaxies all present lower Lyα equivalent widths.

6.2. LARS galaxies simulated to be at z ~ 2

To investigate the detectability of LARS galaxies and haloes at high redshift, we performed simulations. The LARS galaxies were resampled at $z \sim 2$ as described in Sect. 2.3. We find that the effects of pixel resampling and simulated survey noise are dependent on the irregular structures of each individual galaxy.

First of all we defined the detection limits in the continuum and line images (Table 4). In a survey shallower than the detection limit, the background noise dominates the continuum and line surface brightness profiles. Interestingly all LARS galaxies would be detected in the rest-frame UV in surveys like HUDF09 and GOODS, and at the rest-frame optical in a survey like CANDELS (deep), if located at $z \sim 2$. However, even more interesting is that Lyα emission extended up to 5 kpc would be visible in 70% of the sample at a 10σ depth of 3E-18 erg s^{-1} cm^{-2} (Table 5 and Appendix C). The LARS galaxies characterized by the faintest integrated Lyα flux show an even more extended emission. This should be taken into account when designing Lyα spectroscopic observations (see also the discussion in Paper I), which aim to detect as much of the Lyα flux as possible. In the current Lyα surveys (typically characterized by F(Lyα) > 2E−17 erg s^{-1} cm^{-2}) only L14, the brightest LARS-LAE, would be detected. Even if the Lyα size can be as large as 5 times the UV, the extremely detailed Lyα structures (Figs. 1 and 7) could only be identified in the original HST-resolution images.

Table 9. Spearman coefficient and probability of the correlations between morphological and physical parameters.

Parameter	rP20^{ell}	$G^{SB-rP20S}$	M20	$C^{min}A$	A	S	ell	ξ(Lyα/rest-UV)
Rest-UV								
EW(Lyα)	**(–0.64, 0.03)**	(0.25, 0.44)	(0.49, 0.11)	(–0.20, 0.53)	(0.22, 0.50)	(–0.29, 0.37)	(–0.11, 0.74)	
fesc(Lyα)	(–0.22, 0.48)	(0.24, 0.45)	(0.43, 0.16)	(0.09, 0.77)	(0.38, 0.22)	(0.01, 0.98)	(0.18, 0.59)	
Age	(0.52, 0.08)	(0.01, 0.98)	(–0.41, 0.18)	(0.11, 0.75)	(0.20, 0.54)	(0.68, 0.01)	(0.30, 0.34)	
*sSFRuv*_corr	(–0.57, 0.05)	(0.07, 0.84)	(0.25, 0.43)	(0.00, 0.99)	(–0.30, 0.34)	(–0.74, 0.01)	(–0.16, 0.61)	
M_*	(0.74, 0.01)	(0.06, 0.86)	(–0.33, 0.30)	(–0.02, 0.96)	(0.09, 0.78)	(0.63, 0.03)	(0.16, 0.62)	
$E(B-V)$neb	(0.01, 0.97)	(–0.44, 0.15)	(–0.20, 0.53)	(–0.23, 0.48)	(–0.31, 0.32)	(–0.13, 0.69)	(–0.42, 0.17)	
Rest-optical								
EW(Lyα)	**(–0.60, 0.04)**	(0.24, 0.46)	(–0.03, 0.93)	(–0.57, 0.05)	(–0.13, 0.70)	(–0.36, 0.25)	(–0.18, 0.57)	
fesc(Lyα)	(–0.38, 0.22)	(0.11, 0.73)	(0.24, 0.44)	(–0.31, 0.33)	(0.01, 0.98)	(0.03, 0.93)	(0.24, 0.46)	
Age	(0.58, 0.05)	**(–0.62, 0.03)**	(0.05, 0.88)	(–0.17, 0.60)	(–0.39, 0.21)	(0.26, 0.42)	(0.01, 0.98)	
*sSFRuv*_corr	(–0.69, 0.01)	**(0.62, 0.03)**	(–0.16, 0.62)	(0.08, 0.81)	(0.50, 0.10)	(–0.27, 0.40)	(–0.01, 0.98)	
M_*	(0.66, 0.02)	**(–0.55, 0.07)**	(0.24, 0.46)	(0.21, 0.51)	(–0.13, 0.70)	(0.36, 0.25)	(0.14, 0.66)	
$E(B-V)$neb	(0.08, 0.81)	(–0.32, 0.31)	(–0.42, 0.17)	(0.20, 0.54)	(–0.10, 0.75)	(–0.18, 0.58)	(–0.41, 0.18)	
Lyα								
EW(Lyα)	(–0.22, 0.53)	(0.51, 0.09)	(0.03, 0.93)	(0.59, 0.04)	**(–0.70, 0.01)**	(–0.61, 0.04)	(–0.42, 0.17)	(0.25, 0.49)
fesc(Lyα)	(–0.52, 0.13)	(0.20, 0.53)	(0.42, 0.17)	(0.18, 0.57)	(–0.67, 0.02)	(–0.76, 0.00)	(–0.19, 0.56)	(–0.22, 0.53)
Age	(–0.01, 0.99)	(0.60, 0.04)	(0.22, 0.50)	(–0.32, 0.31)	**(0.61, 0.04)**	**(0.84, 0.00)**	**(0.57, 0.05)**	(–0.24, 0.51)
*sSFRuv*_corr	(0.02, 0.96)	(0.65, 0.02)	(–0.38, 0.23)	(0.27, 0.40)	**(–0.56, 0.06)**	**(–0.90, 0.00)**	**(–0.54, 0.07)**	(0.49, 0.15)
M_*	(–0.03, 0.93)	(–0.45, 0.14)	(0.31, 0.33)	(–0.50, 0.10)	**(0.76, 0.00)**	**(0.80, 0.00)**	**(0.56, 0.06)**	(–0.47, 0.17)
$E(B-V)$neb	(0.53, 0.12)	(–0.19, 0.55)	(–0.34, 0.29)	(0.02, 0.95)	(0.52, 0.08)	(0.57, 0.05)	(–0.06, 0.85)	(0.31, 0.38)

Notes. The number pairs in the table correspond to the Spearman coefficient, r, and probability, p, for the correlations between physical (column, y) and morphological (row, x) parameters, measured in the rest-frame UV, optical, and Lyα images. For instance, for $x = G^{SB-rP20S}$ and $y =$ sSFRuv_corr, the Spearman (x, y) calculation tells us that the probability that x and y are uncorrelated datasets is only p = 3% and there is a positive ($r = 0.62$) correlation. Bold face indicates the most significant correlations.

Second of all we quantified the morphological parameters of high-z LARS galaxies. The z2LARS-LAEs tend to be smaller in the rest-frame UV, optical, and Hα than the other LARS galaxies. This is consistent with the observed high-z findings (Gronwall et al. 2011; Bond et al. 2012). Also, the z2LARS-LAEs present a large range of asymmetry values in UV and optical, but do show symmetric morphologies of Lyα emission.

The low surface brightness structures tend to disappear within the background in shallow surveys, making a clumpier and sometimes more elliptical galaxy in the continuum. As a consequence the ellipticity values we measured in the rest-frame UV and optical of z2LARS-LAEs increase as the survey depth decreased. Also, the continuum clumpiness tends to significantly increase. Some of the high-z observations of large ellipticity and clumpy systems could be explained in terms of depth (Gronwall et al. 2011; Bond et al. 2012), but we cannot explain the decrease in the merger fraction and ellipticity for EW(Lyα) $>$ 100 Å LAEs found by Shibuya et al. (2014). However, the clumpiness measured in Lyα also increases for decreasing survey depth (Figs. B.1–B.3), making the integrated EW more difficult to estimate. This happens for the LARS-LAEs as well, which eventually become close to impossible to detect as Lyα emitters. In our sample L08 is the LARS galaxy with the lowest rest-frame optical ellipticity in the original, high-z simulated, and shallow-survey images. It is a massive face-on irregular galaxy in the rest-frame optical, with multiple star-formation clumps seen in the rest-frame UV (Fig. B.2), but it is characterized by the lowest EW(Lyα) among the LARS-LAEs.

Continuum G and M20 values are preserved after pixel resampling and adding noise (see also Appendix A). Therefore, we adopted these two parameters for characterizing LARS galaxies at high redshift (Fig. 13). LARS galaxies have a morphology consistent with merging systems even when simulated at high z. Some z2LARS-LAEs have both rest-frame optical and UV morphologies consistent with being mergers (Fig. 14).

The asymmetry we estimated decreases after adding noise. A merger information calculated just adopting a large-asymmetry criterion could lead to a mis-interpretation of our sample in a shallow survey. This was also noticed in Shibuya et al. (2014), Gronwall et al. (2011) for low signal-to-noise sources.

In general the Lyα morphology tends to be significantly affected in shallow surveys, because Lyα detailed structures are very sensitive to depth and resolution.

6.3. Lyα haloes of LARS galaxies and their implications

There is still open debate about the conditions necessary for the formation of Lyα haloes in high-z galaxies, but it seems that HI scattering is the main factor at the scale of LARS galaxies (Paper II). At high redshift, Lyα halo studies have been performed in stacked data obtained from various samples of galaxies. To be able to compare with high-z results, we simulated how the Lyα haloes of LARS galaxies would appear at $z \sim 2$ and $z \simeq 5.7$. This was performed by stacking subsamples of our galaxies and assuming a range of survey depths. In this test we have the advantage of knowing the original morphology and halo profile.

By simply examining the RGB mosaics in Fig. 1, we see that stacking images with very different irregular structures can be very complicated, but it is commonly done at high redshift to increase the signal-to-noise. Background noise, survey depth, and ground-based PSF are the primary limits of the detection of Lyα haloes. We find that a depth comparable to the M14 survey is ideal to recover these haloes at both $z \sim 2$ and $z \simeq 5.7$ (see Sect. 5.1, Fig. 15). The stacked Lyα surface brightness profile of the LARS-LAEs is peaked in the centre, whereas the

LARSaverage stack contains contributions from more diverse (asymmetric, patchy, and eventually more extended) Lyα morphologies; the result is a more irregular and extended profile. It seems reasonable that the conditions under which a galaxy may emit Lyα (mainly Lyα flux concentrated around the UV-bright knots of star formation), would produce a consistent surface brightness profile. However, variations in the dust and HI contents and distributions, which may cause Lyα photons escape along the line of sight (EW(Lyα) $>$ 0 Å, but not necessarily >20 Å), would produce a more complex, patchy, and extended emission. This is seen in the LARSaverage stack and also in the stack observed in high-z LBGs.

Ground-based observations of high-z galaxies allow us to construct Lyα profiles which extend much farther from the centre (see S11 and M14) than low-z galaxies observed with the HST. The continuum subtraction procedure (Hayes et al. 2009), described in Paper II to isolate Lyα emission, takes advantage of the HST resolution to provide a detailed Lyα mapping within and just outside the interstellar medium. Within the first 10 kpc Lyα scattering already begins to produce halo-like structures in LARS galaxies, while it is at radii above 10−20 kpc that high-z studies are performed because no spatial information is available inside the PSF. A fair comparison between low and high-z observations could only be made by applying the same procedure to extract Lyα from the rest-frame UV emission at high redshift and by investigating the medium on the same scales and the same PSF conditions.

We convolved our HST images with typical ground-based PSFs and compared our smoothed Lyα profile with ground-based observations at comparable scales. Even in this case the $z \sim 2$ LARS Lyα stacked profile is steeper than the one derived for the complete sample by M14 and for the LAE-only subsample of S11. In Feldmeier's survey, the LARS Lyα profile would be indistinguishable from the ground-based PSF on scales larger than 6 kpc. At $z \sim 5.7$, LARS Lyα profile is as steep as the one from M14, which is brighter than the profile they obtained at $z \sim 2$.

With LARS we cannot probe as large scale as the current high-z observations do, due to smaller field-of-view of HST. However, we could still expect some differences between LARS and Feldmeier's sample because of observational depth, and between LARS and the S11 sample because LARS are not located in overdense regions. Also, we may expect differences between LARS and M14 sample at large scale due to the difference in physical properties of the two samples.

The $z \simeq 2.2$ LAE sample studied by Momose et al. is characterized by dust reddening ($E(B-V) < 0.1$), metallicity ($Z \sim 0.2\ Z_\odot$), and stellar mass ($M_* < 10^{10}\ M_\odot$) lower than LARS. Since Lyα photons are sensitive to the presence of dust grains and to the scattering on neutral hydrogen (e.g., Paper II), Lyα morphology (extension and features) is expected to depend on the larger dust and HI contents (Paper III and Rivera-Thorsen et al. 2015). The dust grains, able to absorb Lyα photons close to the knots of star-formation, also prevent their escape at large scales, where HI scattering plays the role of making haloes. There are other phenomena, such as gas kinematics, we are investigating within the LARS survey, which could favour the escape of Lyα photons from the HII regions and ultimately allow the formation of Lyα haloes. Rivera-Thorsen et al. (2015), Duval et al. (in prep.), and Orlitová et al. (in prep.) are dedicated to studying the gas kinematics in LARS galaxies from HST spectroscopy.

7. Conclusions

This paper is the fourth of a series. In this work we have characterized and quantitatively studied the morphology of a sample of starburst galaxies at $z < 0.2$: the Lyman alpha reference sample, LARS.

- LARS galaxies have continuum sizes and stellar masses similar to those of local Lyman break analogues and $2 < z < 3$ star-forming galaxies. The stellar mass and luminosities also match the two samples, respectively. Therefore, LARS galaxies can be studied as a reference of 10^9–$10^{11}\ M_\odot$ high-z star-forming galaxies; they also share some properties with the most massive Lyα emitters at high redshift.
- The rest-frame optical morphology of LARS galaxies is the typical of merging systems. This is also valid for the LAEs within LARS.
- For the first time we were able to quantify the morphology of Lyα emission. LARS-LAEs are on average characterized by more concentrated and symmetrical, while LARS non-LAEs can present patchier and irregular Lyα emissions. LARS-LAEs are more compact in Lyα, even when regridded to high redshift.
- We have simulated LARS galaxies at high redshift and explored their detection: all LARS galaxies would be detected in the continuum in current deep surveys, but they would not be easily detected in the current Lyα surveys at $z \sim 2$.
- In a shallow survey, it is the morphology of Lyα that is most affected by background noise, because the detailed Lyα structures strongly depend on depth and resolution. This may affect high-z Lyα observations.
- The measured ellipticity and clumpiness tend to increase in shallow surveys for most of the LARS galaxies. This could explain some of the high-z observations of large ellipticity and clumpy systems in LAE samples.
- We stacked the Lyα images of LARS galaxies simulated at high redshift. The LARS-LAE stack is peaked in the centre, whereas the LARSaverage stack contains contributions from more diverse Lyα morphologies resulting in a more irregular and extended profile. Variations in the dust and HI contents and distributions may produce more complex, patchy, and extended emission like the one seen in the LARSaverage stack and also in the stack observed in high-z LBGs.
- The Lyα haloes we study in LARS galaxies probe much-smaller-scale media than high-z observations. We find that LARS-halo-profile slope is steeper than $z \sim 2$ and as steep as with $z \simeq 5.7$ observations at ∼10-kpc scales, after applying ground-based PSF.

A sample like LARS, at slightly larger redshift, could allow studying circumgalactic medium-scale haloes and relating them to other galaxy properties. Physical properties (as presented in Paper II), HI-mass estimations (from Paper III), and kinematics (analysed in Rivera-Thorsen et al. 2015; Duval et al., in prep., and Orlitová et al., in prep.) already helped in clarifying the Lyα-photon propagation within the interstellar medium. With the large-scale halo information we would be able to also investigate the mechanisms that transport Lyα photons from the interstellar to the circumgalactic medium.

Acknowledgements. We thank the Referee, Andrew Humphrey, for giving us useful comments which have improved our manuscript. We would also like to thank Nick Bond, Claudia Scarlata, Masami Ouchi and his research group, Suraphong Yuma, Rieko Momose, Takatoshi Shibuya, Yoshiaki Ono, and Caryl Gronwall for useful discussions; Shiyin Shen and Christopher J. Conselice

for key inputs on size and morphological parameter measurements. L.G. sincerely thanks Eric Gawiser and Nelson Padilla for their *always* useful comments and support. G.Ö. and M.H. acknowledge financial support from the Swedish Research 4 Council (VR) and the Swedish National Space Board (SNSB). J.E.G. acknowledges research funding from the Wenner-Gren Foundations. J.M.M.H. has been funded by MINECO grant AYA2012-39362-C02-01. H.O.F. was funded by a post-doctoral UNAM grant and is currently granted by a Cátedra CONACyT para Jóvenes Investigadores. I.O. has been supported by GACR grant 14-20666P of Czech Science Foundation, and long-term institutional grant RVO:67985815. P.L. acknowledges support from the ERC-StG grant EGGS-278202. Dark Cosmology Centre is funded by DNRF. D.K. has been financially supported by the CNES (Centre National d'Études Spatiales)/ CNRS 131425 grant. H.A. was supported by the European Research Council (ERC) advanced grant "Light on the Dark" (LIDA) and the Centre National d'Études Spatiales (CNES).

References

Acquaviva, V., Vargas, C., Gawiser, E., & Guaita, L. 2012, ApJ, 751, L26
Adamo, A., Östlin, G., Bastian, N., et al. 2013, ApJ, 766, 105
Aguirre, P., Baker, A. J., Menanteau, F., Lutz, D., & Tacconi, L. J. 2013, ApJ, 768, 164
Barro, G., Faber, S. M., Pérez-González, P. G., et al. 2013, ApJ, 765, 104
Beckwith, S. V. W., Stiavelli, M., Koekemoer, A. M., et al. 2006, AJ, 132, 1729
Bershady, M. A., Jangren, A., & Conselice, C. J. 2000, AJ, 119, 2645
Bertin, E., & Arnouts, S. 1996, A&AS, 117, 393
Bond, N. A., Gawiser, E., Gronwall, C., et al. 2009, ApJ, 705, 639
Bond, N. A., Feldmeier, J. J., Matković, A., et al. 2010, ApJ, 716, L200
Bond, N. A., Gawiser, E., & Koekemoer, A. M. 2011, ApJ, 729, 48
Bond, N. A., Gawiser, E., Guaita, L., et al. 2012, ApJ, 753, 95
Bond, N. A., Gardner, J. P., de Mello, D. F., et al. 2014, ApJ, submitted [arXiv:1403.7463]
Borne, K. D., Bushouse, H., Lucas, R. A., & Colina, L. 2000, ApJ, 529, L77
Bouwens, R. J., Illingworth, G. D., Blakeslee, J. P., Broadhurst, T. J., & Franx, M. 2004, ApJ, 611, L1
Conselice, C. J. 2003, ApJS, 147, 1
Conselice, C. J., Bershady, M. A., & Jangren, A. 2000, ApJ, 529, 886
Cooke, J., Berrier, J. C., Barton, E. J., Bullock, J. S., & Wolfe, A. M. 2010, MNRAS, 403, 1020
Cowie, L. L., & Hu, E. M. 1998, AJ, 115, 1319
Cowie, L. L., Barger, A. J., & Hu, E. M. 2011, ApJ, 738, 136
Feldmeier, J. J., Hagen, A., Ciardullo, R., et al. 2013, ApJ, 776, 75
Finkelstein, S. L., Cohen, S. H., Windhorst, R. A., et al. 2011a, ApJ, 735, 5
Finkelstein, S. L., Hill, G. J., Gebhardt, K., et al. 2011b, ApJ, 729, 140
Frei, Z., Guhathakurta, P., Gunn, J. E., & Tyson, J. A. 1996, AJ, 111, 174
Grazian, A., Castellano, M., Fontana, A., et al. 2012, A&A, 547, A51
Gronwall, C., Ciardullo, R., Hickey, T., et al. 2007, ApJ, 667, 79
Gronwall, C., Bond, N. A., Ciardullo, R., et al. 2011, ApJ, 743, 9
Guaita, L., Gawiser, E., Padilla, N., et al. 2010, ApJ, 714, 255
Guaita, L., Acquaviva, V., Padilla, N., et al. 2011, ApJ, 733, 114
Hagen, A., Ciardullo, R., Gronwall, C., et al. 2014, ApJ, 786, 59
Hayes, M., Östlin, G., Mas-Hesse, J. M., et al. 2005, A&A, 438, 71
Hayes, M., Östlin, G., Mas-Hesse, J. M., & Kunth, D. 2009, AJ, 138, 911
Hayes, M., Östlin, G., Schaerer, D., et al. 2010, Nature, 464, 562
Hayes, M., Scarlata, C., & Siana, B. 2011, Nature, 476, 304
Hayes, M., Östlin, G., Schaerer, D., et al. 2013, ApJ, 765, L27 (Paper 0)
Hayes, M., Östlin, G., Duval, F., et al. 2014, ApJ, 782, 6 (Paper II)
Holwerda, B. W., Muñoz-Mateos, J.-C., Comerón, S., et al. 2014, ApJ, 781, 12
Hubble, E., & Tolman, R. C. 1935, Contributions from the Mount Wilson Observatory/Carnegie Institution of Washington, 527, 1
Huertas-Company, M., Kaviraj, S., Mei, S., et al. 2014, MNRAS, submitted [arXiv:1406.1175]
Humphrey, A., Villar-Martín, M., Sánchez, S. F., et al. 2008, MNRAS, 390, 1505
Humphrey, A., Binette, L., Villar-Martín, M., Aretxaga, I., & Papaderos, P. 2013a, MNRAS, 428, 563
Humphrey, A., Vernet, J., Villar-Martín, M., et al. 2013b, ApJ, 768, L3
Jiang, L., Egami, E., Mechtley, M., et al. 2013, ApJ, 772, 99
Laursen, P., Razoumov, A. O., & Sommer-Larsen, J. 2009, ApJ, 696, 853
Law, D. R., Steidel, C. C., Shapley, A. E., et al. 2012, ApJ, 745, 85
Lee, J. C., Ly, C., Spitler, L., et al. 2012, PASP, 124, 782
Lee, B., Giavalisco, M., Williams, C. C., et al. 2013, ApJ, 774, 47
Lisker, T. 2008, ApJS, 179, 319
Lotz, J. M., Primack, J., & Madau, P. 2004, AJ, 128, 163
Lotz, J. M., Madau, P., Giavalisco, M., Primack, J., & Ferguson, H. C. 2006, ApJ, 636, 592
Lotz, J. M., Davis, M., Faber, S. M., et al. 2008, ApJ, 672, 177
Lupton, R., Blanton, M. R., Fekete, G., et al. 2004, PASP, 116, 133
Matsuda, Y., Yamada, T., Hayashino, T., et al. 2012, MNRAS, 425, 878
McLinden, E. M., Rhoads, J. E., Malhotra, S., et al. 2014, MNRAS, 439, 446
McLure, R. J., Dunlop, J. S., Bowler, R. A. A., et al. 2013, MNRAS, 432, 2696
Micheva, G., Östlin, G., Bergvall, N., et al. 2013, MNRAS, 431, 102
Momose, R., Ouchi, M., Nakajima, K., et al. 2014, MNRAS, 442, 110
Mosleh, M., Williams, R. J., Franx, M., & Kriek, M. 2011, ApJ, 727, 5
Nakajima, K., Ouchi, M., Shimasaku, K., et al. 2012, ApJ, 745, 12
Nilsson, K. K., Tapken, C., Møller, P., et al. 2009, A&A, 498, 13
Nilsson, K. K., Östlin, G., Møller, P., et al. 2011, A&A, 529, A9
Ono, Y., Ouchi, M., Curtis-Lake, E., et al. 2013, ApJ, 777, 155
Östlin, G., Hayes, M., Kunth, D., et al. 2009, AJ, 138, 923
Östlin, G., Hayes, M., Duval, F., et al. 2014, ApJ, 797, 11 (Paper I)
Ouchi, M., Shimasaku, K., Akiyama, M., et al. 2008, ApJS, 176, 301
Ouchi, M., Shimasaku, K., Furusawa, H., et al. 2010, ApJ, 723, 869
Overzier, R. A., Heckman, T. M., Kauffmann, G., et al. 2008, ApJ, 677, 37
Overzier, R. A., Heckman, T. M., Tremonti, C., et al. 2009, ApJ, 706, 203
Overzier, R. A., Heckman, T. M., Schiminovich, D., et al. 2010, ApJ, 710, 979
Pardy, S. A., Cannon, J. M., Östlin, G., et al. 2014, ApJ, 794, 101 (Paper III)
Partridge, R. B., & Peebles, P. J. E. 1967, ApJ, 147, 868
Pentericci, L., Grazian, A., Scarlata, C., et al. 2010, A&A, 514, A64
Petrosian, V. 1976, ApJ, 209, L1
Petty, S. M., Armus, L., Charmandaris, V., et al. 2014, AJ, 148, 111
Prescott, M. K. M., Martin, C. L., & Dey, A. 2015, ApJ, 799, 62
Rauch, M., Haehnelt, M., Bunker, A., et al. 2008, ApJ, 681, 856
Rhoads, J. E., Malhotra, S., Dey, A., et al. 2000, ApJ, 545, L85
Rivera-Thorsen, T., Hayes, M., Östlin, G., et al. 2015, ApJ, in press [arXiv:1503.01157]
Scarlata, C., Carollo, C. M., Lilly, S., et al. 2007, ApJS, 172, 406
Shen, S., Mo, H. J., White, S. D. M., et al. 2003, MNRAS, 343, 978
Shibuya, T., Ouchi, M., Nakajima, K., et al. 2014, ApJ, 785, 64
Steidel, C. C., Bogosavljević, M., Shapley, A. E., et al. 2011, ApJ, 736, 160
Swinbank, A. M., Smail, I., Chapman, S. C., et al. 2010, MNRAS, 405, 234
Vargas, C. J., Bish, H., Acquaviva, V., et al. 2014, ApJ, 783, 26
Verhamme, A., Dubois, Y., Blaizot, J., et al. 2012, A&A, 546, A111
Yuma, S., Ohta, K., & Yabe, K. 2012, ApJ, 761, 19

Pages 22 to 44 are available in the electronic edition of the journal at http://www.aanda.org

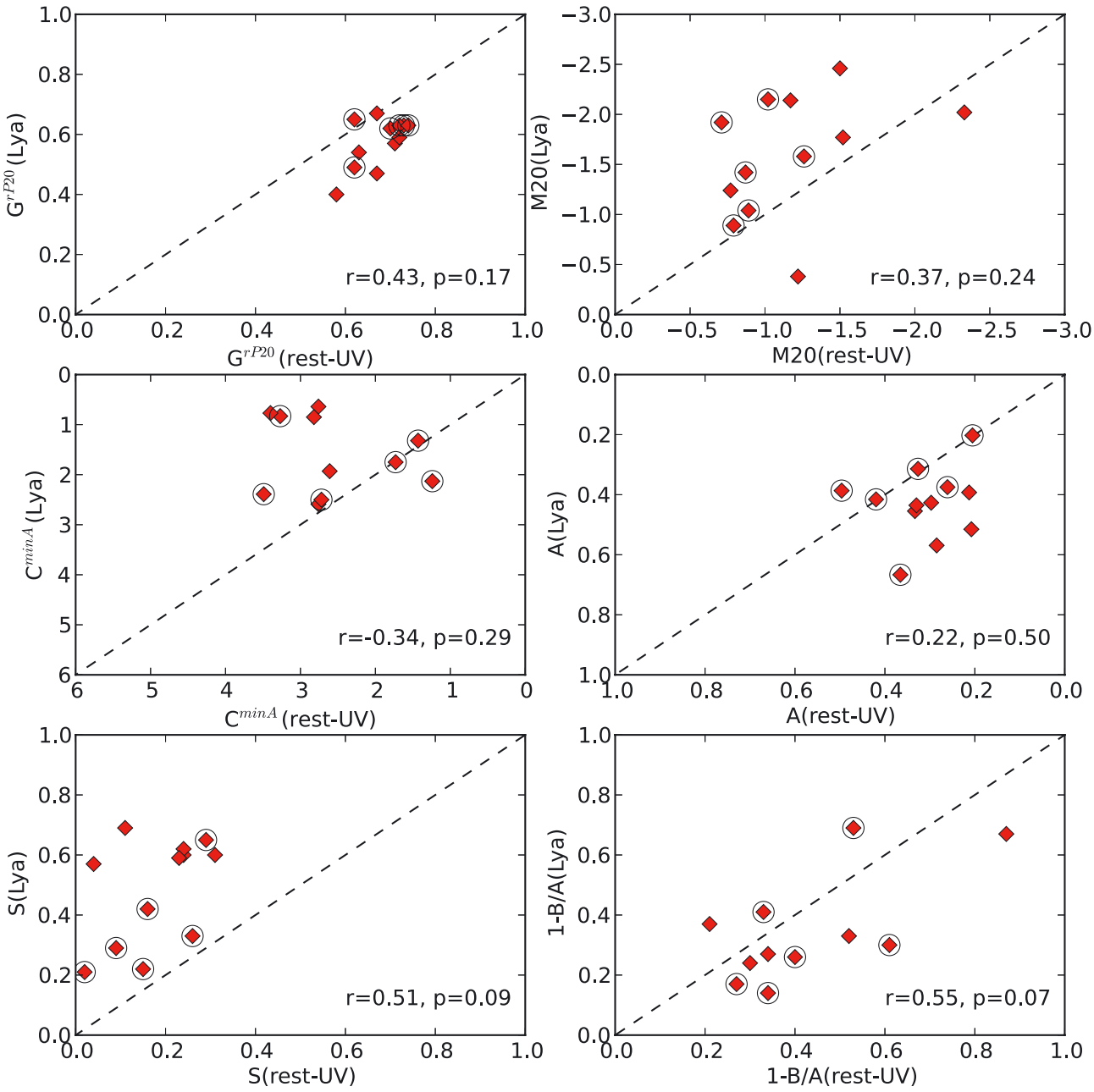

Fig. 5. Non-parametric measurements performed in the Lyα images versus the ones performed in the rest-frame UV. From the *upper left* to the *lower right*: G^{rP20}, M20, C^{minA}, A, S, and SExtractor ellipticity ($1 - B/A$, where A and B are the semi-major and semi-minor axes of the detection ellipse). The dashed line indicates the 1:1 relation. The numbers reported in each panel correspond to the Spearman test coefficient, r, and probability, p, of uncorrelated datasets. $r = 0$ indicates no correlation, $r = 1(-1)$ indicates direct(indirect) proportionality.

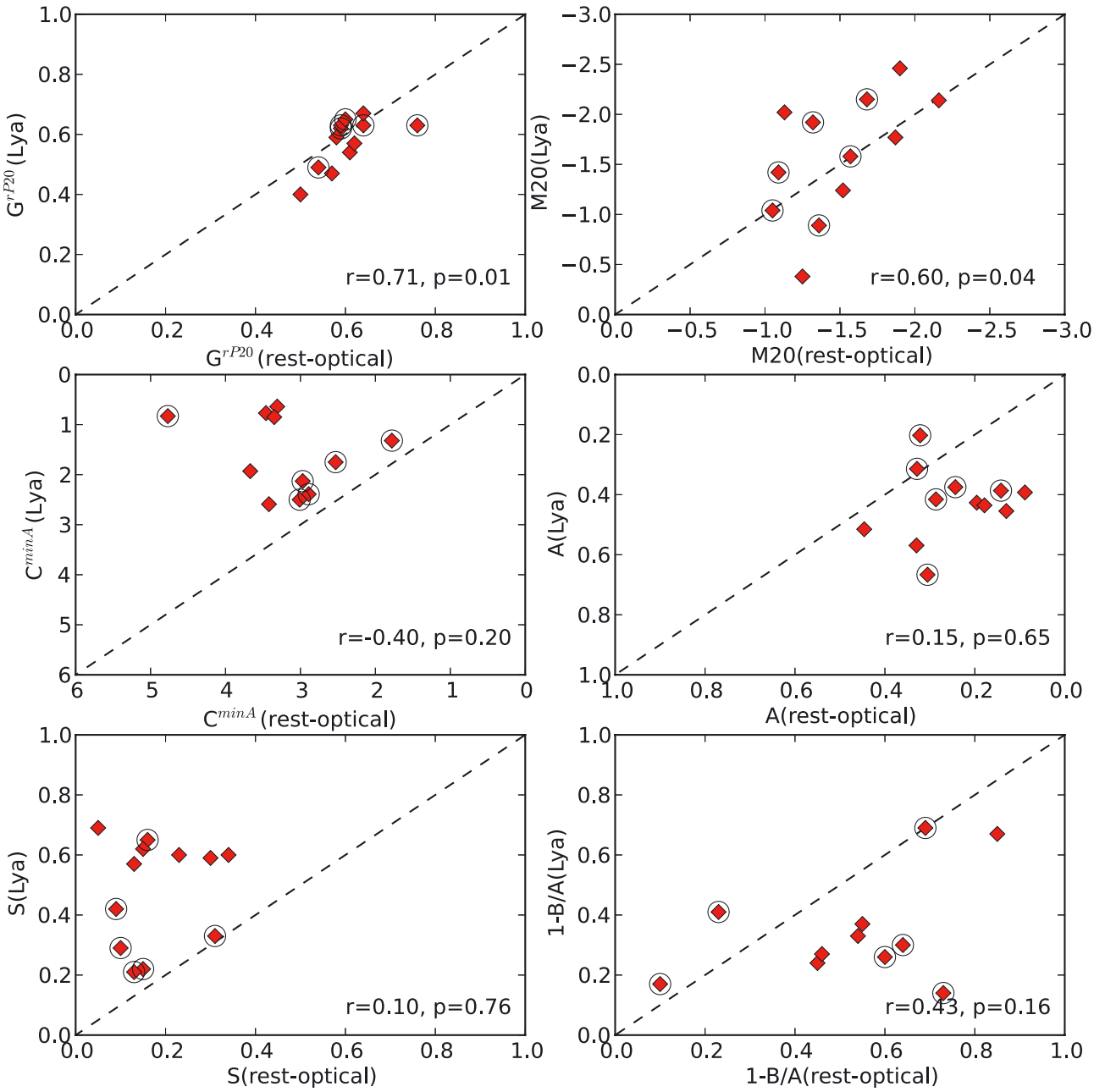

Fig. 6. Non-parametric measurements performed in the Lyα images versus the ones performed in the rest-frame optical. From the *upper left* to the *lower right* we show the same parameters as in Fig. 5.

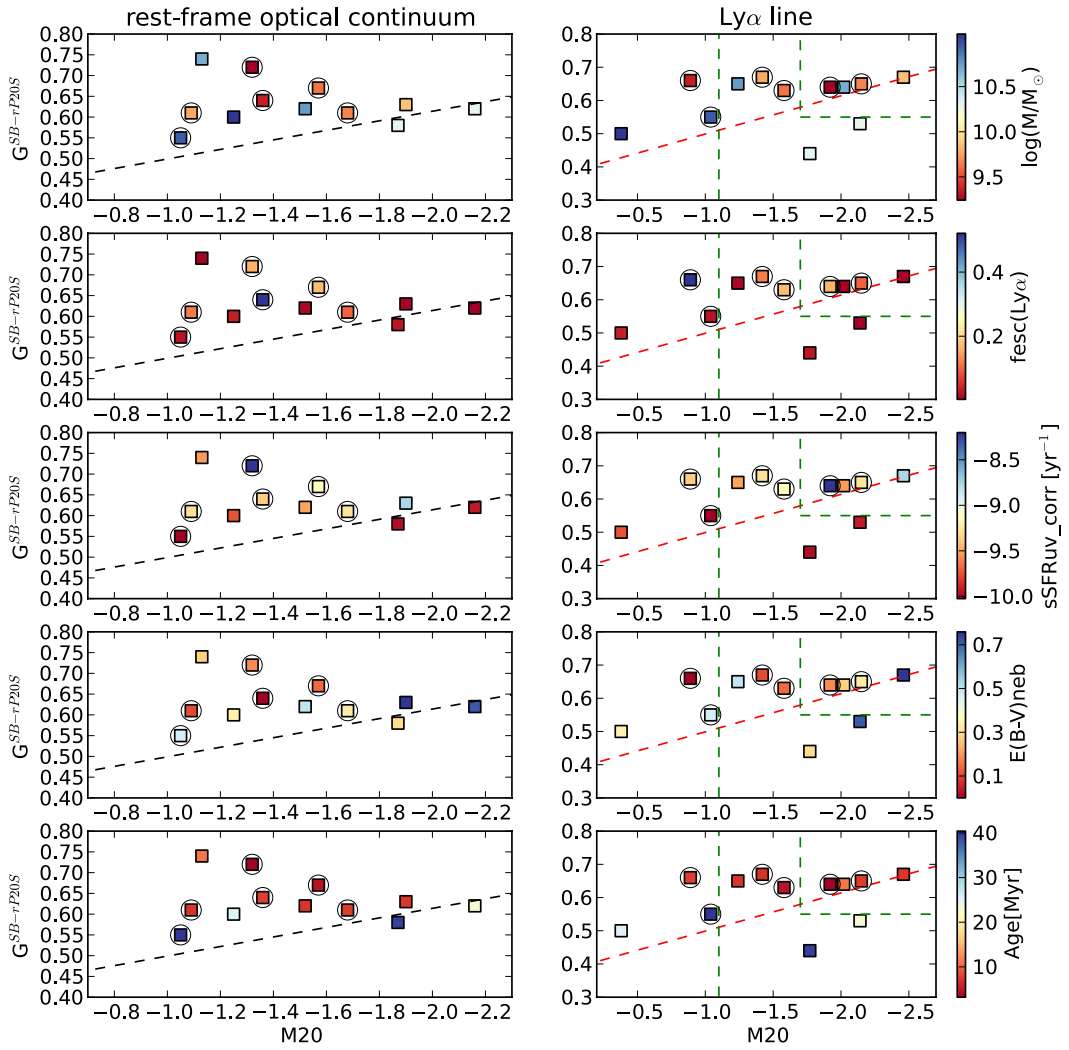

Fig. 18. $G^{SB-rP20S}$ vs. M20 measured in the rest-frame optical (*left panels*) and Lyα (*right panel*) of the original LARS galaxies (squares). LARS-LAEs are indicated with open circles. In each raw the colour scale corresponds to an integrated physical property derived in Paper II (vertical colour bar). *From the top raw* the integrated physical properties are stellar mass, Lyα escape fraction, dust-corrected specific star formation rate, nebular reddening, and age. The dashed lines indicate the regions of separation between merging system, normal galaxies, and bulge-dominated systems as presented in Figs. 13 and 14.

Table 5. Size of high-z simulated LARS galaxies.

Continuum	rP20^{ell}	σrP20^{ell}	rP20^{minA}	σrP20^{minA}	r_{50}	σr_{50}
	kpc	kpc	kpc	kpc	kpc	kpc
line	ξ(rP20^{ell})	$\sigma\xi$(rP20^{ell})	ξ(rP20^{minA})	$\sigma\xi$(rP20^{minA})	$\xi(r_{50})$	$\sigma\xi(r_{50})$
Bond2010($z \sim 3.1$)						
Rest-UV^{F606W}					1.3	
Lyα^{F502N}					~1	
Finkelstein2011($z \sim 4.5$)						
Rest-UV^{F775W}_1					$0.67^{0.07}_{0.07}$	
Lyα^{F658N}_1					$1.1^{3.5}_{0.4}$	
Rest-UV^{F775W}_2					$1.07^{0.27}_{0.20}$	
Lyα^{F658N}_2					$1.3^{1.1}_{0.6}$	
Rest-UV^{F775W}_3					$0.67^{0.07}_{0.00}$	
Lyα^{F658N}_3					$2.0^{1.3}_{0.7}$	
L01						
Rest-UV						
30	2.58	0.20	1.33	0.33	1.17	0.17
29	2.16	0.41	1.32	0.34	1.08	0.19
28	1.83	0.47	1.32	0.50	0.94	0.26
Rest-optical						
29	4.38	0.20	3.18	0.37	2.00	0.17
28	4.51	0.29	3.19	0.46	2.01	0.17
27	4.37	0.49	3.17	0.80	1.98	0.20
26	4.25	0.87	3.35	1.42	1.88	0.28
Lyα						
5E-19	2.20	0.22	2.57	0.37	1.82	0.28
3E-18	2.08	0.28	2.05	0.59	1.73	0.21
8E-18	1.78	0.52	1.74	0.89	1.59	0.39
Hα						
2E-19	0.47	0.04	0.37	0.12	0.53	0.09
6E-19	0.49	0.05	0.34	0.11	0.57	0.09
1E-18	0.48	0.05	0.35	0.12	0.54	0.09
3E-18	0.45	0.06	0.35	0.12	0.51	0.10
L02						
Rest-UV						
30	3.57	1.42	1.86	0.45	2.10	0.91
29	3.53	1.39	2.54	1.43	2.09	0.92
Rest-optical						
29	10.62	0.89	8.82	1.45	4.16	0.25
28	9.76	1.48	6.89	2.02	4.08	0.40
27	7.07	2.30	5.34	2.38	3.48	0.71
Lyα						
5E-19	3.12	0.31	2.43	0.63	2.53	0.16
3E-18	2.63	0.39	1.72	0.68	2.40	0.41
8E-18	1.77	0.80	1.24	0.57	1.71	0.71
Hα						
2E-19	0.16	0.09	0.13	0.05	0.20	0.14
6E-19	0.23	0.03	0.23	0.04	0.33	0.04
1E-18	0.24	0.04	0.23	0.05	0.34	0.05

Notes. Sizes in the continuum are reported as rP20^{ell}. Owing pixel re-sampling, the Petrosian radius can have a variation of 20% with respect to the value estimated in the original image. The Lyα effective radii of two existent individual-source measurements are also shown (Bond et al. 2010; Finkelstein et al. 2011b).

Table 5. continued.

Continuum line	rP20^{ell} kpc ξ(rP20^{ell})	σrP20^{ell} kpc $\sigma\xi$(rP20^{ell})	rP20^{minA} kpc ξ(rP20^{minA})	σrP20^{minA} kpc $\sigma\xi$(rP20^{minA})	r_{50} kpc $\xi(r_{50})$	σr_{50} kpc $\sigma\xi(r_{50})$
L03						
Rest-UV						
30	1.81	0.87	1.38	0.40	0.77	0.31
29	2.15	4.58	1.79	3.65	0.89	1.38
Rest-optical						
29	9.05	2.23	5.82	0.43	3.63	2.00
28	7.95	1.08	4.92	0.83	3.09	0.98
27	7.23	1.71	4.35	0.83	2.98	1.40
26	6.32	1.17	4.06	0.89	2.47	0.30
25	5.47	1.57	4.06	0.89	2.50	0.54
Lyα						
5E-19	7.90	4.45	8.97	11.29	9.19	9.00
3E-18	5.21	11.83	4.00	9.81	8.00	16.92
Hα						
2E-19	0.20	0.02	0.29	0.06	0.18	0.05
6E-19	0.20	0.02	0.29	0.06	0.18	0.05
1E-18	0.21	0.02	0.29	0.06	0.18	0.05
3E-18	0.22	0.02	0.29	0.08	0.21	0.05
L05						
Rest-UV						
30	2.50	0.17	2.33	0.34	1.32	0.17
29	2.54	0.18	2.26	0.40	1.26	0.19
28	2.66	0.22	2.26	0.69	1.33	0.19
27	2.81	0.67	2.46	1.89	1.38	0.22
Rest-optical						
29	2.73	0.20	2.33	0.33	1.27	0.19
28	2.77	0.22	2.35	0.35	1.36	0.18
27	2.87	0.27	2.57	0.61	1.46	0.22
26	3.02	0.41	2.43	1.26	1.52	0.24
Lyα						
5E-19	1.96	0.10	1.76	0.16	1.75	0.13
3E-18	1.93	0.21	1.71	0.33	1.74	0.15
8E-18	1.96	0.37	1.76	0.47	1.86	0.23
Hα						
2E-19	0.92	0.06	1.00	0.20	1.05	0.13
6E-19	0.93	0.07	0.93	0.18	1.13	0.15
1E-18	0.96	0.07	0.98	0.31	1.15	0.14
3E-18	1.03	0.11	1.03	0.26	1.24	0.15
L07						
Rest-UV						
30	1.52	0.18	1.00	0.34	0.67	0.17
29	1.57	0.20	1.05	0.36	0.67	0.17
28	1.57	0.24	1.12	0.39	0.72	0.18
Rest-optical						
29	4.14	0.25	3.34	0.34	1.72	0.19
28	4.02	0.21	3.39	0.38	1.67	0.17
27	4.21	0.36	3.31	0.78	1.73	0.20
26	3.99	0.65	3.00	1.12	1.62	0.27
Lyα						
5E-19	4.54	1.30	3.97	0.39	4.15	2.19
3E-18	3.59	0.59	3.85	0.84	3.22	0.39
8E-18	3.12	0.72	3.45	1.28	3.08	0.58
Hα						
6E-19	0.32	0.04	0.30	0.10	0.48	0.10
wE-19	0.32	0.04	0.30	0.10	0.48	0.10
1E-18	0.32	0.04	0.31	0.10	0.47	0.10
3E-18	0.34	0.08	0.33	0.12	0.48	0.10

Notes. Sizes in Lyα and Hα images are given as ξ(Lyα) = $\frac{\text{size(Ly}\alpha)}{\text{size(rest}-\text{UV)}}$ and ξ (Hα) = $\frac{\text{size(H}\alpha)}{\text{size(rest}-\text{optical)}}$, where the sizes are rP20^{ell}, rP20^{minA}, and r50. ξ(Lyα) is the most meaningful due to the resonant nature of Lyα.

Table 5. continued.

Continuum line	rP20^{ell} kpc ξ(rP20^{ell})	σrP20^{ell} kpc $\sigma\xi$(rP20^{ell})	rP20^{minA} kpc ξ(rP20^{minA})	σrP20^{minA} kpc $\sigma\xi$(rP20^{minA})	r_{50} kpc $\xi(r_{50})$	σ_{r50} kpc $\sigma\xi(r_{50})$
L08						
Rest-UV						
30	7.94	2.62	6.55	1.13	4.40	1.69
29	7.57	2.13	5.92	2.35	3.45	1.08
28	6.67	2.05	5.85	2.75	3.71	0.99
Rest-optical						
29	10.32	1.55	8.67	0.38	4.48	1.40
28	9.86	1.89	8.53	0.54	4.33	1.64
27	9.51	1.97	8.29	0.69	4.06	1.40
26	9.17	1.82	7.67	0.96	3.94	1.28
25	8.17	1.28	7.67	0.96	3.77	0.27
Lyα						
5E-19	2.23	0.16	1.31	0.37	1.58	0.12
3E-18	1.35	0.44	0.73	0.28	1.34	0.39
8E-18	0.76	1.37	0.53	1.59	0.82	1.48
Hα 2E-19	0.67	0.03	0.64	0.08	0.86	0.07
6E-19	0.63	0.03	0.57	0.05	0.80	0.04
1E-18	0.63	0.04	0.56	0.05	0.79	0.04
3E-18	0.95	0.27	0.60	0.11	1.13	0.37
L09						
Rest-UV						
30	20.34	3.32	2.18	1.31	10.34	1.50
29	5.60	2.65	5.67	2.57	3.19	1.84
28	5.09	3.56	1.41	1.03	2.34	2.19
Rest-optical						
29	21.71	0.41	18.01	0.33	12.17	0.17
28	21.81	0.80	18.08	0.49	12.44	0.23
27	15.72	8.35	10.87	5.30	9.00	4.68
Lyα						
5E-19	1.27	0.04	8.24	0.77	1.61	0.04
Hα						
2E-19	0.66	0.19	0.19	0.06	0.50	0.14
6E-19	0.80	0.12	0.17	0.06	0.66	0.09
1E-18	0.73	0.25	0.19	0.08	0.67	0.31
3E-18	0.43	0.19	0.13	0.05	0.37	0.22
1E-17	0.19	0.08	0.10	0.04	0.14	0.06
L10						
Rest-UV						
30	4.68	0.43	3.23	0.41	2.04	0.18
29	4.64	0.66	3.34	0.80	2.10	0.23
28	4.39	1.19	3.45	1.56	2.10	0.37
Rest-optical						
29	9.65	0.36	6.37	0.37	4.08	0.20
28	9.22	0.49	6.16	0.50	3.85	0.20
27	9.09	0.75	5.72	0.86	3.85	0.27
26	8.28	1.23	5.34	1.59	3.76	0.45
Lyα						
5E-19	2.16	1.13	2.59	0.47	3.08	1.55
Hα						
2E-19	0.52	0.07	0.48	0.09	0.54	0.05
6E-19	0.52	0.07	0.48	0.09	0.54	0.05
1E-18	0.50	0.08	0.43	0.12	0.53	0.06
L11						
Rest-UV						
30	28.66	1.20	13.18	0.64	15.17	0.31
29	25.51	2.83	9.64	3.72	13.50	0.72
28	14.59	4.83	6.46	2.49	9.15	2.73
Rest-optical						
29	25.29	6.73	17.64	3.71	12.49	2.77
28	28.06	1.24	17.12	1.17	13.93	0.23
27	24.95	1.90	13.64	2.29	13.67	0.66
26	18.75	3.33	8.51	2.63	11.32	1.53
Lyα						
5E-19	0.25	0.77	0.81	2.04	0.31	1.17

Table 5. continued.

Continuum line	rP20^{ell} kpc ξ(rP20^{ell})	σrP20^{ell} kpc $\sigma\xi$(rP20^{ell})	rP20^{minA} kpc ξ(rP20^{minA})	σrP20^{minA} kpc $\sigma\xi$(rP20^{minA})	r_{50} kpc $\xi(r_{50})$	σr_{50} kpc $\sigma\xi(r_{50})$
3E-18	0.15	0.08	0.24	0.33	0.14	0.12
Hα						
2E-19	1.06	0.11	0.70	0.07	0.92	0.05
6E-19	0.81	0.08	0.56	0.09	0.85	0.10
1E-18	0.90	0.73	0.61	0.20	1.12	0.80
3E-18	0.58	0.10	0.38	0.12	0.66	0.07
L12						
Rest-UV						
30	3.38	0.18	1.67	0.33	1.33	0.17
29	3.44	0.20	1.67	0.34	1.33	0.17
28	3.55	0.25	1.63	0.41	1.32	0.18
27	3.12	0.94	1.70	0.68	1.10	0.35
Rest-optical						
29	4.79	0.21	1.68	1.02	2.05	0.18
28	4.83	0.24	2.25	1.47	2.05	0.19
27	5.09	0.30	2.82	1.59	2.19	0.22
26	5.66	1.53	2.33	1.58	2.66	1.24
Lyα						
5E-19	4.14	0.55	6.87	0.31	5.65	0.87
3E-18	3.81	1.70	6.55	1.07	5.67	2.43
Hα						
2E-19	0.74	0.17	2.04	0.38	0.86	0.41
6E-19	0.71	0.04	1.99	0.20	0.81	0.08
1E-18	0.73	0.04	1.99	0.20	0.82	0.09
3E-18	0.73	0.07	1.84	0.34	0.84	0.09
L13						
Rest-UV						
30	5.29	2.55	1.66	0.34	2.40	2.26
29	4.56	2.08	1.59	0.37	1.80	1.92
28	2.27	0.72	1.54	0.38	0.93	0.22
Rest-optical						
29	12.57	2.48	6.47	0.37	5.94	0.91
28	13.43	0.33	6.35	0.37	6.44	0.20
27	9.31	3.13	6.02	0.43	5.70	1.71
Lyα						
5E-19	0.62	0.14	2.48	3.87	1.11	0.34
3E-18	0.84	0.60	1.74	0.86	1.16	1.03
8E-18	0.96	0.58	1.63	0.75	1.36	0.99
Hα						
2E-19	0.61	0.12	0.31	0.05	0.55	0.14
6E-19	0.63	0.12	0.31	0.05	0.57	0.14
1E-18	0.58	0.13	0.31	0.05	0.48	0.18
3E-18	0.47	0.13	0.28	0.06	0.39	0.13
L14						
Rest-UV						
30	1.67	0.17	1.33	0.33	0.83	0.17
29	1.83	0.18	1.33	0.33	0.84	0.17
28	1.99	1.18	1.19	0.38	1.06	0.99
Rest-optical						
29	4.53	0.18	1.20	0.37	1.50	0.17
28	4.55	0.46	1.10	0.37	1.56	0.41
27	4.88	2.60	1.48	0.59	3.11	2.02
Lyα						
5E-19	3.55	0.33	2.50	0.25	3.00	0.22
3E-18	3.87	0.77	2.49	0.27	3.31	1.17
8E-18	3.50	0.53	2.45	0.29	3.09	0.25
2E-17	3.02	0.51	2.44	0.31	2.87	0.27
5E-17	2.96	0.61	2.44	0.49	2.93	0.38
Hα						
2E-19	0.51	0.04	1.39	0.28	0.79	0.13
6E-19	0.54	0.04	1.39	0.28	0.86	0.12
1E-18	0.56	0.04	1.39	0.28	0.88	0.12
3E-18	1.17	0.60	1.39	0.30	2.34	1.57
1E-17	0.45	0.07	1.22	0.32	0.70	0.12

Table 6. Morphological parameters of high-z simulated LARS galaxies.

Depth	G^{rP20}	σG^{rP20}	$C^{\mathrm{min}A}$	$\sigma C^{\mathrm{min}A}$	M20	σM20	A	σA	S	σS	ell	σell
L01												
Rest-UV												
30	0.73	0.01	2.39	0.00	–1.08	0.03	0.36	0.01	0.20	0.01	0.56	0.02
29	0.70	0.03	2.41	0.12	–1.16	0.34	0.28	0.02	0.18	0.05	0.50	0.06
28	0.67	0.04	2.46	0.45	–1.14	0.41	0.17	0.04	0.20	0.08	0.43	0.09
Rest-optical												
29	0.60	0.00	2.13	0.00	–0.91	0.08	0.26	0.01	0.06	0.01	0.58	0.01
28	0.61	0.01	2.16	0.31	–0.98	0.08	0.18	0.02	0.11	0.01	0.59	0.02
27	0.61	0.02	2.59	0.57	–1.03	0.10	0.10	0.03	0.22	0.04	0.58	0.03
26	0.60	0.03	2.53	0.67	–1.17	0.19	0.04	0.02	0.47	0.12	0.54	0.06
Lyα												
5E-19	0.62	0.02	2.88	0.18	–1.66	0.20	0.28	0.04	0.23	0.06	0.30	0.03
3E-18	0.57	0.01	2.54	0.40	–1.60	0.15	0.15	0.02	0.49	0.09	0.33	0.09
8E-18	0.49	0.02	2.11	0.58	–1.61	0.28	0.09	0.04	0.70	0.15	0.20	0.08
Hα												
2E-19	0.67	0.01	2.39	0.00	–1.10	0.26	0.36	0.00	0.20	0.07	0.43	0.02
6E-19	0.68	0.01	2.39	0.00	–0.87	0.16	0.35	0.01	0.30	0.06	0.46	0.02
1E-18	0.67	0.01	2.39	0.00	–0.94	0.21	0.34	0.01	0.26	0.08	0.44	0.04
3E-18	0.64	0.02	2.40	0.28	–0.97	0.21	0.26	0.02	0.26	0.07	0.42	0.05
L02												
Rest-UV												
30	0.64	0.02	2.40	0.64	–1.41	0.22	0.21	0.03	0.36	0.06	0.69	0.03
29	0.62	0.03	2.29	0.65	–1.29	0.27	0.10	0.04	0.39	0.06	0.71	0.04
Rest-optical												
29	0.62	0.01	3.68	0.19	–1.81	0.08	0.02	0.01	0.36	0.04	0.63	0.02
28	0.60	0.01	3.38	0.32	–1.78	0.12	0.01	0.01	0.54	0.08	0.66	0.03
27	0.55	0.03	2.67	0.59	–1.59	0.19	0.01	0.02	0.60	0.13	0.68	0.05
Lyα												
5E-19	0.61	0.01	3.06	0.35	–1.25	0.07	0.27	0.01	0.35	0.04	0.36	0.03
3E-18	0.51	0.01	2.84	0.43	–1.22	0.21	0.09	0.03	0.64	0.07	0.36	0.12
8E-18	0.45	0.02	2.05	0.52	–1.20	0.25	0.05	0.04	0.68	0.19	0.39	0.12
Hα												
2E-19	0.66	0.02	2.51	0.34	–1.29	0.12	0.34	0.02	0.15	0.07	0.28	0.14
6E-19	0.60	0.02	3.50	0.00	–0.93	0.12	0.26	0.03	0.25	0.07	0.61	0.04
1E-18	0.58	0.02	3.10	0.79	–0.96	0.19	0.21	0.04	0.26	0.07	0.62	0.05
L03												
Rest-UV												
30	0.67	0.03	2.54	0.27	–1.42	0.29	0.08	0.03	0.19	0.12	0.14	0.08
29	0.64	0.15	2.82	1.66	–1.58	1.49	0.06	0.14	0.38	1.02	0.20	0.50
Rest-optical												
29	0.63	0.06	3.38	0.10	–2.01	0.32	0.31	0.03	0.09	0.07	0.46	0.07
28	0.61	0.02	3.07	0.28	–2.00	0.19	0.10	0.03	0.13	0.03	0.46	0.04
27	0.63	0.03	2.98	0.36	–1.96	0.33	0.06	0.01	0.29	0.07	0.34	0.07
26	0.61	0.03	3.06	0.34	–2.04	0.13	0.03	0.01	0.53	0.11	0.27	0.07
25	0.57	0.02	3.06	0.34	–1.87	0.19	0.03	0.01	0.64	0.13	0.37	0.10
Lyα												
5E-19	0.47	0.01	2.70	0.12	–1.78	0.15	0.10	0.02	0.62	0.03	0.30	0.06
3E-18	0.41	0.09	2.04	2.74	–0.93	0.90	0.02	0.10	0.76	0.60	0.50	0.75
Hα												
2E-19	0.67	0.00	3.01	0.00	–1.58	0.25	0.25	0.00	0.08	0.01	0.21	0.03
6E-19	0.66	0.01	3.01	0.00	–1.57	0.25	0.21	0.01	0.10	0.01	0.27	0.03
1E-18	0.67	0.01	3.02	0.05	–1.56	0.27	0.19	0.01	0.11	0.01	0.29	0.03
3E-18	0.65	0.01	2.99	0.33	–1.60	0.26	0.14	0.03	0.17	0.04	0.35	0.05

Notes. Non-parametric measurements are derived by following the equations in Appendix A. Only G^{rP20} and $C^{\mathrm{min}A}$ are reported here, because they are the ones used to compare z2LARS with high-z observations. The uncertainty on the parameters is obtained from the standard deviation of 100 realizations of a simulated survey depth.

Table 6. continued.

Depth	G^{rP20}	σG^{rP20}	$C^{\mathrm{min}A}$	$\sigma C^{\mathrm{min}A}$	M20	σM20	A	σA	S	σS	ell	σell
L05												
Rest-UV												
30	0.70	0.01	3.88	0.07	–1.22	0.07	0.27	0.01	0.23	0.04	0.67	0.01
29	0.70	0.01	3.73	0.21	–1.13	0.10	0.19	0.02	0.35	0.12	0.71	0.02
28	0.70	0.01	3.68	0.48	–1.13	0.12	0.11	0.03	0.32	0.14	0.73	0.03
27	0.68	0.03	2.82	0.78	–1.22	0.25	0.05	0.04	0.36	0.13	0.73	0.05
Rest-optical												
29	0.74	0.01	3.89	0.00	–1.42	0.17	0.27	0.01	0.29	0.05	0.73	0.01
28	0.74	0.01	3.90	0.06	–1.40	0.18	0.19	0.02	0.27	0.07	0.76	0.02
27	0.75	0.02	3.93	0.24	–1.28	0.24	0.12	0.03	0.25	0.11	0.79	0.02
26	0.74	0.03	3.31	1.04	–1.26	0.29	0.06	0.03	0.33	0.17	0.81	0.03
Lyα												
5E-19	0.58	0.01	1.95	0.09	–1.42	0.06	0.26	0.00	0.11	0.01	0.13	0.03
3E-18	0.52	0.02	1.98	0.38	–1.48	0.08	0.13	0.02	0.39	0.08	0.17	0.05
8E-18	0.45	0.01	2.18	0.38	–1.40	0.13	0.05	0.03	0.64	0.11	0.27	0.10
Hα												
2E-19	0.59	0.01	2.21	0.20	–0.79	0.01	0.31	0.01	0.27	0.01	0.44	0.02
6E-19	0.57	0.01	2.25	0.19	–0.76	0.02	0.26	0.03	0.24	0.04	0.52	0.02
1E-18	0.56	0.01	2.21	0.20	–0.76	0.02	0.21	0.04	0.22	0.04	0.56	0.03
3E-18	0.52	0.02	2.24	0.24	–0.75	0.09	0.11	0.04	0.27	0.06	0.64	0.04
L07												
Rest-UV												
30	0.72	0.01	2.39	0.00	–1.20	0.11	0.31	0.01	0.02	0.05	0.47	0.02
29	0.72	0.01	2.39	0.00	–1.12	0.23	0.27	0.01	0.07	0.10	0.50	0.03
28	0.72	0.02	2.43	0.24	–1.02	0.29	0.19	0.04	0.14	0.12	0.51	0.06
Rest-optical												
29	0.63	0.01	3.01	0.03	–1.54	0.12	0.23	0.01	0.05	0.01	0.59	0.03
28	0.62	0.01	3.05	0.13	–1.51	0.12	0.15	0.01	0.08	0.01	0.59	0.02
27	0.63	0.01	2.97	0.38	–1.54	0.13	0.07	0.02	0.20	0.04	0.61	0.02
26	0.63	0.02	2.70	0.65	–1.51	0.18	0.04	0.03	0.46	0.12	0.55	0.09
Lyα												
5E-19	0.64	0.01	3.44	0.10	–2.17	0.21	0.24	0.01	0.18	0.05	0.36	0.04
3E-18	0.57	0.01	3.18	0.27	–2.18	0.12	0.11	0.02	0.49	0.09	0.13	0.07
8E-18	0.51	0.02	2.85	0.48	–2.08	0.16	0.06	0.03	0.66	0.12	0.17	0.08
Hα												
2E-19	0.65	0.01	0.88	0.00	–0.72	0.06	0.34	0.01	0.23	0.05	0.24	0.07
6E-19	0.65	0.01	0.88	0.00	–0.72	0.06	0.34	0.01	0.23	0.05	0.24	0.07
1E-18	0.66	0.01	0.88	0.00	–0.69	0.05	0.33	0.01	0.25	0.04	0.29	0.06
3E-18	0.64	0.02	1.16	0.58	–0.67	0.10	0.25	0.04	0.27	0.09	0.37	0.0
L08												
Rest-UV												
30	0.61	0.04	2.81	0.51	–0.84	0.06	0.10	0.04	0.39	0.09	0.37	0.04
29	0.60	0.03	2.58	0.55	–1.02	0.12	0.05	0.04	0.68	0.12	0.25	0.11
28	0.55	0.03	2.12	0.61	–1.07	0.22	0.01	0.02	0.72	0.13	0.54	0.10
Rest-optical												
29	0.59	0.03	2.71	0.03	–1.21	0.06	0.37	0.00	0.07	0.03	0.20	0.01
28	0.59	0.03	2.69	0.07	–1.24	0.09	0.16	0.02	0.13	0.03	0.16	0.02
27	0.60	0.02	2.63	0.11	–1.25	0.07	0.08	0.01	0.25	0.04	0.16	0.05
26	0.59	0.02	2.50	0.20	–1.26	0.09	0.04	0.01	0.47	0.07	0.17	0.07
25	0.54	0.02	2.50	0.20	–1.17	0.09	0.04	0.01	0.62	0.10	0.24	0.05
Lyα												
5E-19	0.55	0.00	2.77	0.35	–1.75	0.12	0.29	0.03	0.62	0.03	0.15	0.07
3E-18	0.45	0.01	2.06	0.43	–1.33	0.25	0.10	0.04	0.74	0.11	0.37	0.09
8E-18	0.41	0.11	1.81	2.61	–0.75	0.81	0.04	0.27	0.74	0.82	0.54	0.70
Hα 2E-19	0.60	0.01	1.67	0.04	–0.91	0.04	0.36	0.01	0.23	0.02	0.16	0.06
6E-19	0.57	0.01	1.57	0.12	–0.87	0.02	0.33	0.01	0.24	0.01	0.13	0.02
1E-18	0.56	0.01	1.63	0.17	–0.88	0.03	0.28	0.01	0.29	0.03	0.11	0.02
3E-18	0.50	0.01	1.67	0.22	–1.00	0.13	0.11	0.02	0.60	0.13	0.47	0.11

Table 6. continued.

Depth	G^{rP20}	σG^{rP20}	C^{minA}	σC^{minA}	M20	σM20	A	σA	S	σS	ell	σell
L09												
Rest-UV												
30	0.70	0.02	3.59	0.63	–1.23	0.10	0.18	0.05	0.46	0.06	0.79	0.08
29	0.61	0.03	1.54	1.09	–0.90	0.22	0.19	0.08	0.46	0.10	0.57	0.17
28	0.69	0.05	2.46	0.56	–1.74	0.65	0.04	0.03	0.51	0.25	0.38	0.17
Rest-optical												
29	0.67	0.01	2.85	0.05	–0.98	0.01	0.36	0.00	0.33	0.00	0.81	0.00
28	0.65	0.01	2.84	0.12	–0.98	0.01	0.21	0.01	0.36	0.01	0.83	0.00
27	0.62	0.06	2.23	0.71	–1.01	0.26	0.15	0.05	0.50	0.13	0.57	0.22
Lyα												
5E-19	0.47	0.00	0.82	0.10	–0.84	0.01	0.28	0.07	0.57	0.02	0.48	0.02
Hα												
2E-19	0.70	0.02	4.38	0.27	–1.46	0.14	0.23	0.03	0.33	0.12	0.67	0.03
6E-19	0.67	0.01	4.26	0.29	–1.49	0.23	0.19	0.01	0.40	0.04	0.79	0.00
1E-18	0.63	0.03	4.13	0.29	–1.49	0.50	0.16	0.02	0.46	0.09	0.71	0.15
3E-18	0.58	0.03	3.69	0.61	–2.04	0.84	0.11	0.03	0.49	0.16	0.59	0.12
1E-17	0.56	0.04	2.96	0.60	–1.81	0.44	0.06	0.04	0.58	0.20	0.36	0.14
L10												
Rest-UV												
30	0.59	0.02	2.11	0.25	–1.27	0.14	0.14	0.02	0.21	0.04	0.54	0.02
29	0.57	0.03	2.33	0.41	–1.30	0.13	0.07	0.02	0.37	0.09	0.60	0.05
28	0.53	0.04	2.27	0.60	–1.31	0.23	0.02	0.02	0.57	0.15	0.62	0.09
Rest-optical												
29	0.57	0.01	3.34	0.26	–1.97	0.04	0.12	0.00	0.09	0.00	0.55	0.02
28	0.59	0.01	3.35	0.16	–2.04	0.04	0.08	0.01	0.20	0.02	0.50	0.02
27	0.59	0.01	3.18	0.21	–1.98	0.09	0.04	0.01	0.41	0.05	0.52	0.03
26	0.57	0.01	2.95	0.34	–1.92	0.10	0.02	0.01	0.62	0.08	0.53	0.07
Lyα												
5E-19	0.45	0.06	1.08	0.40	–0.82	0.66	0.17	0.13	0.74	0.18	0.41	0.11
Hα												
2E-19	0.58	0.01	2.38	0.70	–1.06	0.14	0.24	0.02	0.30	0.06	0.59	0.03
6E-19	0.58	0.01	2.38	0.70	–1.06	0.14	0.24	0.02	0.30	0.06	0.59	0.03
1E-18	0.55	0.02	2.56	0.68	–1.05	0.15	0.18	0.03	0.35	0.09	0.65	0.03
L11												
Rest-UV												
30	0.57	0.02	3.20	0.10	–1.21	0.08	0.30	0.04	0.39	0.03	0.88	0.08
29	0.56	0.04	2.58	0.53	–1.11	0.18	0.06	0.05	0.47	0.07	0.88	0.09
28	0.57	0.04	2.53	0.74	–0.70	0.18	0.04	0.03	0.69	0.10	0.62	0.15
Rest-optical												
29	0.51	0.01	2.95	0.46	–1.23	0.10	0.28	0.07	0.26	0.13	0.82	0.13
28	0.51	0.02	3.03	0.08	–1.33	0.03	0.18	0.06	0.28	0.01	0.87	0.00
27	0.49	0.02	2.94	0.17	–1.31	0.07	0.05	0.05	0.43	0.05	0.87	0.05
26	0.51	0.02	2.60	0.37	–0.89	0.12	0.01	0.01	0.64	0.07	0.75	0.12
Lyα												
5E-19	0.44	0.34	1.62	1.54	–0.73	1.69	0.43	0.32	0.72	0.87	0.63	0.98
3E-18	0.39	0.05	1.81	0.54	–0.65	0.16	0.29	0.07	0.63	0.25	0.64	0.07
Hα												
2E-19	0.58	0.02	2.61	0.08	–0.89	0.10	0.23	0.01	0.37	0.03	0.88	0.01
6E-19	0.52	0.01	2.39	0.16	–1.11	0.14	0.13	0.02	0.37	0.11	0.81	0.18
1E-18	0.48	0.10	2.58	0.46	–0.67	0.36	0.10	0.12	0.73	0.29	0.44	0.64
3E-18	0.44	0.01	2.28	0.40	–1.01	0.11	0.03	0.02	0.63	0.10	0.73	0.13

Table 6. continued.

Depth	G^{rP20}	σG^{rP20}	$C^{\mathrm{min}A}$	σC^{minA}	M20	σM20	A	σA	S	σS	ell	σell
L12												
Rest-UV												
30	0.69	0.00	3.33	0.23	–1.43	0.03	0.37	0.01	0.10	0.02	0.38	0.01
29	0.69	0.01	3.32	0.24	–1.44	0.04	0.25	0.03	0.11	0.01	0.41	0.01
28	0.70	0.01	3.29	0.30	–1.47	0.22	0.16	0.04	0.18	0.03	0.45	0.02
27	0.69	0.03	3.11	0.53	–1.84	0.41	0.11	0.04	0.39	0.19	0.27	0.17
Rest-optical												
29	0.65	0.01	3.09	0.22	–1.71	0.15	0.37	0.07	0.15	0.01	0.49	0.01
28	0.65	0.01	3.20	0.30	–1.65	0.10	0.25	0.01	0.15	0.01	0.52	0.01
27	0.66	0.01	3.35	0.39	–1.80	0.18	0.14	0.01	0.20	0.01	0.54	0.01
26	0.68	0.05	3.21	0.60	–1.54	0.48	0.07	0.04	0.41	0.12	0.54	0.09
Lyα												
5E-19	0.62	0.01	1.27	0.11	–2.26	0.25	0.37	0.03	0.44	0.10	0.27	0.03
3E-18	0.54	0.06	1.38	0.30	–1.81	0.87	0.13	0.07	0.75	0.15	0.47	0.13
Hα												
2E-19	0.61	0.05	2.99	0.11	–1.54	0.22	0.34	0.05	0.19	0.14	0.39	0.06
6E-19	0.62	0.01	3.01	0.00	–1.66	0.16	0.28	0.00	0.19	0.06	0.40	0.02
1E-18	0.62	0.01	3.01	0.00	–1.83	0.20	0.26	0.01	0.17	0.05	0.41	0.02
3E-18	0.60	0.01	2.93	0.29	–1.60	0.30	0.17	0.01	0.23	0.03	0.44	0.03
L13												
Rest-UV												
30	0.72	0.03	1.60	0.36	–1.24	0.34	0.27	0.01	0.17	0.12	0.37	0.11
29	0.71	0.03	2.30	0.73	–1.35	0.24	0.23	0.03	0.23	0.13	0.38	0.08
28	0.65	0.03	2.36	0.65	–1.37	0.19	0.18	0.03	0.20	0.12	0.15	0.08
Rest-optical												
29	0.64	0.02	3.64	0.03	–1.32	0.22	0.31	0.00	0.24	0.15	0.47	0.06
28	0.62	0.01	3.52	0.08	–1.45	0.06	0.21	0.01	0.23	0.01	0.53	0.02
27	0.49	0.05	3.31	0.11	–0.98	0.16	0.16	0.01	0.49	0.15	0.53	0.11
Lyα												
5E-19	0.53	0.03	2.10	1.28	–0.52	0.12	0.40	0.07	0.61	0.09	0.40	0.12
3E-18	0.48	0.02	1.74	0.50	–1.18	0.32	0.28	0.07	0.55	0.09	0.24	0.10
8E-18	0.44	0.02	1.63	0.56	–1.22	0.25	0.12	0.06	0.72	0.13	0.40	0.11
Hα												
2E-19	0.67	0.01	1.99	0.00	–1.90	0.09	0.16	0.00	0.17	0.03	0.23	0.07
6E-19	0.66	0.01	1.99	0.00	–1.87	0.10	0.16	0.01	0.24	0.03	0.25	0.07
1E-18	0.65	0.02	1.99	0.00	–1.93	0.43	0.14	0.01	0.30	0.11	0.28	0.17
3E-18	0.60	0.02	1.80	0.30	–1.91	0.32	0.09	0.02	0.44	0.15	0.34	0.16
L14												
Rest-UV												
30	0.64	0.00	2.39	0.00	–0.99	0.04	0.36	0.00	0.04	0.02	0.41	0.02
29	0.64	0.01	2.39	0.00	–0.77	0.11	0.32	0.01	0.11	0.07	0.52	0.03
28	0.65	0.05	2.38	0.09	–0.94	0.20	0.29	0.05	0.08	0.10	0.47	0.15
Rest-optical												
29	0.78	0.00	2.39	0.00	–1.06	0.09	0.39	0.00	0.19	0.01	0.09	0.02
28	0.78	0.01	2.39	0.00	–1.17	0.12	0.29	0.02	0.27	0.04	0.22	0.05
27	0.67	0.13	1.97	0.51	–0.93	0.34	0.28	0.11	0.36	0.18	0.50	0.12
Lyα												
5E-19	0.61	0.03	2.13	0.00	–1.47	0.07	0.29	0.00	0.16	0.01	0.17	0.01
3E-18	0.61	0.02	2.13	0.01	–1.51	0.09	0.24	0.01	0.20	0.03	0.24	0.04
8E-18	0.56	0.03	2.12	0.04	–1.48	0.09	0.19	0.01	0.28	0.07	0.21	0.04
2E-17	0.50	0.02	2.04	0.16	–1.44	0.09	0.12	0.02	0.40	0.11	0.15	0.05
5E-17	0.43	0.02	1.99	0.23	–1.33	0.12	0.05	0.03	0.60	0.11	0.23	0.09
Hα												
2E-19	0.55	0.01	1.50	0.00	–1.07	0.03	0.20	0.00	0.03	0.01	0.39	0.01
6E-19	0.57	0.01	1.50	0.00	–1.08	0.01	0.21	0.00	0.03	0.00	0.42	0.01
1E-18	0.58	0.01	1.50	0.00	–1.09	0.01	0.18	0.00	0.04	0.00	0.45	0.02
3E-18	0.65	0.07	1.63	0.21	–0.91	0.30	0.19	0.09	0.23	0.18	0.43	0.13
1E-17	0.52	0.03	1.48	0.12	–1.35	0.12	0.10	0.02	0.14	0.07	0.19	0.08

Appendix A: Non-parametric measurements

In this section we explain the way we measured galaxy sizes and non-parametric quantities in detail, and show the results for galaxies with known-profiles.

In Fig. A.1 we summarize the equations adopted in this analysis and first introduced by Conselice et al. (2000) and Lotz et al. (2004).

The code we developed makes a basic use of the ELLIPSE task in *iraf.stsdas.isophote* and the PHOT task in *iraf.digiphot.apphot*. We first ran the Source Extractor (SExtractor) software (Bertin & Arnouts 1996) on one galaxy image. This provided the centroid and the elliptical aperture containing the entire galaxy. We adopted configuration parameters like in Bond et al. (2009; DETECT_THRESH = 1.65 and DEBLEND_MINCONT = 1). We followed the choice of DETECT_MINAREA = 30 for the high-z simulations. Those parameters were optimized to provide significant morphological measurements in deep HST-band observations. A larger value of contiguous pixels was adopted to prevent SExtractor from breaking up the clumpy, resolved, original $z \sim 0$ LARS galaxies into smaller fragments.

We adopted SExtractor centroid, orientation angle, and ellipticity as the fixed ELLIPSE parameters and the SEx AUTO photometry semi-major axis as the reference semi-major axis length (sma0). We then measured flux within ellipses by varying the semi-major axis (sma). The task was able to fit elliptical isophotes at a pre-defined, fixed sma, and works better for well-defined galaxy profiles. As LARS galaxies are irregular, a better convergence of the task was performed by fixing the ellipse orientation and ellipticity.

The ELLIPSE task outputs surface brightness ($I(r)$) and integrated flux (F) within every sma (r_i, r_{i+1}, ...). We used the given surface brightness to derive the Petrosian ratio (Bershady et al. 2000, $\eta = I(r)/\langle I(r)\rangle$) as a function of sma and the integrated flux to estimate r_{20}, r_{50}, r_{80}, the radii containing 20%, 50%, and 80% of the total source flux. The Petrosian semi-major axis (rP20$^{\rm ell}$) corresponds to the sma where $\eta = 0.2$. We defined an elliptical concentration ($C^{\rm ell}$), proportional to r_{80}/r_{20}. Applying a smoothing kernel with width equal to rP20/5, we also estimated a smoothed-image Petrosian radius (rP20S, Lotz et al. 2004).

The PHOT task outputs fluxes integrated within circular apertures. We derived the corresponding $I(r)$ and estimated the circular Petrosian radius (rP20$^{\rm circ}$), the circular $r_{20}^{\rm circ}$, and $r_{80}^{\rm circ}$. The circular concentration ($C^{\rm circ}$) was then proportional to $r_{80}^{\rm circ}/r_{20}^{\rm circ}$.

We also defined the signal-to-noise (SN) per pixel as

$$SN_{\rm pixel} = \frac{1}{n}\Sigma_{i=1}^{n}\frac{S_i}{\sqrt{\sigma_{\rm sky}^2 + |S_i|}},$$

where $\sigma_{\rm sky}$ is the standard deviation of means measured in more than three boxes around the galaxy, S_i the signal, and n the number of pixels belonging to a galaxy. The total SN of the galaxy was then obtained by multiplying the SN$_{\rm pixel}$ by $\sqrt{n}$. If $\sigma_{\rm sky}^2 > |S_i|$,

$$SN_{\rm pixel} = \frac{1}{n}\Sigma_{i=1}^{n}\frac{S_i}{\sigma_{\rm sky}}.$$

The asymmetry (A) was calculated as the minimum value of the normalized difference between the galaxy image (I_0) and the same one rotated by 180° (I_{180}). We adopted the background (B) correction advised by Conselice et al. (2000) for low SN galaxies. Based on this definition, $0 < A < 1$ (e.g., Scarlata et al. 2007; Aguirre et al. 2013; Law et al. 2012). After calculating the position of minimum asymmetry, we ran PHOT on that position and calculated the Petrosian radius (rP20$^{{\rm min}A}$), $r_{20}^{{\rm min}A}$, and $r_{80}^{{\rm min}A}$, corresponding to the minimum of asymmetry. The point of the galaxy of minimum asymmetry is generally close to its brightest pixel, but not necessarily to the SExtractor centroid. The concentration ($C^{{\rm min}A}$) at minimum asymmetry was then calculated from the $r_{80}^{{\rm min}A}/r_{20}^{{\rm min}A}$ ratio (Conselice et al. 2000; Lotz et al. 2006; Jiang et al. 2013; Holwerda et al. 2014).

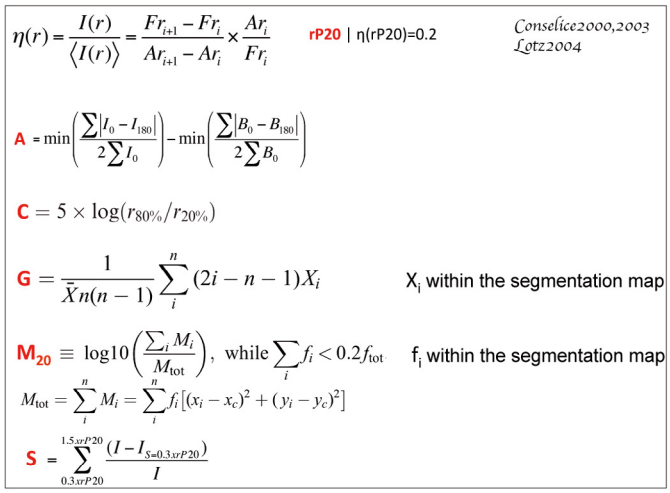

Fig. A.1. Basic equations adopted to calculate galaxy size and non-parametric measurements of the LARS original and high-z simulated galaxies.

Bershady et al. (2000) defined C by measuring photometry inside circular apertures. They estimated that C could be underestimated up to 30%, in the case of an ellipticity of ~0.75 and circular aperture, but that it was within 10−15% for early-type galaxies. $C^{{\rm min}A}$ was the quantity we mainly used throughout the paper.

A galaxy was assumed to be composed of a certain number of pixels, constituting a segmentation map. The non-parametric measurements and SN estimation were performed counting the flux of pixels belonging to that segmentation map. We defined the segmentation map in two ways, one (the fixed-size segmentation map) is an ellipse with sma = rP20 and orientation given by SEx (see Scarlata et al. 2007); one described in Lotz et al. (2004), where the pixels belonging to the segmentation map have surface brightness larger than the value at rP20S. The fixed-size map was mainly concentrated in the central part of the galaxy, the second one could contain bright pixels in the galaxy outskirts.

The Gini coefficient (G) and M20 were also calculated by following the equations in Fig. A.1. X_i ($i = 1$ to n) correspond to the pixel values, sorted in increasing order, and $\bar{X}$ the average pixel value, within the chosen segmentation map. f_i ($i = 1$ to n) correspond to the pixel values within the chosen segmentation map, but sorted in decreasing order; x_c and y_c are the pixels corresponding to SEx centroid. A first value of G (G^{rP20}) was estimated within the first segmentation map (Lotz et al. 2004, 2006; Jiang et al. 2013; Holwerda et al. 2014). A second value ($G^{SB-rP20S}$) was estimated within the second segmentation map. The latter is sensitive to multiple knots in a galaxy full of structures. Within the fixed-sized segmentation map we measured M20 (Scarlata et al. 2007; Jiang et al. 2013; Aguirre et al. 2013; Holwerda et al. 2014) and S.

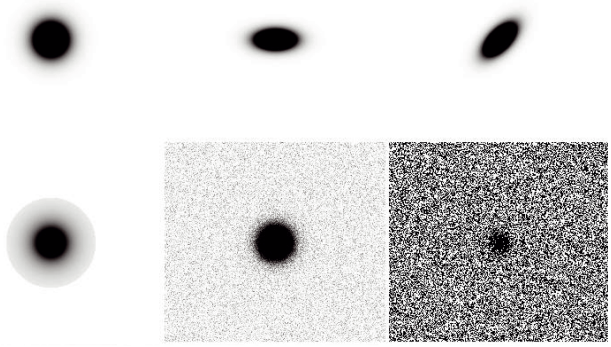

Fig. A.2. Simulated profiles used as a test of our code performance. From the *upper left* to the *lower right panels*: symmetric exponential profile, exponential profile with ellipticity equal to 0.5 and position angle 0°, exponential profile with ellipticity equal to 0.5 and position angle 45°, de Vaucouleurs profile, asymmetric exponential profile after adding a noise corresponding to a 10σ detection limit 7 times fainter (noise in Tables A.1 and A.2) and 3 times fainter than the fake galaxy flux. They were generated by running the MKOBJECT task in *iraf.artdata* and noise was added by running the MKNOISE task in *iraf.artdata*.

The clumpiness (S) was defined by Conselice (2003) as the normalized difference between the galaxy image (I) and the smoothed image ($I_{0.3xrP20}$, where the smoothing kernel sigma was 0.3× rP20). The pixels belonging to the galaxy image are the ones within 0.3 and 1.5 times the rP20, i.e. we excluded the very central pixels, which are often unresolved.

We tested our code on the frames showed in Fig. A.2. The code calculations are shown in Fig. A.3. First of all we analytically calculated the theoretical (THEO in the figure) Petrosian ratio and radius of an exponential and de Vaucouleurs profiles. Then, we ran SExtractor and calculated the non-parametric measurements described above.

The results are listed in Tables A.1 and A.2. The rP20$^{\rm ell}$ size better recovers the analytical value of an exponential profile. It also well recovers the value in the case of added noise and of a de Vaucouleurs profile. For this reason, we adopted rP20$^{\rm ell}$ as the main size estimator throughout the paper. By comparing with the analytical solution and the estimations by Bershady et al. (2000) and Lotz et al. (2006), we noticed that we could underestimate $C^{\rm circ}$ of a de Vaucouleurs profile up to 30%, $C^{{\rm min}A}$ of an exponential(de Vaucouleurs) profile up to 10(20)%, and overestimate $G^{SB-rP20S}$ up to 10(5)% for an exponential(de Vaucouleurs) profile. M20 is well-recovered for all the profiles within 3%.

Also, we tested our code on the public galaxy stamps from COSMOS and compared the results with the ones obtained with the ZEST software (Scarlata et al. 2007). When assuming the brightest pixel as the centre of a galaxy, we recovered G^{rP20} values in more than 80% of the cases. As the fixed-size segmentation map is a better choice for redshift comparisons (Scarlata et al. 2007), we tended to prefer G^{rP20} rather than $G^{SB-rP20S}$ throughout the paper.

A.1. Comparison between original and simulated galaxy morphological parameters

Following the method described in the previous section, we estimated sizes and morphological parameters in the continuum and line images. We adopted the same method in the case a galaxy was simulated to be at $z \sim 2$ and observed in different depth surveys. To quantify the morphological parameter variations owing pixel resampling and added noise, we defined Δ(param),

$$\Delta(\text{param}) = \frac{\text{param}(z \sim 2, \text{noise}) - \text{param}(\text{original})}{\text{param}(\text{original})} \quad \text{(A.1)}$$

which represented the difference between the measurement of a parameter in the simulated and in the original image, normalized to the value in the original image. By definition, Δ(param) tended to be zero when the two measurements were very similar, tended to be equal to −1 when the measurement in the simulated image was much smaller than in the original one, and equal to 1 when the measurement in the simulated image was twice that in the original one. We calculated Δ(param) for every galaxy and estimated the mean and the standard deviation.

In Fig. A.4 we show the results. A, $C^{{\rm min}A}$, G^{rP20}, and M20 were all preserved after pixel resampling in the continuum images. Owing survey depth, A decreased.

Huertas-Company et al. (2014) studied the variation of A, G, and M20 due to resampling the rest-frame optical of local galaxies to $z > 1$. They found that A can increase up to 50%, G up to 10%, while M20 can decrease up to 10%. These trends were observed to be more pronounced for early-type galaxies; Lotz et al. (2006) resampled the rest-frame UV of a few sources from $z = 1.5$ to $z = 4$, finding that G and M20 were preserved, consistent with our results. Overzier et al. (2010) investigated the change of A, C, G, and M20 when resampling $z = 0.2$ Lyman break analogues to $z = 2$. They gave an R-value scale, where $|R| \sim 0$ when the difference between the median parameter measured in the resampled and in the original image was small and $|R| \sim 1$ when was comparable to the sample scatter. They found $R^A = -1.1$, $R^C = 0.02$, $R^G = -0.34$, and $R^{M20} = -0.43$ in the rest-frame UV and $R^A = -0.46$, $R^C = -0.52$, $R^G = -1.1$, and $R^{M20} = -0.26$ in the rest-frame optical. Recently, Petty et al. (2014) explored the variations of G and M20 of local LIRGS when simulated to be at $z = 0.5$, 1.5, 2, 3 and in a survey with the HUDF depth. Some of the galaxies in their sample, characterized by clumps and filamentary structures (typical of merging systems) in high-resolution HST images, tended to appear as disk-like galaxies by $z = 2$. Some others maintained merging systems' morphology. All these trends are in agreement with our findings, but they also tell us that the variations do not follow a specific trend for irregular galaxies.

In the Lyα images, A tended to decrease and $C^{{\rm min}A}$ could increase due to pixel resampling. Owing survey depth, all the four parameters tended to decrease and A significantly decreased.

Another way to study the change of morphological parameters is to look at pairs of them, like G^{rP20} vs. M20 and A

Table A.1. Sizes from known profile galaxies of Re = 10 pixels.

Profile kpc	rP20$^{\rm ell}$ kpc	rP20$^{\rm circ}$ kpc	rP20$^{{\rm min}A}$ kpc	r_{20} kpc	r_{50} kpc	r_{80} kpc
exp						
ell0	22.0	21.0	19.0	5.5	10.0	17.5
ell0.5,pa0	21.5	16.0	15.0	5.0	10.0	17.5
ell0.5,pa45	21.5	16.0	15.0	5.0	10.0	17.0
noise	19.0^{+5}_{-1}	16.0^{+7}_{-2}	23.0	5.0	10.0	16.0
deVauc						
	20.5	17.0	11.0	2.5	7.5	17.0

Notes. The analytical values for the ratio of rP20 and effective radius is 2.16 for an exponential and 1.82 for a de Vaucouleurs profile (Bershady et al. 2000).

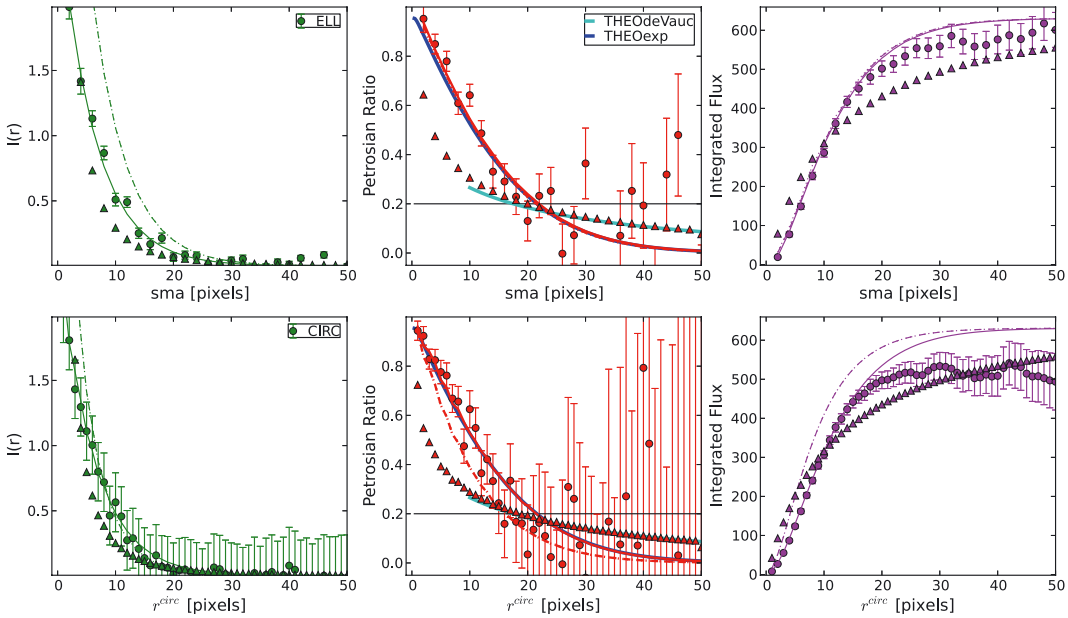

Fig. A.3. *From the left to the right panels* surface brightness, Petrosian ratio, and integrated flux. The *upper(lower)* row is obtained by using elliptical(circular) aperture and the *iraf* ELLIPSE(PHOT) task. For an effective radius, Re = 10 pixels, we estimated photometry in the case of a symmetric exponential profile (solid line), exponential profile with ellipticity equal to 0.5 and either position angle 0 (dashed line) or 45 (dotted line) degrees, and of a de Vaucouleurs profile (triangles). The case of adding noise is represented by filled circles with and without errorbars. The analytical Petrosian ratios for exponential (THEOexp) and de Vaucouleurs (THEOdeVauc) profiles are presented in the *second-column panels* as blue and cyan solid curves respectively.

Table A.2. Morphology measurements from known profile galaxies of Re = 10 pixels.

Profile	G^{rP20}	$G^{SB-rP20S}$	M20	ell	$C^{\rm circ}$	$C^{\rm ell}$	$C^{\rm minA}$	A	S
exp									
ell0	0.4888	0.5229	–1.752	0.05	2.657	2.513	2.386	0.0	0.016
ell0.5,pa0	0.4923	0.5326	–1.836	0.5	2.559	2.720	2.559	0.0	0.036
ell0.5,pa45	0.4874	0.5333	–1.796	0.5	2.559	2.657	2.559	0.0	0.034
noise	0.4914	0.5164	–1.164	0.114	2.236	2.526	2.236	–0.0135	0.393
deVauc									
	0.6183	0.6271	–2.398	0.05	3.495	4.162	3.495	0.0	0.025

Notes. The analytical values of $C^{\rm circ}$ is 2.7 and 5.2 for an exponential and a de Vaucouleurs profile respectively (Bershady et al. 2000). Lotz et al. (2006) estimated $G^{SB-rP20S}$=0.473, M20 = −1.8, $C^{\rm minA}$ = 2.71 for a noise-free image of an exponential profile and $G^{SB-rP20S}$ = 0.6, $M20$ = −2.47, $C^{\rm minA}$ = 4.34 for a noise-free image of a de Vaucouleurs profile (half-light-radius equal to 600 resolution elements).

vs. $C^{\rm minA}$. In Fig. A.5 we show the diagrams of two-parameters, measured in the rest-frame optical, UV, and Lyα images. Our analysis showed that the G and M20 estimations were not affected by resolution and survey depth. Therefore, they were useful for comparisons at different redshifts and different survey depths throughout the paper.

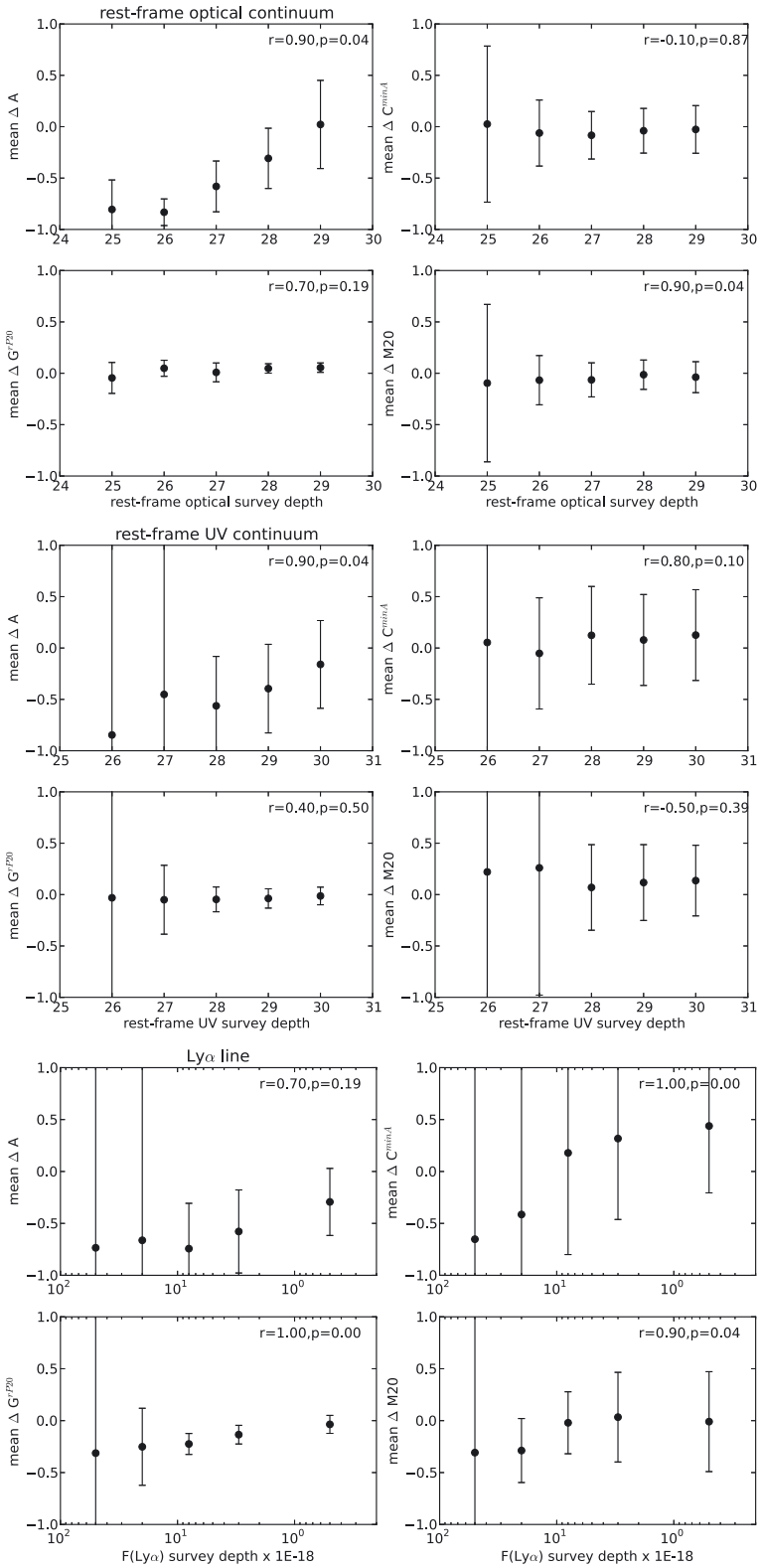

Fig. A.4. Mean Δ(param) as defined in Eq. (A.1) vs. simulated survey depth. *param* is *A* (*upper left*), C^{minA} (*upper right*), G^{rP20} (*lower left*), and M20 (*lower right*) for the rest-frame optical, UV, and Lyα simulated images. The deepest simulated survey is represented by the most right data point in each panel. The error bars represent the standard deviation among all the high-z simulated LARS galaxies. In the case fewer-than-twelve galaxies are detected at a specific depth, the error bars is increased proportionally to the number of undetected galaxies. The numbers on the top right corner of each panel represent the Spearman test coefficient, r, and probability, p, of uncorrelated datasets, assuming that the depth vector indicates the deepest survey on the right of the x-axis.

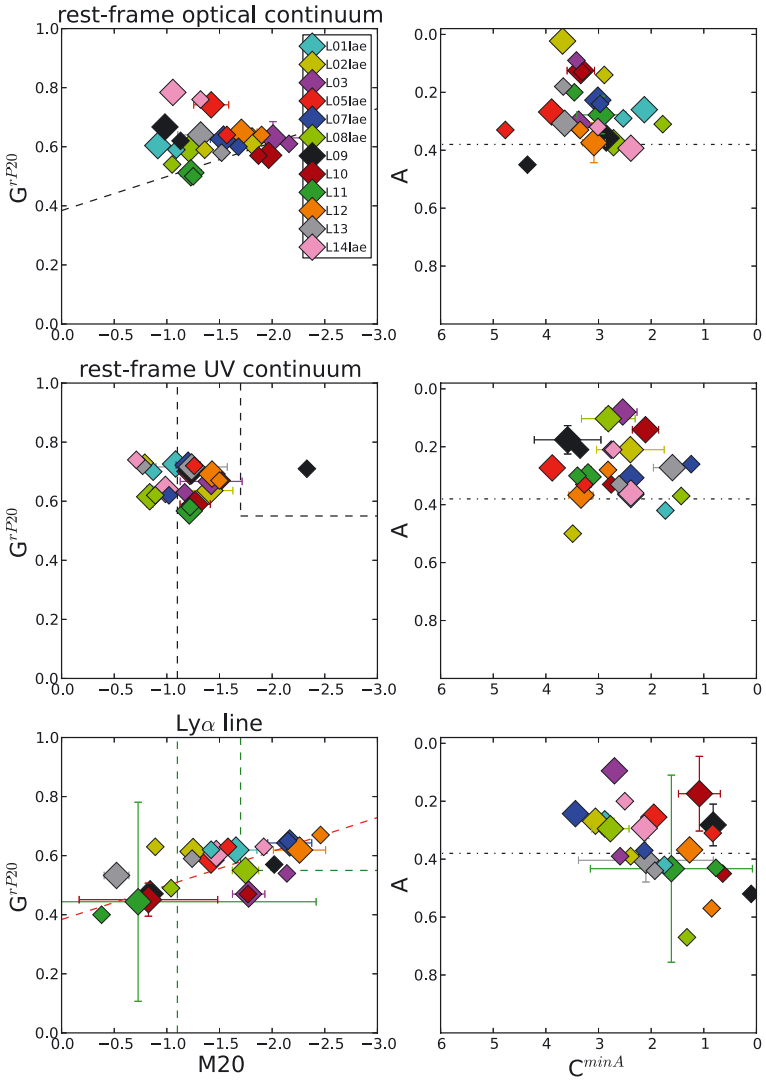

Fig. A.5. G^{rP20} vs. M20 (*first column*) and A vs. $C^{\mathrm{min}A}$ (*second column*) measured in the rest-frame optical (*upper*), UV (*middle*), and Lyα (*lower*) images. Small and big diamonds with error bars indicate the parameters of the original and (deepest survey) high-z simulated LARS galaxies. The dashed and dotted-dashed lines indicate the separation between merging system and normal galaxies' parameter space. Owing pixel resampling the galaxies stay in the same region of the G^{rP20} vs. M20 diagram.

Appendix B: LARS galaxies simulated at high redshift in a deep and shallow survey

In this appendix, we show the continuum and line maps of the high-z simulated LARS galaxies. Figures B.1–B.3 present rest-frame UV, Lyα, rest-frame optical, and Hα images in the deepest survey depth probed here, together with SEx detection apertures. In Figs. B.4–B.6, we show the same stamps but for a shallower simulated survey.

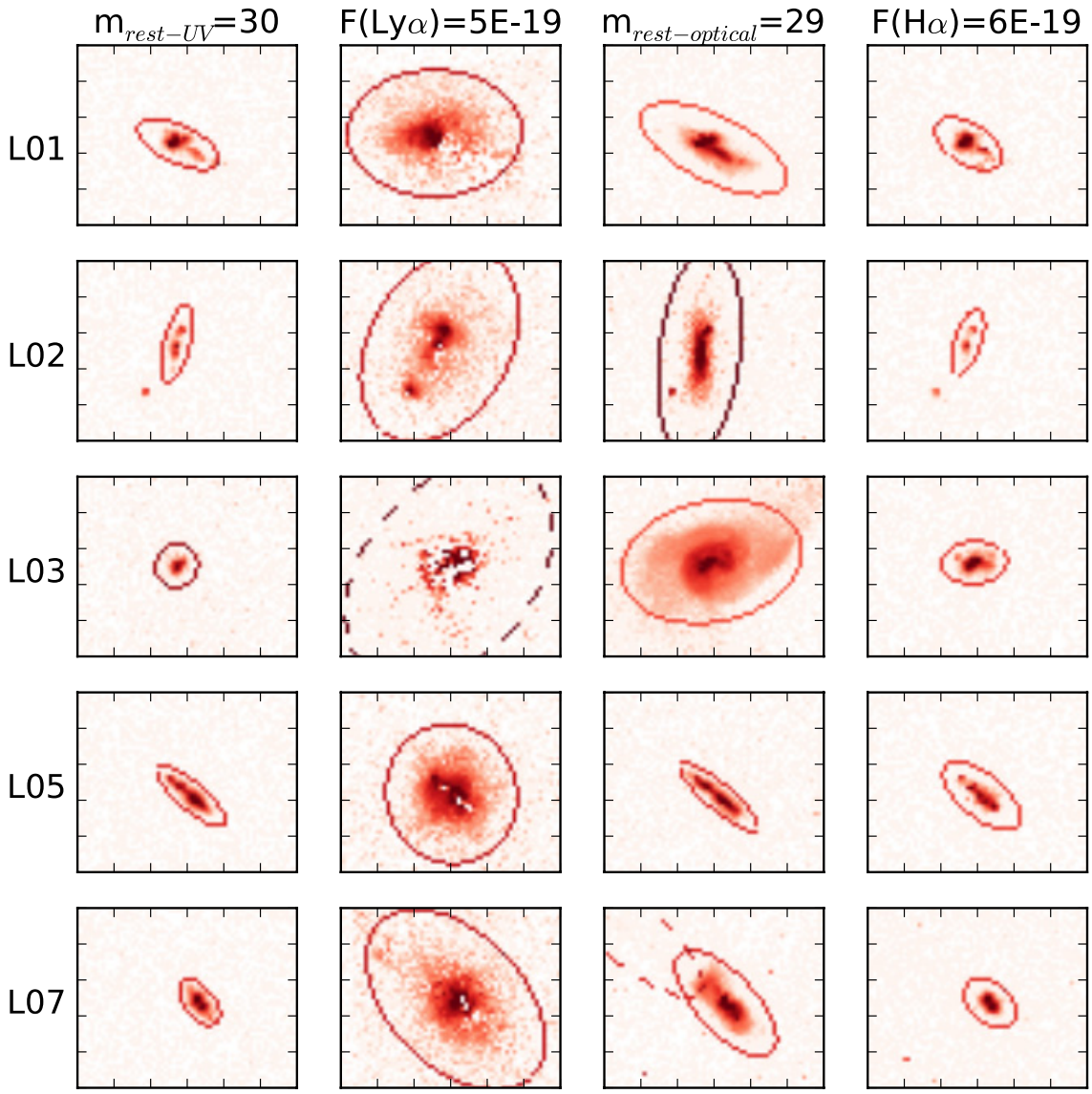

Fig. B.1. Rest-frame UV (*first column*), Lyα (*second column*), rest-frame optical (*third column*), and Hα (*fourth column panels*) images for z2L01, z2L02, z2L03, z2L05, and z2L07 in the deepest survey, probed here. Every panel is 20 × 17 kpc wide. The reddish ellipses indicate SEx apertures (dashed curves indicate flagged sources according to SEx convention), corresponding to the assumed detection parameters: DETECT THRESH = 1.65, DETECT MINAREA = 30, and DEBLEND MINCONT = 1 from Bond et al. (2009). The colour scaling is logarithmic and chosen to show a visually consistent background noise.

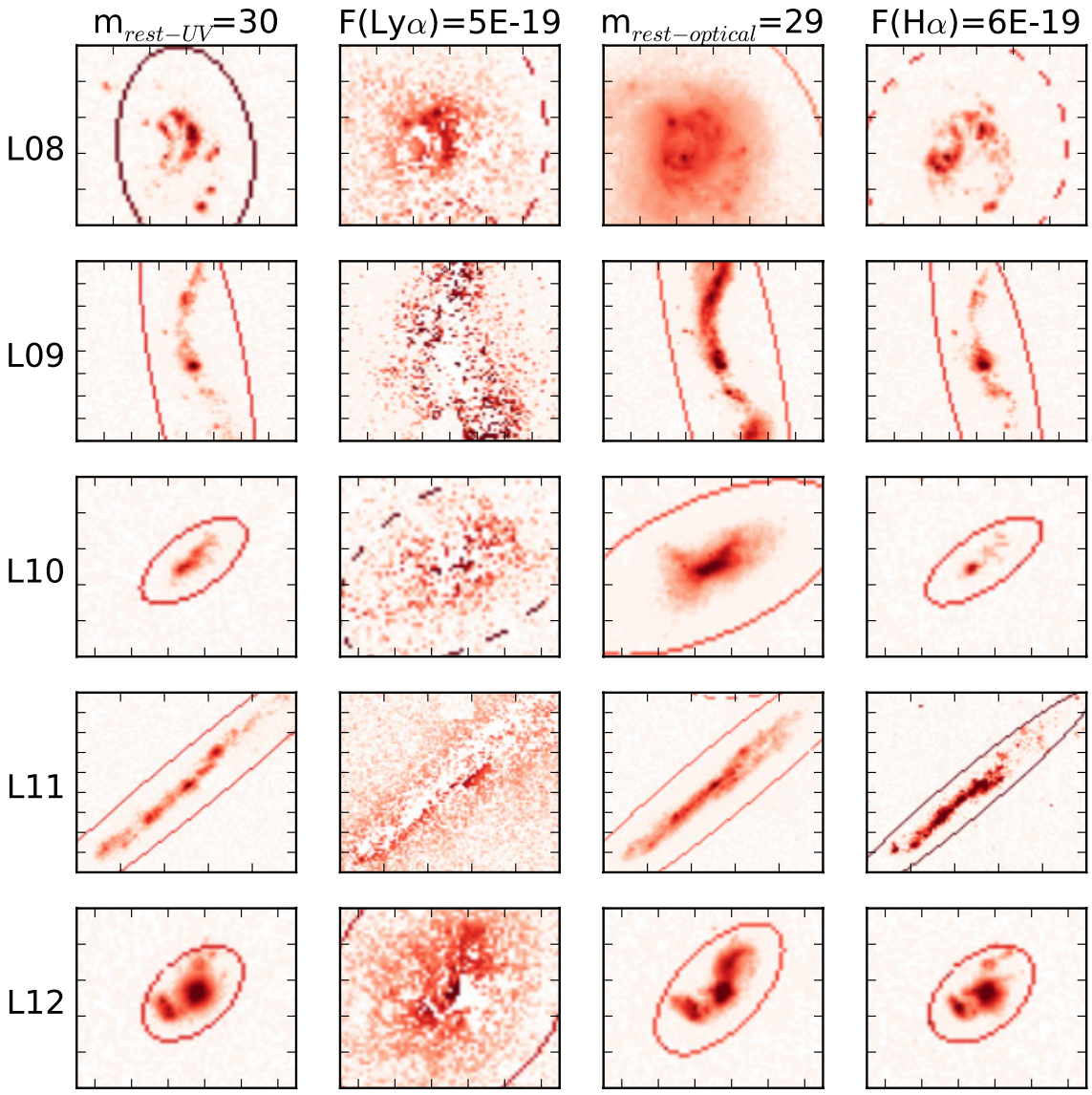

Fig. B.2. As Fig. B.1 for z2L08, z2L09, z2L10, z2L11, and z2L12. In the case of z2L09 and z2L11 the size is 27 × 27 kpc and 33 × 30 kpc respectively to fit their elongated shapes. For these galaxies SEx apertures in Lyα happen to be outside the shown region.

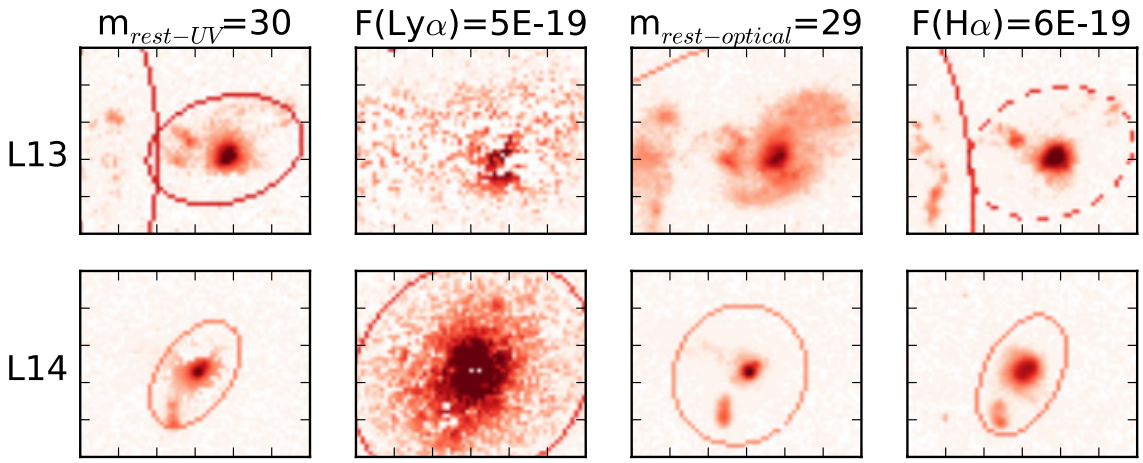

Fig. B.3. As Fig. B.1 for z2L13 and z2L14. For z2L13 SEx aperture in Lyα happens to be outside the shown region. Also, two main sources connected by undetectable ($m_{\rm rest-UV} > 30$ and $F(\rm H\alpha) < 6\text{E-}19$ erg s^{-1} cm^{-2}) surface brightness structures are seen in UV continuum and Hα. By using the chosen detection parameters, SEx found two sources as separated. As in Lyα and optical continuum the photometric measurements are done centring the aperture close to the right clump, we locate the aperture on that one for the photometry in UV and Hα as well.

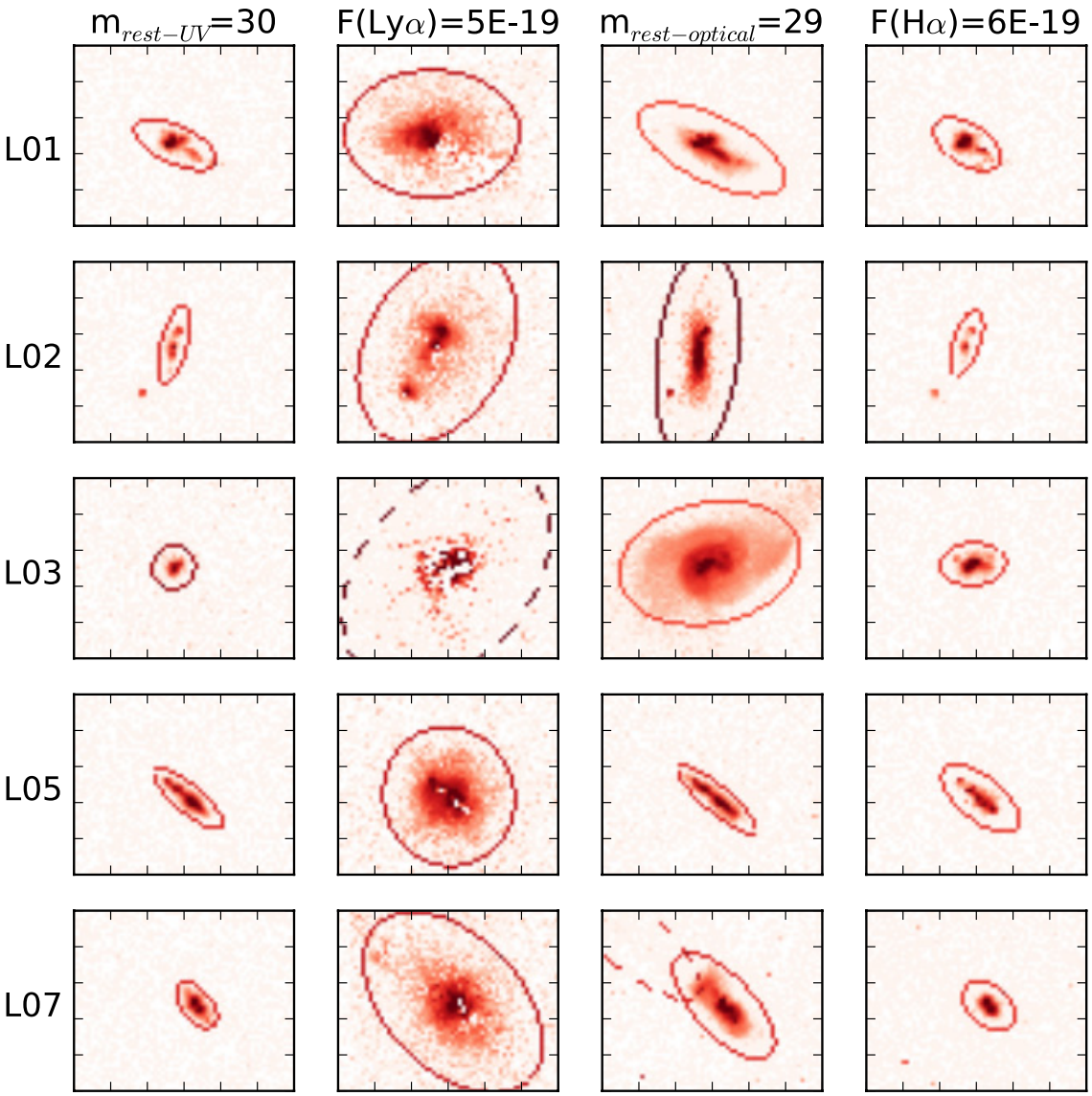

Fig. B.4. As B.1, but for a shallow simulated survey. The dashed-line apertures indicate that some detected source is blended to another (Bertin & Arnouts 1996).

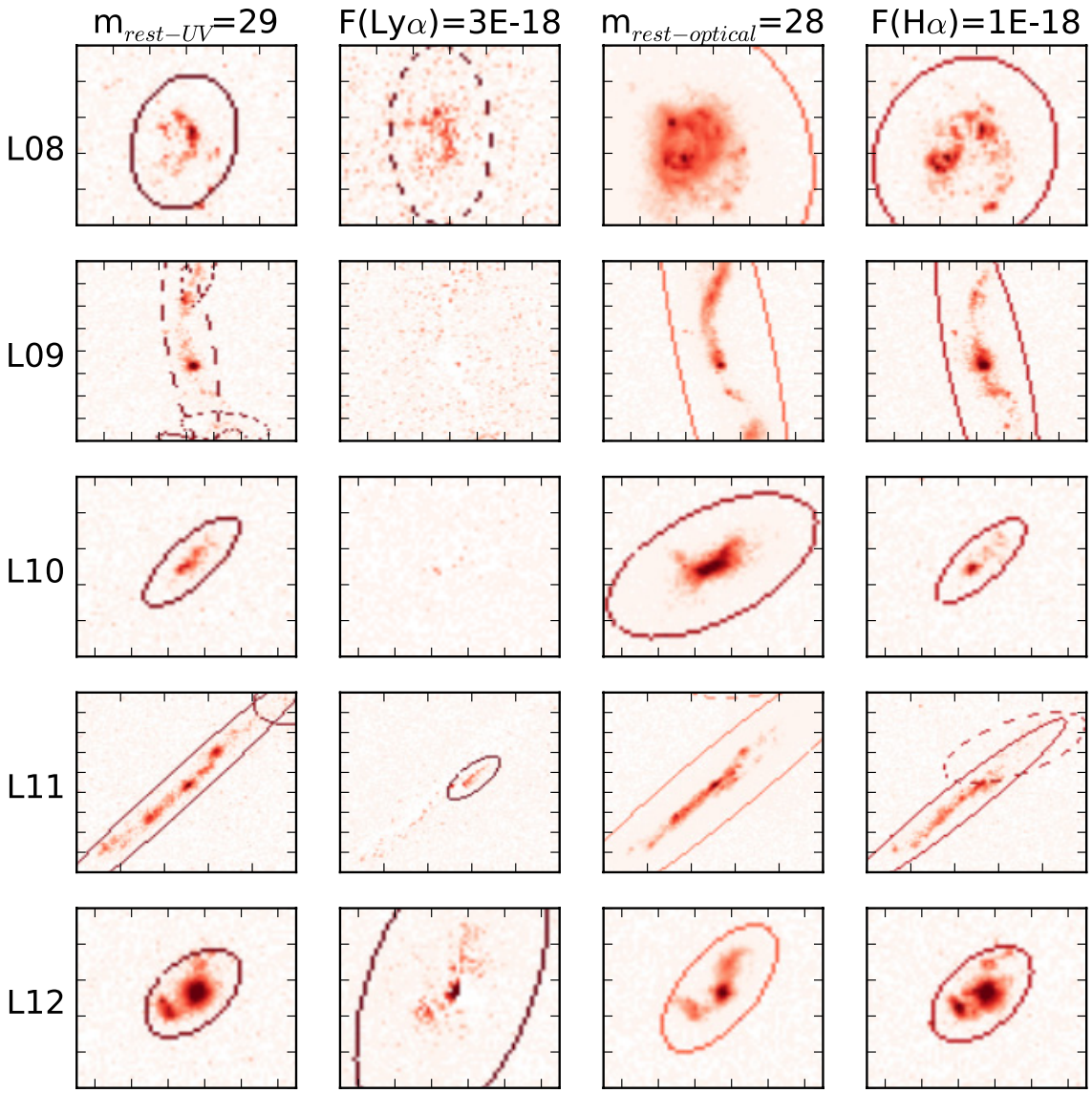

Fig. B.5. As Fig. B.2, but for a shallow simulated survey. z2L09 and z2L10 are not detected in Lyα at a 10σ detection limit of 3E-18 erg s^{-1} cm^{-2}.

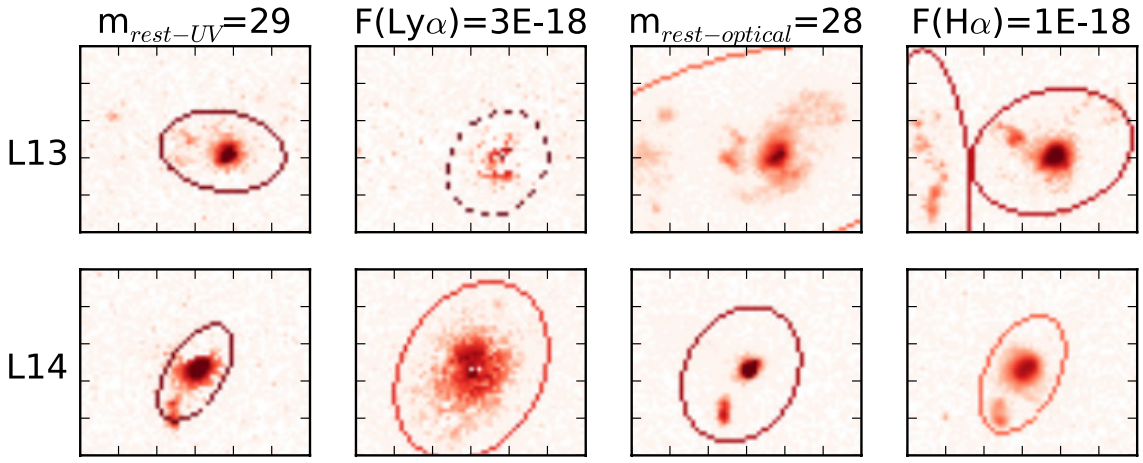

Fig. B.6. As Fig. B.3, but for a shallow simulated survey. Only the bright right clump of z2L13 is detected in UV at a 10σ detection limit of $m_{\rm rest-UV}$ = 29. Its Lyα emission is localized around the lower side of the right clump. In Hα the two overlapping sources become well separated.

Appendix C: Surface brightness profiles of original and high-*z* simulated LARS galaxies

We present here the surface brightness profiles of eleven LARS galaxies studied in this paper. The profiles of L01 were shown in Fig. 8. Every figure in this appendix shows four panels, rest-frame UV and optical continua, Lyα and Hα lines. The profiles are normalized to 2 kpc to compare continuum and line profiles.

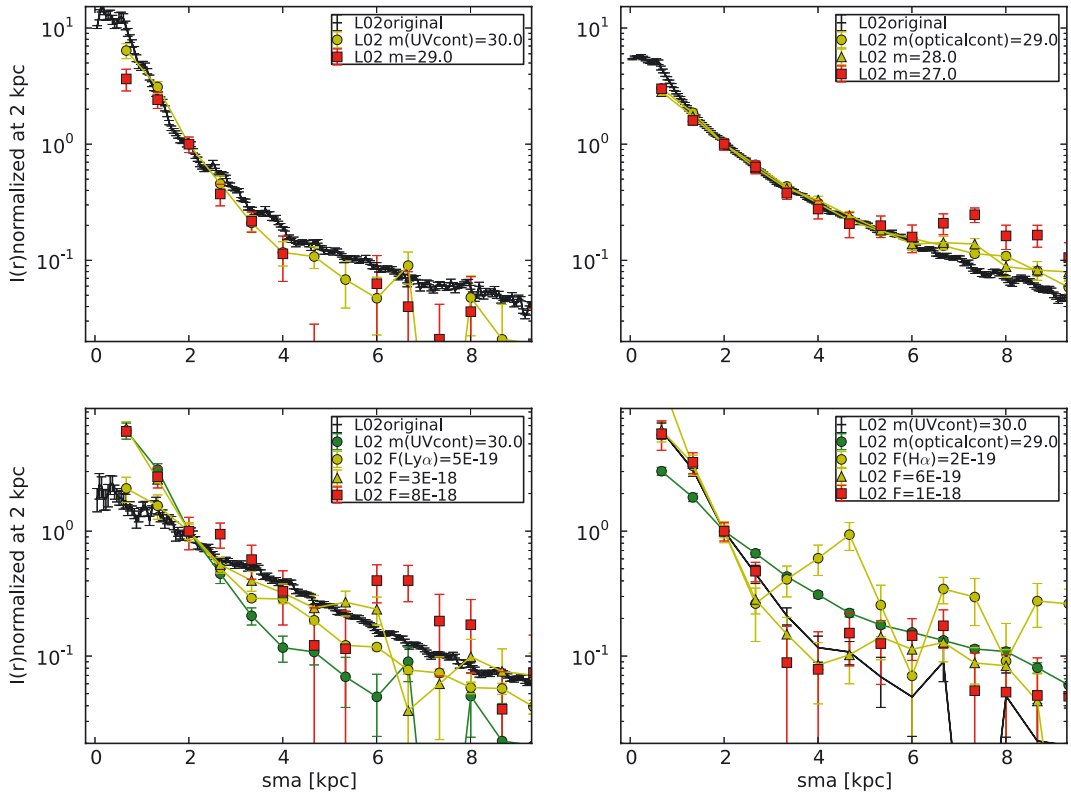

Fig. C.1. Normalized surface brightness profiles of L02. Black points with error bars correspond to the surface brightness profile of the original LARS images in the rest-frame UV, optical, and Lyα as explained in the text (Fig. 8). The red squares represent the profile affected by background noise, for a certain shallow survey.

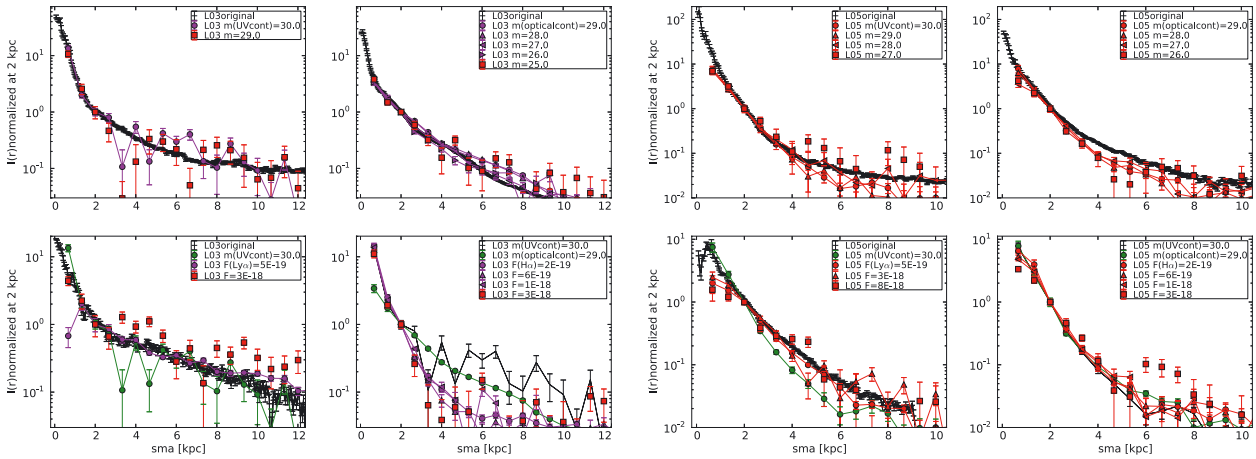

Fig. C.2. Same colour coding as in Fig. C.1, but for z2L03 and z2L05. The deepest and intermediate depth surveys are shown for z2L03(z2L05) in magenta(red) symbols with error bars, as throughout the paper.

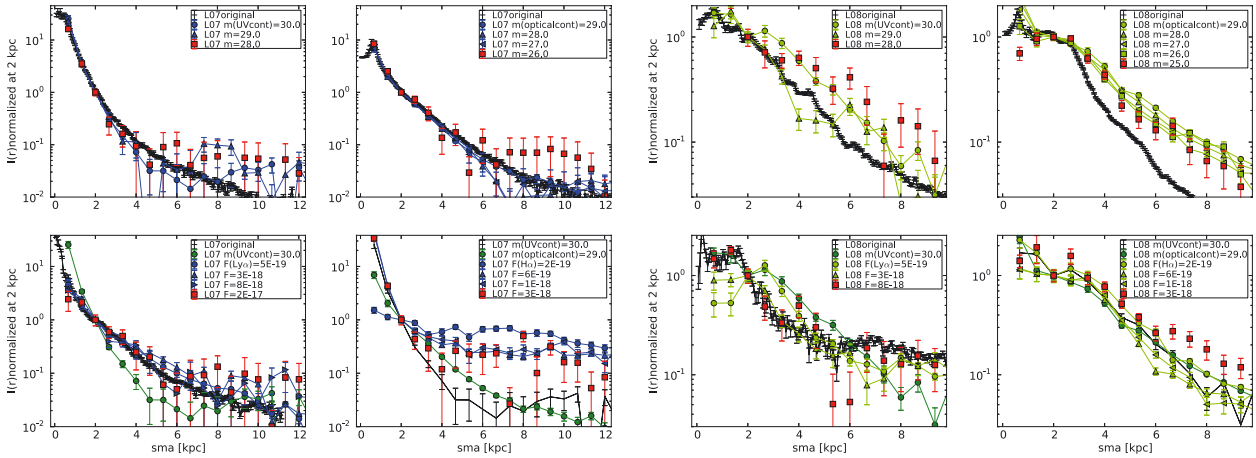

Fig. C.3. Same colour coding as in Fig. C.1, but for z2L07 and z2L08. The deepest and intermediate depth surveys are shown for z2L07(z2L08) in blue(light green) symbols with error bars.

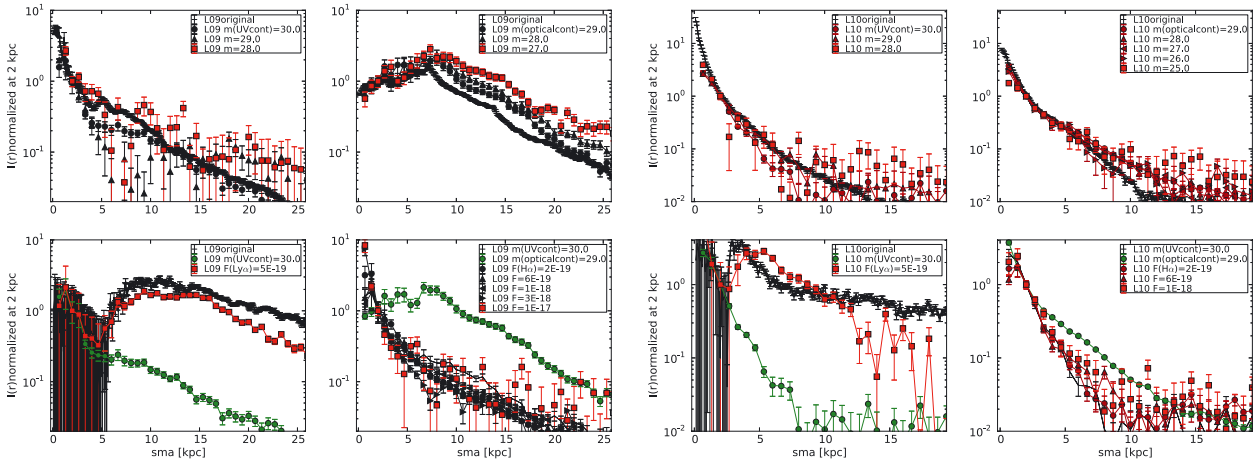

Fig. C.4. Same colour coding as in Fig. C.1, but for z2L09 and z2L10. The deepest and intermediate depth surveys are shown for z2L09(z2L10) in black(dark red) symbols with error bars.

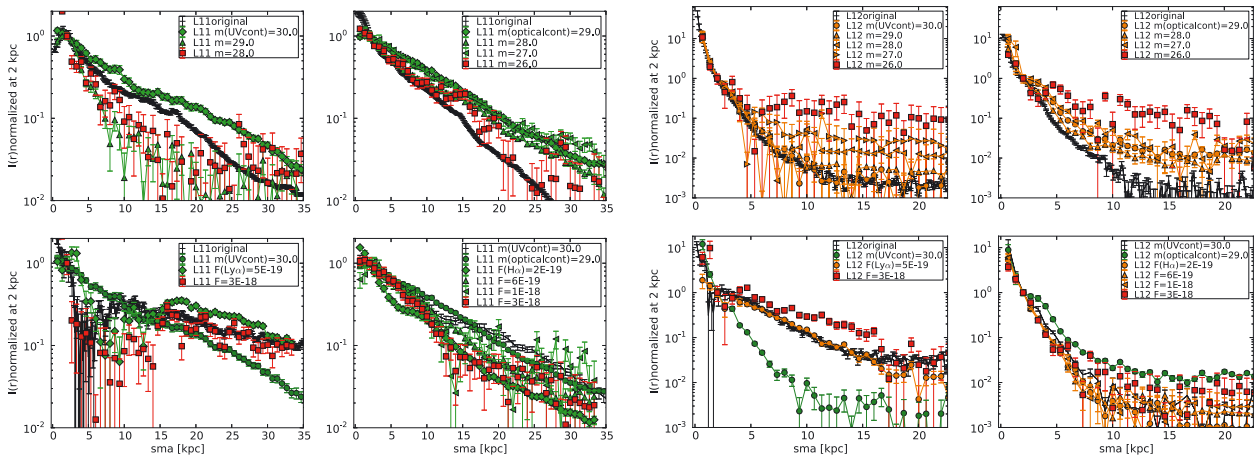

Fig. C.5. Same colour coding as in Fig. C.1, but for z2L11 and z2L12. The deepest and intermediate depth surveys are shown for z2L11(z2L12) in dark green(orange) symbols with error bars.

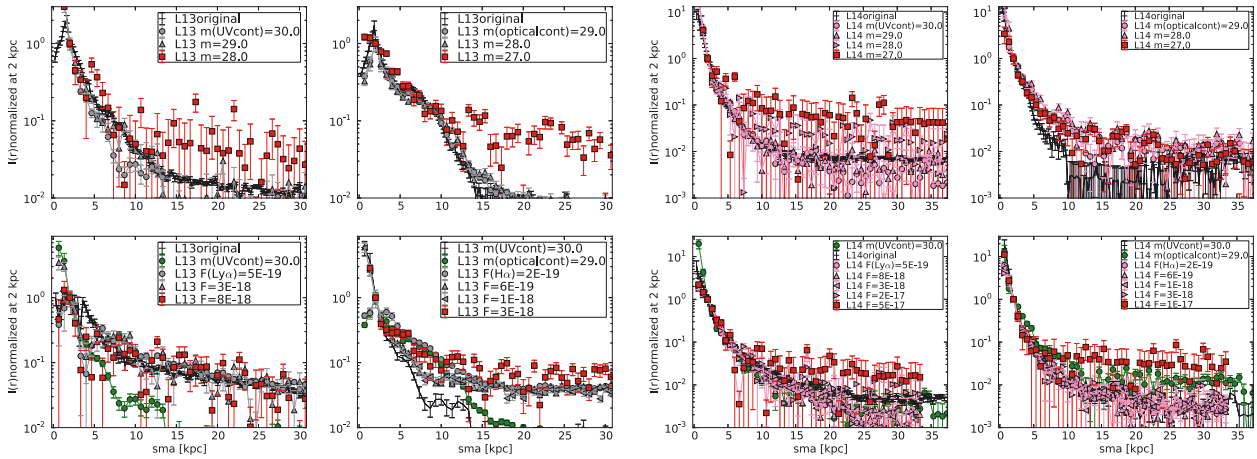

Fig. C.6. Same colour coding as in Fig. C.1, but for z2L13 and z2L14. The deepest and intermediate depth surveys are shown for z2L13(z2L14) in grey(pink) symbols with error bars.